NASA

Technical Memorandum 80285

Satellite Observations of Rapidly Varying Cosmic X-Ray Sources

Gregory Scott Maurer

MAY 1979

National Aeronautics and Space Administration

Goddard Space Flight Center
Greenbelt, Maryland 20771

THE CATHOLIC UNIVERSITY OF AMERICA

SATELLITE OBSERVATIONS OF RAPIDLY VARYING COSMIC X-RAY SOURCES*

A DISSERTATION
Submitted to the Faculty of The
School of Arts and Sciences
of The Catholic University of America
For the Degree
Doctor of Philosophy

by
Gregory Scott Maurer

Washington D.C.
1979

*Research supported by NASA Grant NSG 5066

This dissertation was approved by Carol Jo Crannell
Carol Jo Crannell

as Director and by Brian R. Dennis
Brian R. Dennis and

Carl Werntz
Carl Werntz as readers.

PREFACE

The techniques used throughout most of the OSO-8 data analysis for determination of the incident photon spectra from observed counting-rate spectra are presented in this thesis. Reevaluation of these techniques was motivated by the systematically high photon flux above the K-edge in the Crab spectra which led to unacceptable values of X^2. That reevaluation, described here, was carried out after completion of this thesis. An assumed incident spectrum was folded through the detector response function, taking into account absorption, quantum efficiency, K-escape, and detector resolution in the proper order. The resulting counting-rate spectrum was then treated as an observed incident spectrum and analyzed by the methods described in Chapter 2. At each step in the analysis the results were compared with the assumed incident spectrum at the same level of processing (e.g., after absorption, after absorption and quantum efficiency, etc.). Any discrepancies could then be identified with the processing step during which they were generated. It was found that the high point in the final spectrum was generated by the process of apodization and is a consequence of the inability of apodization to accomodate sharp features in the detector response function. Difficulties in the method are not

entirely unexpected because apodization depends on the assumption of an everywhere well-defined second derivative, which is clearly violated at the K-edge.

Because the problem described above is inherent to the method of apodization, the Crab data were reanalyzed with a different technique. Assumed incident spectra were folded through the detector response function, and the resulting counting-rate spectra were least-squares fitted to the observed counting-rate spectra. Statistical uncertainties in the spectral parameters were determined as before. Systematic uncertainties were obtained by perturbing the detector parameters by their known uncertainties and determining the effect on the spectral parameters. These uncertainties were added in RMS fashion to the statistical uncertainties.

The results of the reanalysis of the Crab observations have been submitted for publication in The Astrophysical Journal. The spectral indices presented there all agree with the results presented in this thesis. The only significant differences occur around the K-edge where apodization induced fluctuations in individual data points. The new technique does not generate these systematic fluctuations and consequently yields acceptable values of χ^2.

TABLE OF CONTENTS

LIST OF TABLES

Chapter 1

INTRODUCTION

The disciplines of astronomy and space physics have developed rapidly during the past 30 years. This development stems largely from a variety of advances in the technical capability for observations of celestial sources at photon energies outside the visible band of the electromagnetic spectrum. Radio, infrared, ultraviolet, x-ray and gamma-ray measurements have all contributed greatly to our knowledge of the structure and evolution of stars and galaxies, indeed of the universe itself. Measurements of the emission from celestial objects over a wide range of energies have clarified the interpretation of source structure and radiative processes. Observations outside the visible spectrum have led, moreover, to the discovery of astrophysical objects which are undetectable at optical wavelengths. Celestial masers, radio pulsars, and black holes are only a few examples of such objects.

Progress in x-ray and gamma-ray astronomy has been linked most directly to the ability to place observing platforms above the earth's atmosphere. For x-ray energies below 20 keV, observations from altitudes obtained by rockets or

satellites are necessary to eliminate atmospheric attenuation of the radiation. The short duration of rocket flights (usually about five minutes) has precluded their use for the observation of high-energy x rays and gamma rays because of the low flux values at these energies. The decreased atmospheric attenuation of high-energy photons, however, enables observations from balloon altitudes to be made for photon energies above 20 keV. At the present time larger and more sensitive high-energy x-ray detectors can be flown from balloons than from satellites. Balloon-borne detectors are not subject to background problems related to the high charged-particle fluxes encountered at satellite altitudes. These advantages of balloone-borne detectors are offset somewhat by the short observing times, on the order of a few hours, obtainable with balloon flights. The detection of source variability during a single flight is limited to time scales of minutes or hours. Satellite observations, on the other hand, can be performed over longer intervals, making the detection of source variability on time scales of days and weeks possible. Repeated observations, made over intervals of months and years with the same detector, provide reliable information on the long-term variability of cosmic x-ray sources.

A number of recent discoveries have demonstrated that observations with fine time resolution can contribute

greatly to our understanding of compact astrophysical objects. The temporal analysis of the radiation which many of these objects emit provides information concerning source structure and evolution which cannot be obtained from analysis of the steady emission or from measurements made with poor time resolution. For example, both secular and random changes in neutron star rotation rate can be related to changes in accretion torques, core-crust coupling mechanisms, mass transfer in binary systems, and binary orbital parameters (Lamb 1977). More observations of periodic sources, with instruments with fine time resolution, will extend the interval over which precise timing information is available.

The current status of x-ray and of gamma-ray astronomy, including both experimental and theoretical aspects of the field, has been reviewed recently by Giacconi and Gursky (1974) and by Chupp (1976).

The work presented in this thesis is focussed on satellite observations of two distinctly different astrophysical objects: the pulsar in the Crab Nebula and the x-ray binary Her X-1. The Crab pulsar, PSR 0531+21, is an isolated pulsar in the center of the Crab nebula. The pulsar and our knowledge of it are unique in several ways. It is the remnant of a supernova which was observed in 1054

A.D.; it is the fastest known pulsar, with a period of 0.033 seconds; and it is an intense source of radiation from radio to gamma-ray energies. The shape of the integrated pulse profile, obtained by binning the observed radiation modulo the pulsation period, is remarkably constant over 16 decades in photon energy. Variability in radio intensity, however, has been observed from pulse to pulse and on time scales of months (Sutton et al. 1975; Rankin et al. 1974; Lyne and Thorne 1975). No such variability has been seen in the optical emission. Forman et al. (1974) have observed rapid variations in the time-averaged low-energy x-ray flux. Recently Ryckman et al. (1977) have reported transient pulsed structure in the high-energy x-ray pulse profile. A better understanding of the temporal variability observed throughout the energy spectrum is essential to distinguish between competing theories for the emission from the pulsar.

The emission of radiation from x-ray binary systems is due to very different mechanisms than those which characterize isolated pulsars. A well studied example of an x-ray binary system is Her X-1 and HZ Her. Her X-1, a neutron star, is the secondary component in the binary system whose primary component is the late A-type star HZ Her. The x-ray emission is complex, with a break in the spectrum near 20 keV and features both above and below the break. Temporal variations are observed on several different

time scales. These aspects of the x-ray emission are discussed in detail in Chapter 6. Because of the richness of both its spectrum and its temporal variability, Her X-1 has been the object of an intensive observing program with rockets, balloons, and satellites as observing platforms. The results from this ongoing program should provide a better understanding of not only Her X-1 but the class of x-ray binaries in general.

The x-ray spectrum of Her X-1 is very complex. Shulman et al. (1975) and Catura and Acton (1975) have observed intense x-ray emission below 2 keV. The spectrum between 2 and 20 keV is relatively flat (Pravdo et al. 1977). Iron line emission near 6.7 keV has been observed by Pravdo et al. (1976). The spectrum above 20 keV decreases rapidly with increasing energy; however, Trümper et al. (1978) have observed a feature in the spectrum which they interpret as a cyclotron line at 55 keV. The richness of both the energy spectrum and the temporal variation has motivated an intensive observing program using balloons, rockets, and satellites as observing programs. As with the Crab pulsar, the variable x-ray emission can be related to the structure of the neutron star and the binary system. The relationship between timing observations and source structure is discussed in Chapter 4.

The data presented in this thesis were obtained with the High-Energy Celestial X-ray Detector on the last Orbiting Solar Observatory, OSO-8. The detector has been used, during the 39-month lifetime of the satellite, to observe most of the known celestial x-ray sources which are known to emit radiation above 20 keV. The satellite and the x-ray detector are described in Chapter 2 together with the data analysis techniques employed for periodic sources. Chapter 3 contains a summary of fundamental physical processes which are expected to be important in the production of x-rays near compact astrophysical objects. A general description of current ideas on the structure of pulsars and x-ray binaries is presented in Chapter 4. The results from two separate observations of the Crab pulsar are presented in Chapter 5. The significance of the observations is their unique potential to describe variations in the pulsed emission from day to day and from 1976 to 1977. Integrated pulse profiles and energy spectra for the pulsed, nonpulsed, and time-averaged x-ray emission are derived. The results of the Hercules X-1 observation are presented in Chapter 6. This observation is the first during which the high-energy x-ray emission was continually monitored for nearly an entire ON-state. As such it makes a valuable contribution to our knowledge of the temporal behavior of the source. The results are compared with the predictions of several theories for the x-ray emission.

Chapter 2

INSTRUMENTAL TECHNIQUES AND DATA REDUCTION

The OSO-8 satellite was launched on 1975 June 21 into a circular earth orbit with an orbital period of ∿95 minutes, an altitude of 550 km, and an inclination of 33° with respect to the equatorial plane. The satellite consists of two sections, a wheel and a sail. Six scientific instruments are housed in the wheel, which rotates at 6±1 rpm to provide a spin-stabilized platform for the two solar instruments in the sail. A schematic drawing of the spacecraft is shown in Figure 2-1. The Celestial X-ray Detector is located in the wheel. The design and construction of the detector, as well as its performance in orbit, have been described in detail by Dennis *et al.* (1976). A brief description of the instrument and the method of data collection is presented here, with emphasis on the aspects which are important in the analysis of data from periodic sources.

The Celestial X-ray Detector has as its central detection elements two identical, sodium-activated Cesium Iodide (CsI(Na)) scintillators which are adjacent to each other but optically isolated. Five more CsI(Na) scintillators surround the central elements and provide active shielding with a

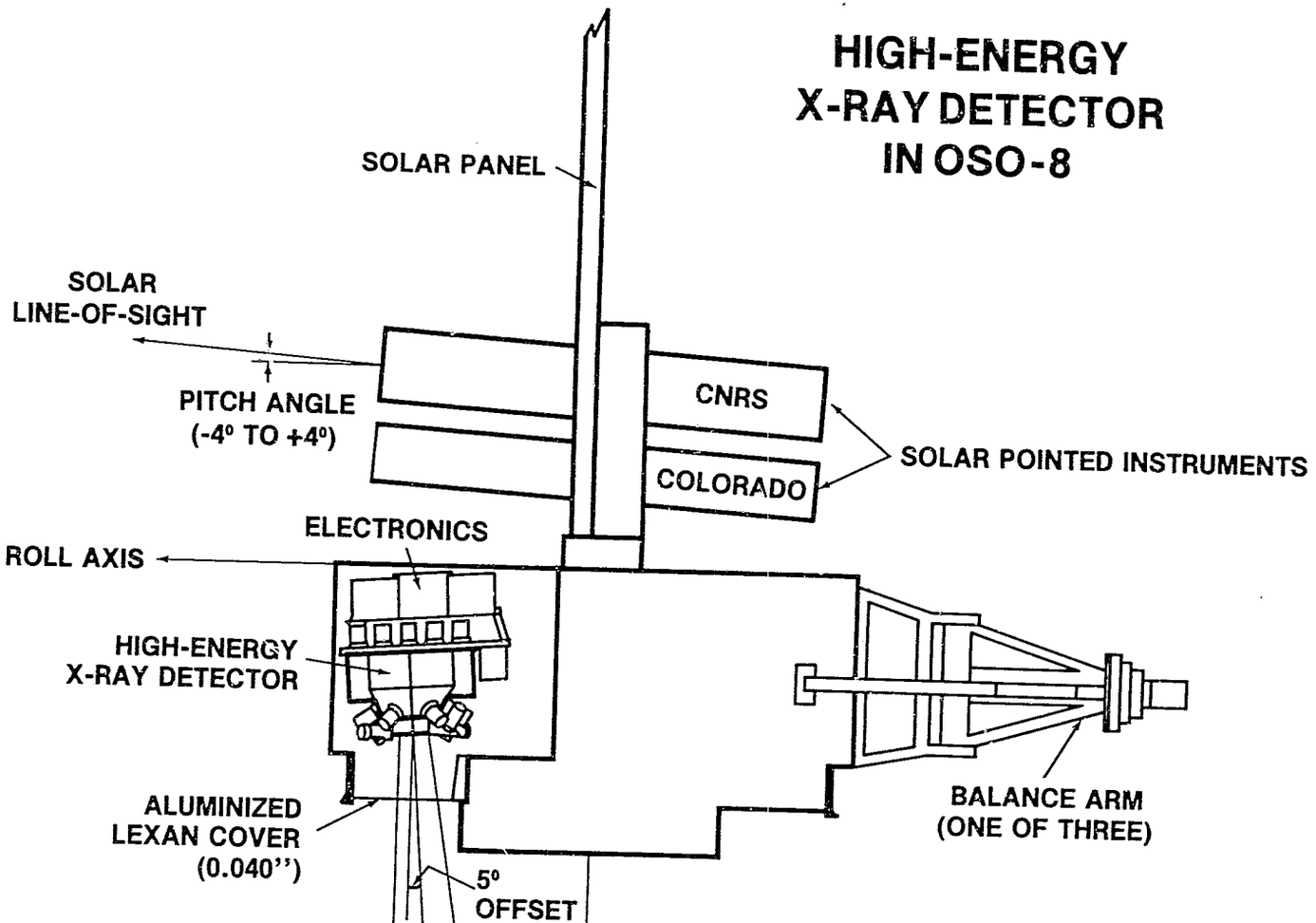

Figure 2-1. A schematic drawing of the OSO-8 spacecraft, showing the component of the satellite and the location of the High Energy X-ray Detector.

thickness of at least two inches in all directions. Two photomultiplier tubes (RCA C31016F) view each of the central elements and twelve photomultiplier tubes (RCA 70132B) view the shield crystals. The detector is shown schematically in Figure 2-2. The top shield crystal, with seventeen holes drilled through to one of the central elements, known as the open central crystal, constitutes a collimator with a 5.1° (FWHM) field of view. The total sensitive area of the open central crystal is 27.5 cm^2. The top of the collimator is covered with plastic scintillator. The other central element, the shielded central crystal, is completely surrounded by active shielding and serves as a monitor of the internal background of the instrument. Both of the central crystals are operated in anticoincidence with the CsI shield and with the plastic scintillator over the collimator. In this way events resulting from the passage of charged particles through the detector are rejected. The active shield also simplifies the data analysis by eliminating many events in which the incoming photon loses only part of its energy in the central crystals. For the purpose of in-flight calibration, a ^{241}Am source is imbedded between two solid-state detectors immediately below the central crystals. The photopeak at 59.6 keV resulting from its decay provides a continual measure of the detector's energy calibration.

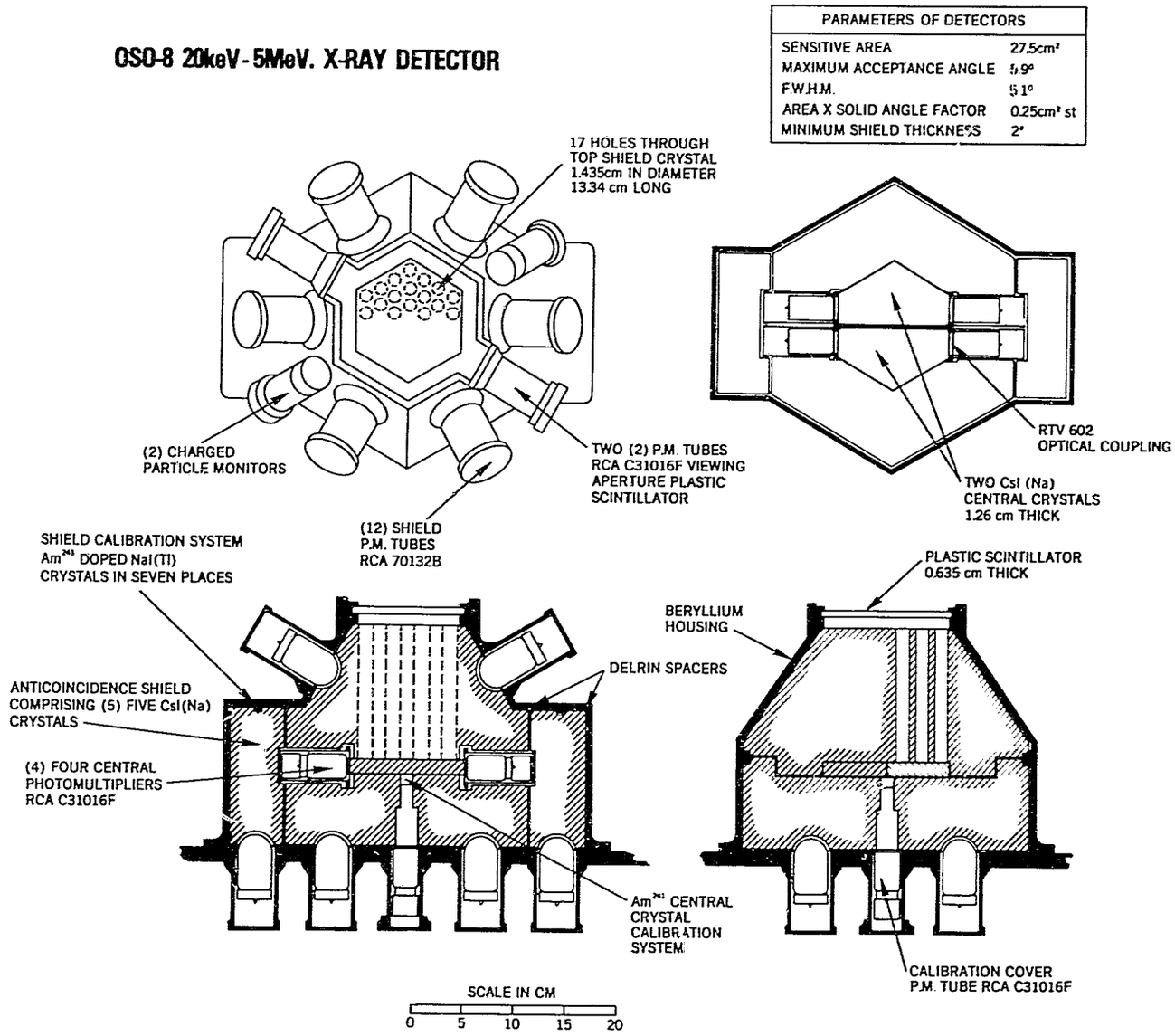

Figure 2-2. A schematic drawing of the Celestial X-ray Detector.

Background counts observed in the detector are due primarily to the decay of radioactive nuclei within the detector crystals. These nuclei are made radioactive through collisions with cosmic rays and with trapped protons in the South Atlantic Anomaly, a region of high charged particle density through which the satellite passes several times each day. The average energy of the principal peaks in the background spectrum and the isotopes responsible for their presence are shown in Table 1 (Dennis et al. 1976).

TABLE 1

Peaks in the Background Spectrum

Energy in keV	Species
34	K capture from isotopes of all elements from Sb to Ba.
67.3	^{125}I.
191	^{125}Te, ^{123}I, ^{125}Xe, ^{123}Te.
408	^{127}Xe.
603	^{121}Te, ^{126}I.

The background spectrum exhibited an increase by roughly a factor of two during the first 100 days in orbit; since then, the average shape and intensity of the background have remained nearly constant. There are, however, short-term increases in the rate as the satellite traverses the South

Atlantic Anomaly. The background rate is continually monitored by means of counting rates in the various detector components.

As mentioned above, the detector is sensitive to photons in the energy range from 15 to 3000 keV. This wide range of sensitivity is obtained through the use of 16 different gain states which can be adjusted by command from the ground. In practice, the two gain states employed for most observations cover the energy ranges from 14 to 281 and from 14 to 746 keV. The energy resolution of the open central crystal, as determined from pre-launch calibration data, in-flight calibration data, and the observed background spectrum, is well represented by the equation

$$\Delta E = 1.72\ E^{0.7} \quad \text{keV} \tag{2-1}$$

where ΔE is the full width at half maximum (FWHM) of the photopeak resulting from an incident beam of monoenergetic photons with energy E in keV. This corresponds to a FWHM of 30 keV at 60 keV. The value of the coefficient in equation (2-1), 1.72, is somewhat larger than that obtained in the preliminary analysis and reported by Dennis et al. (1976); the larger value found in subsequent analysis provides a better fit to the observed in-orbit background and calibrate spectra for the observations presented here.

An ultrastable clock was used to time each detected photon to the accuracy required for observations of the 33-ms periodicity of the Crab pulsar over many days. This clock, on board the spacecraft, is a (5.126±0.000001)-MHz, temperature-controlled crystal oscillator which is stable to better than one part in 10^9 per day. Each day the real-time telemetry bit stream driven by the clock was precisely time tagged to better than 0.1 ms with universal time (UTC) as maintained by the LORAN-C network. Events in the scintillation spectrometer were tagged with a pulse from a 3.2 kHz clock derived from the spacecraft clock. The time resolution of the instrument is thus 0.3125 ms, sufficient for the most rapidly varying periodic x-ray sources known. The daily UTC time tag enables direct comparisons of x-ray events observed on the satellite to be made with the radio and optical events observed with ground-based equipment. Such ground-based observations are regularly made with 0.1 ms time resolution (Manchester and Taylor 1977).

The method of data acquisition is determined by the spacecraft telemetry format, which consists of major frames each lasting 20.48 s. A major frame contains 128 minor frames, and each minor frame contains 128 8-bit words. Eighteen of these words are available for telemetering data from the Celestial X-ray Detector. Eight pairs of adjacent words are located every 20 ms in the minor frame. These

pairs are used to read out the pulse amplitude (8 bits) and time of occurence (6 bits) of the first event detected in the previous 20 ms. One bit is used to indicate which of the central crystals produced the event and one bit is used to indicate if a pulse from the ^{241}Am calibration system occurred in coincidence with the central crystal event. If more than one event occurred during the 20 ms interval, only data from the first is read out. Subsequent events are lost but the livetime encoded in the seventeenth word records the lack of sensitivity during that time. Pulse amplitude and time of detection for up to 50 events s^{-1} can thus be telemetered. The eighteenth word used in each minor frame contains various counting rate data from the different detector elements and housekeeping data consisting of voltages, temperatures, etc.

The detector is mounted in the wheel section of the satellite so that the angle between the antispin axis and the detector collimator axis is 5°. As the wheel rotates at a rate of 6±1 revolutions per minute, the detector scans a small circle of 5° radius on the celestial sphere. For a source located 5° away from the antispin axis, the wheel rotation provides measurements of the source and the background once every 10 seconds. As is described in the next section, this aspect of the satellite geometry figures importantly in the analysis of the data.

The length of time during which any one source can be observed is also determined to a large extent by the spacecraft geometry. Constraints are placed on the satellite orientation by the requirement that the two solar instruments mounted normal to the spin axis be pointed continuously at the sun. This allows the possibility for sources lying in the ecliptic plane to be observed by the Celestial X-ray Detector for a maximum duration of 18 days twice per year when the direction to the source is normal to within ±3° to the direction of the sun. A source located at the ecliptic pole can be observed indefinitely. In practice, because of the limited supply of gas for orientation maneuvers, sources of interest were observed only once each year.

2.1 CALCULATION OF OBSERVED SOURCE FLUX

The response function of the Celestial X-ray Detector to a celestial source within 10° of the antispin axis is a periodic function of time. This is a consequence of the rotation of the wheel section of the satellite and the nonzero angle between the spin axis and the detector collimator. Reduction of data from pulsed sources is thus a two-stage process: first, the modulation of the incident flux by the detector response function must be deconvolved; then the resulting variable flux from the source must be analyzed for periodic structure.

For a collimated detector with cylindrical symmetry, the detector response function may be expressed simply as a function of the angle between the collimator axis and the source. This angular separation will be denoted hereinafter as the distance from the source (DFS). The detector response as a function of DFS is shown in Figure 2-3 for an infinitely distant point source. For a perfectly absorbing shield, the response is triangular except for slight broadening at the base. For any real material, however, the triangle is extended because of shield penetration by high-energy photons. For photons with energies less than a few hundred keV this broadening is negligible. A calculation of the detector response as a function of energy and DFS, based on the work of Mather (1957), is described in Appendix A.

The determination of source flux from the raw data can be considered to be the calculation of the average source flux from many independent measurements of the instantaneous source flux. To make this notion precise, let

k, k' = summation indices each value of which corresponds to a particular time interval. The unprimed indices correspond to quantities measured when the source is in the field of view. The primed indices correspond to quantities measured when the source is not in

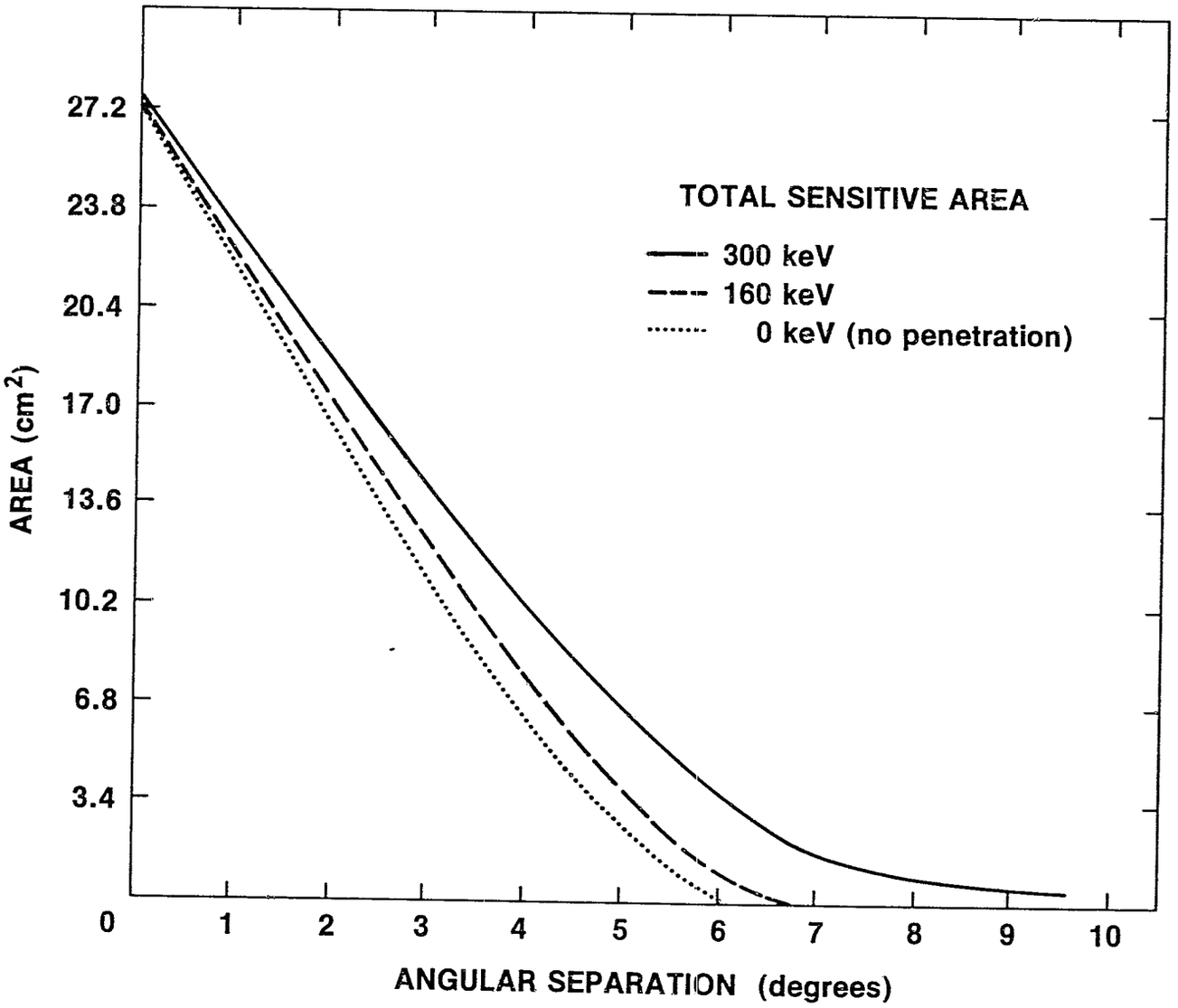

Figure 2-3. The effective area of the Celestial X-ray Detector as a function of the angular distance from the source and the incident photon energy.

the field of view.

n_k = the total number of counts in the kth time interval;

B_k = the number of background counts expected in the kth time interval;

t_k = the total livetime in the kth time interval;

r = the background rate in counts per second;

A = the total sensitive area to photons incident parallel to the collimator axis;

A_k = the sensitive area normal to the vector from the satellite to the source during the kth time interval;

f_k = the source flux during the kth interval;

f = the source flux in counts s^{-1} cm^{-2};

Θ = the angular distance from source(DFS); and

E = the energy loss in the open central crystal.

The expression for the weighted mean source flux is

$$(2\text{-}2) \qquad f(E) = \frac{\sum_k (n_k - B_k)\, w_k / t_k A_k}{\sum_k w_k} \equiv \frac{\sum_k f_k\, w_k}{\sum_k w_k}$$

where $w_k = 1/\sigma_k$ and σ_k is the uncertainty in f_k. For sources which are weak compared to the background (a situation which is the case for most sources observed with the scintillation spectrometer) the best estimate of the expected number of counts is derived from the mean background rate. The background rate is defined as

$$(2\text{-}3) \qquad r = \sum_{k'} n_{k'} \Big/ \sum_{k'} t_{k'} \quad ;$$

B_k is then equal to the product of r and the livetime t_k.

The formal uncertainty in the source flux is calculated under the assumption that n_k and $\{n_{k'}\}$, the set of all counts contributing to the background, are Poisson-distributed independent random variables. The quantities A_k and t_k are further assumed to be known exactly. With these assumptions the expression for the square of the uncertainty in f_k is

$$(2\text{-}4) \qquad \sigma_k^2 = \left[\frac{\partial f_k}{\partial n_k}\right]^2 \sigma^2_{n_k} + \sum_{k'} \left[\frac{\partial f_k}{\partial n_{k'}}\right]^2 \sigma^2_{n_{k'}}$$

where

$$\frac{\partial f_k}{\partial n_k} = \frac{1}{t_k A_k} \quad ; \qquad \frac{\partial f_{k'}}{\partial n_{k'}} = \frac{1}{A_k \sum_{k'} t_{k'}} \quad ;$$

$$\sigma_{n_k}^2 = r t_k ; \text{ and } \quad \sigma_{n_{k'}}^2 = r t_{k'} .$$

With these substitutions, equation (2-4) becomes

$$\sigma_k^2 = \frac{r}{t_k A_k^2} \left[1 + \frac{t_k}{\sum_{k'} t_{k'}} \right] \tag{2-5}$$

Since $t_k << \sum t_{k'}$, the term in brackets in the above equation is approximately unity, so that

$$\sigma_k^2 = \frac{r}{t_k A_k^2} \quad . \tag{2-6}$$

After substituting (2-6) into (2-2), the result is

$$f(E) = \sum_k n_k A_k - r \sum_k t_k A_k \Big/ \sum_k t_k A_k^2 \quad . \tag{2-7}$$

The expression for the squared uncertainty in f(E) is

$$\sigma_f^2 = \sum_k \left[\frac{\partial f}{\partial n_k} \right]^2 \sigma_{n_k}^2 + \sum_{k'} \left[\frac{\partial f}{\partial n_{k'}} \right]^2 \sigma_{n_{k'}}^2 \tag{2-8}$$

Expressing the partial derivatives and uncertainties in terms of measurable quantities, the result is

$$\sigma_f^2 = r\left[\frac{1}{\sum t_k A_k} + \frac{\left[\sum t_k A_k\right]^2}{\sum t_{k'} \left[\sum t_k A_k^2\right]^2}\right]. \qquad (2\text{-}9)$$

2.2 CALCULATION OF INCIDENT PHOTON SPECTRUM

The source counting rate spectrum calculated using the equations derived in the previous section differs from the incident photon spectrum. The measured energy-loss spectrum must be corrected for attenuation in inert material overlying the active volume of the detector, detector quantum efficiency, the escape of fluorescent photons, and the finite energy resolution of the detector. The following procedure for taking these effects into account is based on the work of Dolan (1972). The incident photon spectrum and the observed counting rate spectrum are represented by vectors, and the photon interactions as matrices which attenuate or redistribute the components of the incident spectrum vector. The dimension of the vector is equal to the number of pulse amplitude bins used in the analysis. The equation for the observed source spectrum is

$$V_o = MV \qquad (2\text{-}10)$$

where V_o is the observed spectrum, V is the incident photon spectrum, and M is the matrix operator representing the detector properties. M may be written as

$$M = M_R M_E M_Q M_W M_A \tag{2-11}$$

M_A represents the attenuation of the incident flux by any residual atmosphere. M_W represents the attenuation by window material covering the central detecting element. The quantum efficiency, fluorescent escape, and detector energy resolution are represented by the matrices M_Q, M_E, and M_R. M_A and M_W thus take into account interactions of incident photons before they reach the detecting elements, while the remaining matrices describe the fundamental interactions within the detecting element. Each of these matrices is discussed in the following paragraphs.

Because there is no residual aatmosphere above the satellite, M_A is the identity matrix. For the sake of completeness, however, expressions for M_A in the presence of overlying atmosphere are given. If E(i) is the energy at the center of the ith pulse height channel and $\tau_A(i)$ is the optical depth of the atmosphere at energy E(i), then

$$M_A(i,j) = \delta_{ij} \exp\{-\tau_A(i)\} \tag{2-12}$$

where δ_{ij} is the Kronecker delta and

(2-13) $$\tau_A(i) = (\mu/\rho)_{A,i}(\rho x)$$

with (ρx) being the residual atmosphere above the detector in g cm^{-2} and $(\mu/\rho)_{A,i}$, the mass absorption coefficient of air in cm^2 g^{-1} at energy E(i).

The attenuation of the incident flux in the window material is treated in the same manner. If $\tau_W(i)$ is the optical depth of the window material at energy E(i), then

(2-14) $$M_W(i,j) = \delta_{ij}\exp\{-\tau_W(i)\}$$

M_Q represents the quantum efficiency of the detector. The expression for M_Q is

(2-15) $$M_Q(i,j) = \delta_{ij}\{1 - \exp(-\tau_Q(i))\}$$

where $\tau_Q(i)$ is the optical depth of the detecting medium at energy E(i). A plot of the detection probability, which includes the effects of M_W and M_Q is shown in Figure 2-4.

The redistribution of photon energies through fluorescent escape is represented by M_E. Fluorescent photon escape occurs after an incident photon with energy E ejects a K-shell electron from an atom in the detecting medium. When

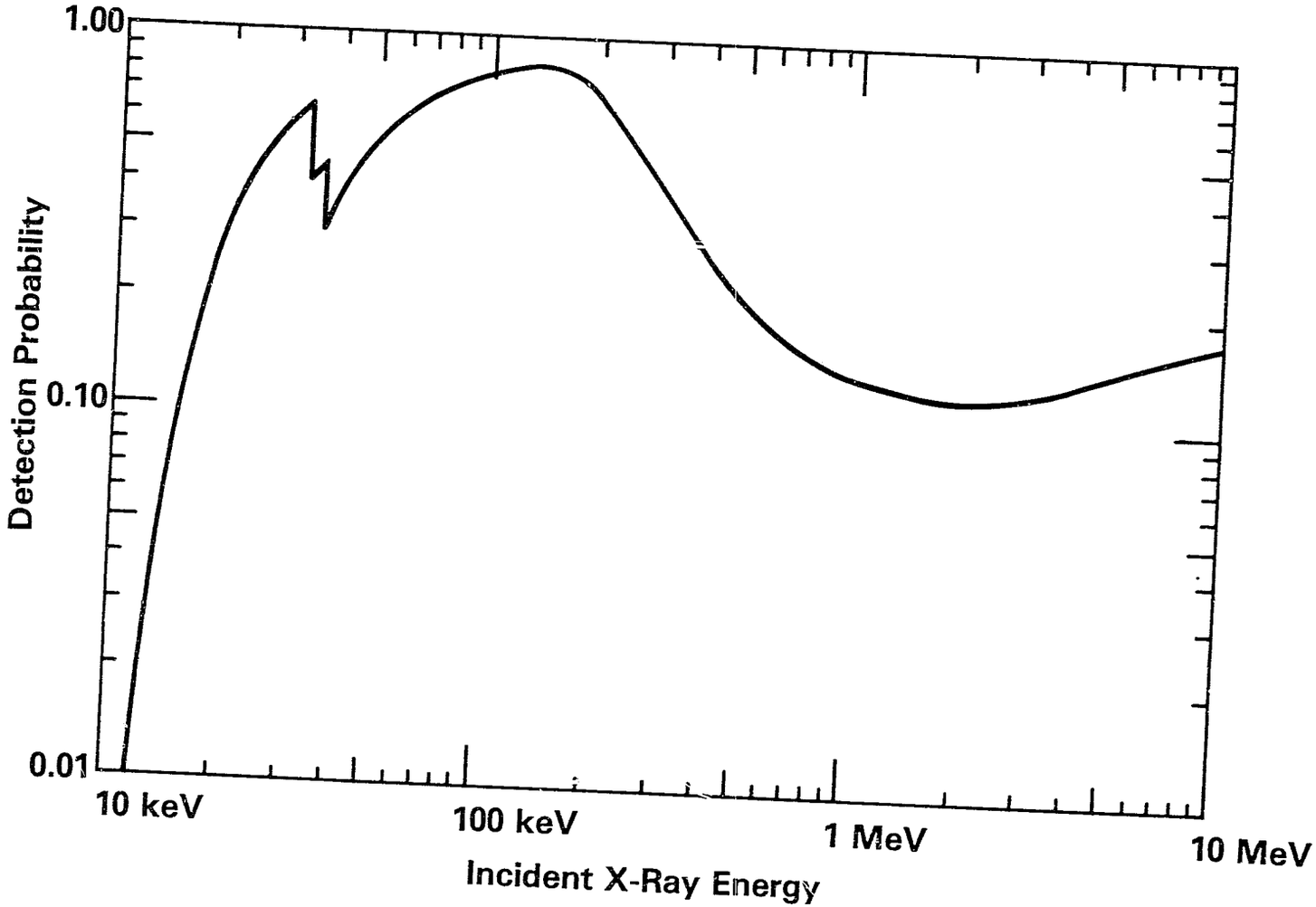

Figure 2-4. The detection probability, which includes the effects of quantum efficiency and absorption in the windows and the dead layer.

the K-shell vacancy is subsequently filled by an electron, usually from the L shell, the emitted photon has a high probability of escaping from the detector, mainly back through the front surface. The high probability arises because the fluorescent x-ray lacks sufficient energy to eject a K-shell electron. The result is that a photon with incident energy E(j) deposits only energy E(i)=E(j)-E(k) in the crystal, where E(k) is the K line energy. To quantify this process, let "a" be the energy, in channels, of the K_α photon; let "b" be the energy, in channels, of the K_β photon; let α be the fraction of K_α photons emitted; and let β be the fraction of K_β photons emitted. Note that K_α photons result from transitions to the K shell from the L shell and K_β photons result from transitions to the K shell from higher shells (M, N, etc.). If η_j is the fraction of detected photons with energy E(j) (E(j)>E(k)) which are detected with energy E(j)-E(k), then

$$M_E(i,j) = \delta_{ij} \qquad (j<k)$$

(2-16)

$$M_E(i,j) = \delta_{ij}(1-\eta_j) + \delta_{i+a,j}\alpha\eta_j + \delta_{i+b,j}\beta\eta_j \qquad (j>k)$$

The values of η used in this analysis were taken from the work of Riegler (1969). See also the work of Stein and Lewin (1967). A notational difficulty in Dolan (1972) has been corrected in equation (2-16).

The detector resolution, as discussed in section 2.1, is well represented by equation 2-1. The standard deviation of the gaussian line shape is related to its full width at half maximum (FWHM) by

$$\sigma = 0.4247\,\mathrm{FWHM} \tag{2-17}$$

The elements of the resolution matrix M_R are the corresponding values of the gaussian:

$$M_R(i,j) = \frac{W(j)}{\sqrt{2\pi}\,\sigma_j} \exp \frac{E(i)-E(j)}{2\,\sigma_j^2} \tag{2-18}$$

where W is the channel width in energy units and σ_j is derived from equations (2-1) and (2-17).

The incident photon spectrum is obtained by solving equation (2-10) for V:

$$V = M^{-1}V_o = M_A^{-1}M_W^{-1}M_Q^{-1}M_E^{-1}M_R^{-1}V$$

Since M_A, M_W, and M_Q are diagonal matrices, their inversion is trivial:

$$M_A^{-1}(i,j) = \delta_{ij}\exp(\tau_A(i)) \tag{2-19}$$

$$M_W^{-1}(i,j) = \delta_{ij}\exp(\tau_W(i)) \tag{2-20}$$

(2-21) $$M_Q^{-1}(i,j) = \delta_{ij}/(1 - \exp(-\tau_Q(i)))$$

M_E is not diagonal but can be inverted using any standard numerical matrix inversion subroutine.

The resolution matrix M_R is difficult to invert numerically because adjacent rows are nearly equal, making the determinant nearly zero. The matrix is, for all practical purposes, singular. To avoid the problems encountered in inverting M_R, the resolution is taken into account using the method of apodization (Lloyd 1969; Dolan 1972). Apodization enables construction of a spectrum V_a from an observed spectrum V_o by using the known properties of the finite detector resolution. V_a is the distribution of counts which would be observed if the energy resolution were perfect. As shown by Lloyd,

(2-22) $$V_a(i) = V_o(i) - S(i)\left[0.5\{V_o(i+\ell) + V_o(i-\ell)\} - V_o(i)\right]$$

where ℓ is the apodization length in channels and $S(i) = (\sigma_i/\ell)^2$ for a gaussian line shape. The final expression for the incident photon spectrum is then

(2-23) $$V = M_A^{-1} M_W^{-1} M_Q^{-1} M_E^{-1} V_a$$

The method of apodization, as discussed above, eliminates problems associated with the inversion of singular matrices. It provides a reasonable method for determining incident photon spectra from observed counting rate spectra. Some care must be used, however, when interpreting the results of apodization. Two points in particular must be remembered. First, apodization has a tendency to enhance statistical fluctuations, as may be seen from equation (2-22). Secondly, individual spectral points are no longer statistically independent, so that care must be used in determining the goodness of fit when an assumed spectral shape is fitted to the apodized data.

2.3 SPECTRUM FITTING

Once the incident photon spectrum has been obtained, it is fitted to model functions using a variation of the CURFIT routine of Bevington (1969). These models were restricted to either power-law spectra or thermal spectra with and without additional gaussian lines. The physical basis for these particular forms is discussed in subsequent chapters.

The uncertainties in the derived spectral parameters are determined from the confidence contours in chi-squared space as described by Lampton et al. (1975). This method of estimating the confidence in the spectral fit is based on the distribution of $\chi^2 - \chi^2_{min}$, where χ^2_{min} is the minimum

value of chi-squared obtained during the fitting procedure. The best fit values of the parameters are those for which χ^2_{min} obtains. The parameters are then perturbed about their best fit values and the value of chi-squared calcr ated. For a spectral fit involving p spectral parameters, $\chi^2 - \chi^2_{min}$ is distributed as chi-squared with p degrees of freedom. The determination of confidence contours is most clearly demcnstrated by considering the special case of two parameters. The confidence intervals are obtained by projecting constant values of $\chi^2 - \chi^2_{min}$ onto the plane defined by the parameter axes. The confidence contour so projected defines a conic section, usually an ellipse. The parameters are statistically independent if the major and minor axes of the contour are parallel to the parameter axes. If this is the case, then the uncertainty quoted for one parameter is independent of the value of the other parameter. If the axes of the conic section are not parallel to the parameter axes, then the quoted uncertainties will be, in general, too small. More detailed discussions of confidence interval estimation may be found in Meyer (1973) and Lampton et al. (1976).

2.4 PULSE TIMING

Complete analysis of the radiation emitted from periodic x-ray sources includes the determination of spectral variation as a function of pulse phase. The phase

distribution, also known as the integrated pulse profile, is accumulated by binning events according to their predicted phase at the barycenter. The analysis described in section 2.2 is then performed for each phase interval. Each of the relevant quantities is then indexed by phase as well as time interval and energy. Because the background rate, r(j), is expected to be independent of phase, j, r(j) was replaced in the present analysis by the mean background rate, $r = r(j)/N$, where N is the number of phase intervals into which the period was divided. This change leads to a reduction by a factor of N in the second term of the expression for the squared uncertainty in f(E) (equation 2-9).

To facilitate comparison with other pulse timing techniques, a detailed description of the timing procedure used in this work is presented in the following subsections.

2.4.1 Astronomical Time Scales

The three different time scales used in the OSO-8 data analysis are coordinated universal time (UTC), atomic time (AT), and ephemeris time (ET). The relationship between these times is best understood by considering first the definition of universal time. Universal time is determined from observations of the stars and is corrected for motion of the earth's rotation axis and for variations in the

earth's rotation rate. The natural unit of time in this system is a fraction of the rotation period of the earth relative to the fixed stars. The different universal time scales are as follows (U. S. Naval Observatory Time Service Repcrt, Series 11, 225):

1. UT0: obtained by observing transit times of stars;

2. UT1: UT0 corrected for polar motion; and

3. UT2: UT1 corrected for seasonal variations in the earth's rotation rate.

4. UTC: an atomic time scale defined to coincide with UT1(see below).

The atomic time scale is defined in terms of the frequency of an electronic transition in a particular atom. The particular atomic time scale used in this work is the A.1 time scale maintained by the United States Naval Observatory. A.1 is defined as follows (U.S. Naval Observatory Time Service Notice 6, 1959):

"1. A clock which keeps time A.1 advances one second in the time required for 9,192,631,770 oscillations of cesium at zero field.

2. at 0h 0m 0s UT2 on 1 January 1958 the value of A.1 was 0h 0m 0s."

Ephemeris time is determined from the solution to the equations of motion for the solar system. In some sense the unit of time is a parameter which is used to fit the positions of the sun and planets. The difference between ET and A.1 is

$$ET - A.1 = 32.15 \text{ s}$$

On the basis of observational data presently available, this difference between ET and A.1 is constant, i.e. ET and A.1 clocks run at the same rate.

The coordinated universal time (UTC) scale is defined to have the same natural unit length as A.1; however, it is also constrained so that

$$|UTC - UT1| < 0.8 \text{ s}$$

Since the A.1 and UT1 clocks have different rates, the above restriction requires the periodic insertion of leap seconds into the UTC time scale. UT1, rather than UT2, is used in the definition because certain applications such as precise navigation and satellite tracking, require a time scale referenced to the earth's rotation(National Bureau of Standards Special Publication 432, 1976) The difference

between A.1 and UTC for the duration of the OSO-8 mission is shown in Table 2. The tabulated values of the time difference apply to UTC and A.1 clocks which are at rest in an inertial frame. Relativistic corrections are necessary because of the earth's motion in the sun's gravitational field. Relativistic effects vary in strength according to the position of the earth in its orbit and lead to corrections in the atomic time of the order of milliseconds. The exact form of the corrections is presented in the next section.

TABLE 2

Difference between A.1 and UTC

from	to	A.1-UTC (s)
1975 Jan 1 0h UT	1975 Dec 31 23h59m60s UT	14.0343817
1976 Jan 1 0h UT	1976 Dec 31 23h59m60s UT	15.0343817
1977 Jan 1 0h UT	1977 Dec 31 23h59m60s UT	16.0343817
1978 Jan 1 0h UT	1978 Dec 31 23h59m60s UT	17.0343817

2.4.2 Barycentric Arrival Time

The correct determination of pulsar frequency and the construction of integrated pulse profiles require that the observed pulse arrival times be corrected for the relative motion of the satellite and the source. This relative motion introduces a time-varying Doppler shift in the observed

pulsar frequency. The motion of the earth in the sun's gravitational field also affects the frequency of the atomic clock used to generate the UTC time scale. To eliminate these problems each photon arrival time, as measured at the spacecraft, is corrected to the predicted arrival time at the solar system barycenter (the center of mass of the solar system). The barycenter is to a good approximation an inertial reference frame. The only additional effect which might be expected is a constant, unobservable, Doppler shift due to the uniform rectilinear motion of the emitting object relative to the detector.

The expression for the barycentric arrival time of a photon is (Manchester and Taylor 1977)

$$(2\text{-}24)\quad t_{bc} = t_e + (\hat{r}\ (\vec{r}_1 + \vec{r}_2))/c + t_{bi} - D\nu^{-2} + t_r$$

where

t_{bc} = the barycentric arrival time;

t_e = the event time at the satellite;

$\vec{r}_1$ = the position vector of the satellite relative to the earth;

$\vec{r}_2$ = the position vector of the earth relative to the solar system barycenter;

$\hat{r}$ = the unit vector from the earth to the x-ray source;

t_{bi} = a time-of-flight correction to remove the relative effects of binary motion;

c = the speed of light;

D = the dispersion measure;

ν = the photon frequency; and

t_r = the relativistic clock correction.

The various vectors used for the barycentric corrections are shown in Figure 2-5. For x-ray photon energies the dispersion term $D\nu^{-2}$ is negligible. The event time at the satellite is recorded in UTC. As part of the analysis the event time is converted to atomic time A.1 and then corrected for gravitational red shift and the transverse Doppler shift. The relativistic clock correction is given by

$$t = 0.001661\{(1 - e^2/8)\sin(\ell) + (1/2)\, e \sin(2\ell) + (3/8)\, e^2 \sin(3\ell)\} \quad (2\text{-}25)$$

where ℓ and e are the mean anomaly and the eccentricity, respectively, of the earth's orbit. The mean anomaly is the product of the mean angular rate of rotation $2\pi/T$, where T is the orbital period, and the time from perihelion, the orbital position of closest approach to the focus of the orbital ellipse (Smart 1977). The satellite-earth vector, $\vec{r}_1$, is obtained from the OSO production tapes as a function of UTC for the epoch of date. The earth-barycenter vector, $\vec{r}_2$, is obtained from the Lincoln Labs planetary ephemeris designated PEP311 and is given in ET for epoch 1950.0. A list of constants used in the timing analysis is provided in Table 3 (Ash et al. 1967).

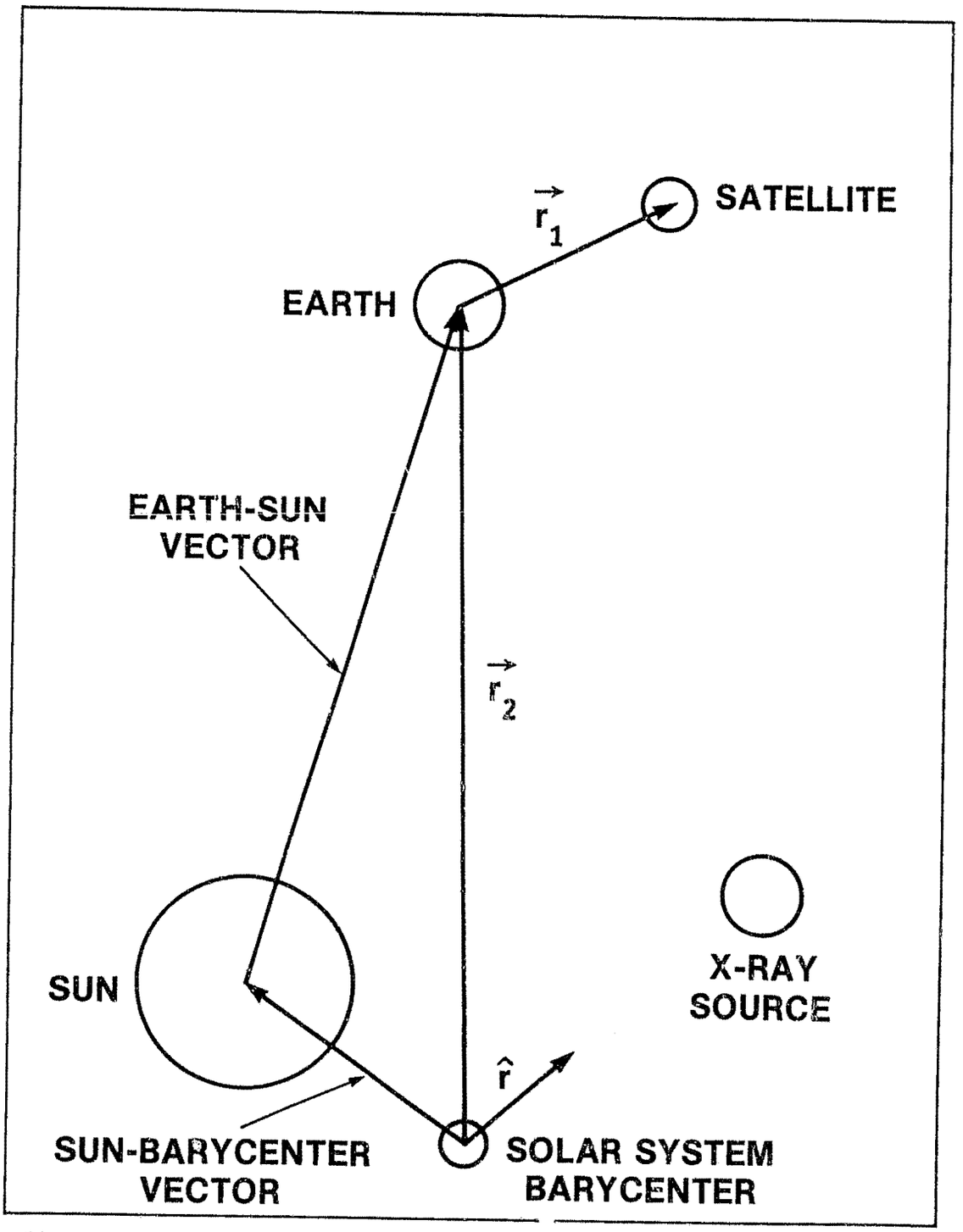

Figure 2-5. The vectors necessary for the calculation of the barycentric time-of-arrival correction.

TABLE 3

Timing Constants Used With The PEP311 Ephemeris

Light Travel Time per A.U.	499.004786 s
Speed of Light	2.997925×10^{10} cm s^{-1}

Strictly speaking, the barycentric arrival time should be calculated for each event. In practice, however, it is sufficient to calculate the timing corrections at the center of each telemetry minor frame. Each minor frame is 0.160 s long; thus, the time for which corrections are calculated may differ from the true event time by as much as 80 ms. The maximum error induced in the barycentric arrival time by this approximation can be estimated by considering the change in the earth's position, Δr_{earth}, in an 80-ms interval;

$$\Delta r_{earth} = (2\pi/T_{earth})(0.080) = 1.6 \times 10^{-8} \text{ A. U.} \tag{2-26}$$

where T_{earth} is the earth's orbital period. This distance, when multiplied by the light travel time per A.U., represents the error in the barycentric arrival time:

$$\Delta t_{earth} = 8.0 \times 10^{-6} \text{ s} \tag{2-27}$$

This error is less than 3% of the instrumental resolving time, and is thus negligible. This is also the maximum error, since the inner product of $\vec{r}_2$ and the source unit vector $\hat{r}$ can make Δt_{earth} smaller but never larger. A similar calculation for the error in the satellite-earth time-of-flight correction produces a value of 2×10^{-6} s, which is again negligible.

The binary time-of-flight correction, t_{bi}, may be expressed for circular orbits by

$$(2\text{-}28) \quad t_{bi} = -r \sin(i) \cos(2\pi (t - t_s)/T)$$

where

r = the light radius of the binary orbit in units of time

i = the inclination of the binary orbit;

T = the binary period; and

t_o = the time of superior conjunction; and

t = the barycentric arrival time exclusive of the binary correction.

The binary correction removes the effects of the relative motion of the x-ray source and the center of mass of the binary system. For binary systems with eccentric orbits, a more sophisticated treatment is required (see Manchester and Taylor 1977).

The events are binned by phase, ϕ, at the barycenter computed from the following expression:

$$(2\text{-}29)\quad \phi(t_{bc}) = \phi_o + \nu_o(t_{bc}-t_o) + \dot{\nu}_o(t_{bc}-t_o)^2/2 + \ddot{\nu}_o(t_{bc}-t_o)^3/6$$

where $\phi_o, \nu_o, \dot{\nu}_o$, and $\ddot{\nu}_o$ are the absolute phase, frequency, frequency derivative, and frequency second derivative of the pulsar at the epoch t_o. These pulsar parameters are usually obtained from other observers because it is difficult to obtain them directly from the High-Energy Scintillation Spectrometer data. For the Crab observations, radio pulsar parameters from Arecibo were used (Gullahorn et al. 1977). The parameters for Her X-1 were provided by Pravdo (1978). Fine adjustment of the parameters is sometimes necessary because of differences in analytic methods, planetary ephemerides, fundamental constants, etc. The absolute phase is particularly sensitive to small differences in timing techniques, and great caution must be exercised in the comparison of phase measurements made by different observers.

2.5 ANALYSIS OF PULSED EMISSION

Several different methods of analysis are currently used to determine the spectral content of pulsed emission. Ideally, the spectrum should be determined as a function of pulse phase. When this is not possible, the following questions may be asked:

1. Is the integrated pulse profile naturally divided into pulsed and nonpulsed regions?

2. What is the spectrum of the nonpulsed component?

3. What is the spectrum of the pulsed component?

4. What is the pulsed fraction of emission?

5. Is the spectrum sensibly constant over each of the above regions so that (2) through (4) are reasonable questions to ask?

The data from the Celestial X-ray Detector lack the statistical significance necessary for the precise determination of the spectrum as a function of phase on a fine scale. Both x-ray sources considered in this work, however, have well-defined pulse profiles so that spectra may be obtained for the pulsed and nonpulsed regions of the integrated pulse profile. Pravdo et al. (1978) suggest that, even though the Her X-1 pulse profile is well defined, spectral changes do occur within the pulsed component of radiation so that information is lost by averaging the spectrum over the entire pulsed component.

Two different methods of pulsed emission analysis were used in this work. The first, following Helmken (1975), is the one traditionally used in the analysis of data from the Crab pulsar. Its use requires the subjective definition by

the observer of pulsed and nonpulsed regions of the pulse profile. Suppose that the integrated pulse profile consists of N phase bins and suppose, for definite ss, that the first M of these correspond to pulsed emission. Then the expressions for the pulsed flux, F_p, average nonpulsed flux, F_{np}, and total time-averaged flux, F_t, are

$$F_p = (1/N)\left[\sum_{i=1}^{M} f(i) - (M/(N-M))\sum_{i=M+1}^{N} f(i)\right]$$

$$F_{np} = 1/(N-M)\sum_{i=M+1}^{N} f(i) \qquad (2\text{-}30)$$

$$F_t = (1/N)\sum_{i=1}^{N} f(i)$$

where f(i) is the source flux in phase bin (i). The above quantities are evaluated for each energy interval to obtain spectra for the nonpulsed, pulsed, and time-averaged x-ray emission.

A useful way to compare results from different experiments is to consider the pulsed fraction of emission, which is defined to be

$$\xi = F_p/F_t \qquad (2\text{-}31)$$

Because the pulsed fraction is a ratio of fluxes at the same energy, its value is independent of systematic effects

associated with interstellar absorption, absorption in any overlying atmosphere, and detector response. It is sensitive, however, to some systematic errors in background determination and subtraction. Moreover, transient pulsed structure in the region defined to be nonpulsed can invalidate the results of the analysis. It should be noted that the determination of the pulsed spectrum is not sensitive to most systematic errors in the determination of background, but it is sensitive to the other systematic effects listed above. Critical consideration of both quantities is, therefore, prudent.

The second method of pulsed emission analysis involves fitting the integrated pulse profile by a Fourier series (Joss et al. 1976). The pulsed fraction is defined to be

$$\zeta = (a_o - m)/a_o \tag{2-32}$$

where a_o is the constant term in the Fourier series and m is the minimum value of the series expansion. The number of terms kept in the expansion depends on the quality of the data and the desired goodness of fit. Because only a finite number of equally spaced data points are being fitted, the resultant series is known as a finite Fourier series. The orthogonality of the Fourier basis functions over discrete, equally spaced points leads to some remarkable results, as

discussed in detail by Hamming (1973). Of particular importance are the convergence properties. For N phase bins, there are only N nonzero terms in the series. If all terms are retained in the expansion, then the series exactly reproduces the original pulse profile. Truncating the series decreases the goodness of fit but has the effect of smoothing the pulse profile. The pulse profile obtained from this truncated series expansion is the one from which spectral parameters are derived.

The above method requires no a priori determination of pulsed and nonpulsed regions and can easily take into acccunt transient pulsed structure. Use of the minimum of the profile rather than the mean of a group of phase bins with low flux, however, results in a systematic overestimate of the pulsed fraction relative to the values obtained using the conventional method discussed above. The Fourier series method also leads to larger uncertainties in the values of pulsed flux and pulsed fraction than does the conventional method. This is a consequence of the use of the minimum value, rather than the mean value of a group of phase bins, with its correspondingly greater uncertainty. For the Her X-1 data presented here, the calculated uncertainty in the pulsed flux was larger by a factor between 2 and 5 for the Fourier series method. For these reasons the first of the above methods was used for the determination of pulsed emission from both Her X-1 and the Crab pulsar.

Chapter 3

EMISSION MECHANISMS

The fundamental challenge of x-ray and gamma-ray astrophysics is to relate the observed source flux to the physical processes taking place in the emitting region and thereby to infer the structure and properties of the source. It is necessary to determine the spatial and spectral distribution of the radiating particles, the mechanism by which these particles lose their energy through radiation, and the modification of the radiation as it propagates from the emitting region to the point of observation. Calculations are usually performed by assuming particular source geometries and radiating particle distributions, considering a number of different energy-loss mechanisms, and comparing the predicted photon spectra with observational results. The source geometry can be quite complicated; several models are discussed in Chapter 4. Mechanisms for radiative energy loss include the synchrotron, cyclotron, and curvature processes, Compton scattering, photomeson production and decay, bremsstrahlung, nuclear transitions, and particle-antiparticle annihilation. Not all of these necessarily produce photons in the high-energy x-ray region of the electromagnetic spectrum;

however, modification of an existing photon energy distribution by Compton scattering or through Doppler, gravitational, or cosmological redshifts can modify the photon spectrum to give significant fluxes of high-energy x-rays.

A formal expression for the observed directional intensity, I(E), of photons with energies between E and E+dE arriving at earth from their point of generation within the production region is the following, taken from Chupp (1976).

$$(3\text{-}1) \quad I(E)\,dE = dE \int d\vec{r}\; q(E,\vec{r})\; \exp -\left\{\int d\vec{x}\; \kappa(E,\vec{x})\right\}$$

photons $cm^{-2}\ s^{-1}\ sr^{-1}$,

where $\vec{r}$ is the vector from the earth to the emitting region and $q(E,\vec{r})$ is the production rate per unit volume, also known as the photon source function. The exponential term in the integral accounts for the absorption of photons in the space between the emitting region and the earth; κ is the absorption coefficient per unit path length of the intervening medium. As discussed by Boldt(1967), the photon source function may be written as the product of the density of radiating particles and the energy emitted in the form of radiation per particle. It is necessary to know both these functions before the structure of the source can be

determined. In the following subsections those emission mechanisms which are believed to be important in the production of x-rays from the Crab pulsar and Her X-1 are discussed. They include synchrotron and cyclotron processes, bremsstrahlung, and Compton scattering.

3.1 SYNCHROTRON RADIATION

The radiation emitted by an electron accelerated in a magnetic field is referred to as cyclotron radiation if the electrons are nonrelativistic and synchrotron radiation if the electrons are relativistic. The radiation from the Crab nebula is most likely synchrotron radiation emitted by particles injected into the nebula from the pulsar (cf. Smith 1977). Because of the very high magnetic field strength in the pulsar magnetosphere, interactions between particles and the magnetic field are expected to play an important role in the electrodynamics of the pulsar. The radiation from ultrarelativistic electrons is considered first; the radiation from nonrelativistic electrons is discussed in a subsequent subsection.

The emission of radiation from a single ultrarelativistic electron is discussed fully by Jackson (1975), Landau and Lifschitz (1962), and Panofsky and Phillips (1962). Several properties of the radiation are (Jackson 1975):

1. The radiation is strongly peaked in the forward direction. The angle, θ_{max}, between the direction of maximum radiation intensity and the electron velocity approaches $1/(2\gamma^2)$ as the electron speed approaches the speed of light. If v is the electron velocity and c is the speed of light, then $\gamma=(1-v^2/c^2)^{-0.5}$. The root-mean-square (RMS) value of the angle of emission approaches γ^{-1} in the same limit. Note that $\gamma = E/mc^2$ where E is the electron energy and m is the electron mass.

2. For a given magnitude of applied force, the radiation emitted when the acceleration of the particle is normal to its velocity is a factor of γ^2 more intense than for acceleration parallel to its velocity.

3. Point (2) allows approximate calculations of the radiation from a relativistic charged particle to be made by considering only the component of the acceleration normal to the particle's instantaneous velocity, i.e. by treating the particle as though it were undergoing instantaneously circular motion.

4. For circular motion the radiation is highly polarized in the plane of the orbit, with 86% of the radiation having its electric vector parallel to the plane of the orbit.

5. For circular motion, the intensity of radiation at frequency ω is proportional to $\omega^{1/3}$ for frequencies much less than the critical frequency, ω_c, and is proportional to $\exp(-2\omega/\omega_c)$ for frequencies much greater than ω_c, where $\omega_c = 3\gamma^3 c/\rho$ and ρ is the radius of curvature of the electron trajectory. The critical frequency is that frequency above which the intensity of radiation is negligible.

The radiation emitted by an electron whose trajectory is constrained by the Lorentz force to follow a curved magnetic field line is known as curvature radiation. The formalism for synchrotron radiation described above, as noted in points 2 and 3, can be used without modification to describe curvature radiation.

Discussion of synchrotron and curvature radiation in astrophysical environments may be found in Ginsburg and Syrovatskii (1964), Ginsburg (1969), Tucker (1975), and Chupp (1976). Chupp presents some useful numerical relationships which follow from the above general properties. The energy of a photon at the maximum intensity of the synchrotron spectrum is

(3-2) $$E_{max} = 5\times10^{-12}\ \gamma^2 B_\perp \quad \text{keV}$$

where B is the magnetic field in gauss perpendicular to the electron's motion. The total power emitted over all frequencies for an ultrarelativistic electron is

$$P_e = 10^{-6} B_{\perp}^2 \gamma^2 \quad \text{kev s}^{-1} \tag{3-3}$$

The time for the electron to lose half its energy by radiation is

$$T_{\frac{1}{2}} = 5 \times 10^8 / (\gamma B_{\perp}^2) \quad \text{s} \tag{3-4}$$

This lifetime is generally very short in astrophysical terms, so that synchrotron emission at optical, x-ray and gamma-ray energies is expected to be very weak except in supernova remnants and near compact objects, where high magnetic fields and continuous energy injection may exist.

The properties of synchrotron radiation from an ensemble of particles are obtained by integrating over the particle distribution function. An important result for ultrarelativistic electrons is that a power-law electron spectrum produces a power-law photon spectrum for a wide range of spectral indices. The photon flux, F, from a volume, V, of trapped electrons with a power-law number spectrum of the form $N(E)=K_e E^{-\alpha}$ is given by the following expression (Chupp 1976):

$$(3\text{-}5) \quad F = 3.27\times10^{-2}\, a(\alpha) K_0 \frac{VB}{R^2}^{(\alpha+1)/2} \left[\frac{2.59\times10^{-2}}{E}\right]^{(\alpha+1)/2}$$

photons cm^{-2} s^{-1} Mev^{-1}

where R is the distance from the source to the observer and $a(\alpha)$ is a constant whose value lies between 0.3 and 0.07 for values of between 1 and 5 (Ginzburg 1969). It is assumed that no significant radiation is emitted by the electrons near the endpoints of the electron spectrum.

The conditions under which the above formulas were derived must be stressed (Chupp 1976):

1. Ultrarelativistic electrons are moving in a constant, homogeneous magnetic field with no other fields present;

2. the influence of the ambient medium is negligible;

3. particle-particle interactions are neglected; and

4. the electron energy is such that $\gamma << 10^8/B^{0.5}$. This requirement essentially states that the electron will not lose a significant fraction of its energy during a single orbit (Ginzburg 1969).

3.2 CYCLOTRON RADIATION

Cyclotron radiation, here defined to be the radiation emitted by a nonrelativistic or mildly relativistic electron undergoing circular motion in a magnetic field, is not usually considered in astrophysics because of the normally low frequency of the emitted radiation. It is important, however, wherever strong magnetic fields exist. Examples of astrophysical sites where cyclotron radiation is important include solar flares, white dwarfs, and neutron stars (Tucker 1975). Cyclotron processes have been postulated as the source of the spectral feature from Her X-1 observed by Trümper et al. (1978), so a brief discussion of these processes is given here. More detailed descriptions may be found in the papers of Daugherty (1978), Daugherty and Ventura (1978), Canuto and Ventura (1977), and in the book by Bekefi (1966).

Cycloton processes in very large magnetic fields must be treated quantum mechanically even for mildly relativistic electrons (Daugherty 1978). The solution of the Dirac equation in an intense magnetic field yields energy eigenvalues, W(j), such that

$$W^2(j) = p^2c^2 + m^2c^4(1 + 2jB/B_c) \quad j = 0,1,2,... \tag{3-6}$$

where p is the electron momentum parallel to the magnetic field and $B_c = m^2c^3/(e\hbar)$ is the critical magnetic field strength with a numerical value of 4.413×10^{13} gauss (Bussard 1978; Daugherty and Ventura 1978). Note that B_c is the magnetic field strength for which the energy of a photon at the Larmor frequency is equal to the electron rest energy. Daugherty and Ventura (1978) have calculated discrete emission rates and absorption cross sections and find that the lifetime of an electron in an excited state is of the order of 10^{-16} s. Because this time is much less than collisional time scales for reasonable densities, relatively cool electrons will spend most of their time in the ground state (Bussard 1978). It is necessary, therefore, to populate the upper levels before transitions can occur. Several mechanisms have been suggested for the population of the excited states. Bussard (1978) has considered energy loss from infalling protons with energies of the order of 200 MeV. Basko and Sunyaev (1975) suggest that line peaks should reach the blackbody intensity but that the bremsstrahlung continuum would remain considerably below it. This is because of the high Thomson opacity required to maintain the observed luminosity from accretion onto a small area (cf. Meszaros 1978). The high-energy states in this case are excited thermally. Bonazzola et al. (1978) regard thermal excitation as unlikely.

The cyclotron emission lines can be broadened by a variety of mechanisms (Bekefi 1966): radiation broadening, collisional broadening; Doppler broadening, self-absorption, plasma dispersion effects, and nonuniformity of the magnetic field. The spectral features observed to date have not been detected with sufficient resolution to determine the line shape precisely; however, Chapter 6 contains a discussion of the general properties of the line emission which can be deduced from the observations.

3.3 BREMSSTRAHLUNG

An electron traversing an ionized gas can lose energy by either nonradiative or radiative processes. Examples of the nonradiative processes include the excitation of ionic states and the generation of plasma waves. In this section the radiative energy-loss mechanism of bremsstrahlung is discussed. The astrophysical sites where it is expected to be an important emission mechanism include the envelopes of supernovae and radio galaxies (Ginzburg 1969) and x-ray binaries (Blumenthal and Tucker 1974). For nonrelativistic electrons the intensity of radiation, I, as a function of frequency, ω, and impact parameter, b, is given by Jackson (1975) as

$$(3\text{-}7)\quad I(\omega,b) = \frac{8}{3}\left[\frac{z^2e^2}{mc^2}\right]^2\left[\frac{Z^2e^2}{c}\right]\left[\frac{c}{v}\right]^2\frac{1}{b^2} \qquad \omega < v/b$$

$$= 0 \qquad \omega > v/b$$

where Ze is the charge of the scattering center (here assumed stationary) and ze is the charge of the incident particle. The radiation cross section, $\chi(\omega)$, is determined by integrating over all possible impact parameters. The result is

$$(3\text{-}8)\quad \chi(\omega) = \frac{16}{3}\left[\frac{Z^2e^2}{c}\right]\left[\frac{z^2e^2}{mc^2}\right]^2\frac{c^2}{v^2}\ln(Y)$$

where Y is the ratio of maximum and minimum impact parameters. It is here that the classical calculation breaks down, because the classical minimum impact parameter, $b_{min} = zZe^2/mv^2$, does not take into account the quantum nature of the electron momentum. By setting b_{min} approximately equal to the de Broglie wavelength of the electron, $b_{min} = \hbar/mv$, a much better approximation to the bremsstrahlung spectrum is obtained. In this case, $Y = mv^2/\hbar\lambda$, where λ is a factor of order unity which takes into account the uncertainties in the exact values of the integration endpoints. For rigorous results, or when the radiated energy is a significant fraction of the incident particle energy, the Bethe-Heitler equation should be used (Bethe 1957). For an optically thin, hot, completely

ionized plasma, the energy radiated per unit volume of plasma at temperature T with ion density n_i cm^{-3} and electron density n_e cm^{-3} is (Chupp 1976)

$$(3\text{-}9) \qquad W = \frac{32\ 2^{\frac{1}{2}} e^6 Z^2 n_i n_e (kT/m)^{0.5}}{3\pi^{\frac{1}{2}} mc^3 h} \qquad \text{erg cm}^{-3}\ \text{s}^{-1}$$

For a neutral hydrogen plasma,

$$(3\text{-}10) \qquad W = 1.57\text{x}10^{-27}\ n_e^2\ T^{0.5} \qquad \text{erg cm}^{-3}\ \text{s}^{-1}$$

Equations (3-9) and (3-10) are valid for 10^5 K < T < 10^{10} K. The differential energy spectrum for the same temperature range is

$$(3\text{-}11) \qquad \frac{dN}{d\nu} = \frac{7.7\text{x}10^{-38}\ n_e^2\ \exp(-h\nu/kT)}{4\pi^{\frac{1}{2}}\ T^{0.5}} \qquad \text{erg cm}^{-3}\ \text{s}^{-1}\ \text{Hz}^{-1}$$

3.4 COMPTON SCATTERING

Compton scattering, the inelastic scattering of photons by charged particles, can redistribute the energy of the photon field. Expressions for the scattering cross section and energy of the scattered photon, for the case of an electron initially at rest, are well known (cf. Evans 1955). The differential scattering cross section, for unpolarized incident radiation and photon energies much less than the electron rest mass, is

$$(3\text{-}12) \qquad (d\sigma/d\Omega) = (r_o^2/2)(1+\cos^2\theta),$$

where θ is the angle between the incident and scattered photon directions and $r_o = e^2/mc^2$ is the classical electron radius. The integral of equation (3-12) over all angles is just the Thomson scattering cross section, $\sigma_T = (8/3)r_o^2 = 6.65\times10^{-25}$ cm^2. The energy, E , of an individual scattered photon is

$$(3\text{-}13) \qquad E = \frac{E_o}{1 + (E_o/mc^2)(1 - \cos\theta)} ,$$

where E_o is the incident photon energy.

In astrophysical applications a more interesting situation arises when a low-energy photon is scattered from a relativistic electron. This process is sometimes called inverse Compton scattering because the scattered photon energy is larger than the initial photon energy.

Several assumptions are usually made relating to the electron and photon distributions. The first is that the photon distribution is isotropic; this allows a determination of the mean electron energy loss and the mean scattered photon energy to be made. The second assumption is that the initial phcton energy, E , is much less than the electron rest mass. The total Compton scattering cross

section is then just the Thomson cross section. In the opposite extreme, when the photon energy is much greater than the electron rest mass, the cross section is given by the Klein-Nishina equation. This case is not of importance for the sources of interest here. Typical incident photon spectra include ambient starlight and the microwave background radiation; for these examples the former condition on the photon energy is well satisfied.

To calculate the average energy loss per unit time of an electron in a photon field, it is first necessary to calculate the mean energy, E_γ, of the scattered photons. The expression for E_γ is (Blumenthal and Tucker 1974)

$$E_\gamma = (4/3)\gamma^2 \bar{E}_o \tag{3-14}$$

where $\bar{E}_o$ is the mean energy of the incident photon distribution, defined by

$$\bar{E}_o = \int dE_o E_o n(E_o) \Big/ \int dE_o \cdot (E_o) \tag{3-15}$$

where $n(E_o)$ is the initial photon distribution function. The average energy loss rate of an electron in the photon field is then the product of the collision rate and the mean energy loss per collision (Chupp 1976)

(3-16) $$-(dE/dt) = c\, n(E_o)\, \sigma_T\, E_\gamma$$

The rate of energy loss in both the synchrotron process and Compton scattering is proportional to the electromagnetic energy density and to the square of the electron energy. This similarity is not coincidental; indeed, the synchrotron process may be viewed as the interaction of virtual photons in the magnetic field with electrons (cf. Jones 1965). As a result, Compton scattering dominates the electron energy loss when $(4/3)\bar{E}_o > B^2/8\pi$, and vice versa.

The situation for which most calculations have been performed is the case of a power-law electron spectrum and a blackbody photon spectrum. Stecker (1971) has presented the resulting photon spectrum, evaluating the coefficients numerically.

(3-17) $$I_\gamma(E) = 6.22\times10^{-21} L\ 10^{-2.962 f(\alpha)}\ K_e T^{(\alpha+5)/2}\ E^{-(\alpha+1)/2}$$

$$(\mathrm{cm^2\ s\ sr\ GeV})^{-1},$$

where L is the effective path length for gamma-ray production and the electrons have the following energy spectrum:

(3-18) $$I_e(E) = K_e E^{-\alpha}$$

The coefficient $f(\alpha)$ has values between 0.84 and 1.4 for values of α between 1 and 4.

The lifetime, t_c (= $E/(dE/dt)$), for an electron undergoing Compton scattering in the Thomson limit is (Blumenthal and Tucker 1974)

$$t_c = 3mc/(4\sigma_T \gamma \bar{E}_o) = (2.1 \times 10^7)/(\gamma \bar{E}_o) \quad (s) \tag{3-19}$$

where E_o is measured in erg cm^{-3}. For compact astrophysical sources the Compton lifetime may be shorter than the synchrotron lifetime.

The above results are subject to modification in the presence of superstrong magnetic fields. Lodenquai et al. (1974) have shown that, if a photon's electric vector is normal to the magnetic field and its frequency is much less than the cyclotron frequency, then the cross section, , is modified as follows:

$$\sigma_T(H) = (\omega/\omega_H)^2 \sigma_T(0) \tag{3-20}$$

where $\sigma_T(0)$ is the Thomson scattering cross section in the absence of the field H and ω_H is the cyclotron frequency. This anisotropy arises because the electron cannot move freely in directions normal to the magnetic field but can

move freely parallel to the field lines. As a consequence the photon opacity becomes anisotropic. Basko and Sunyaev (1975) have suggested that this effect provides a natural mechanism for the beaming of x-rays from binary x-ray sources. This idea will be discussed further in Chapter 6.

3.5 ELECTROMAGNETIC WAVE PROPAGATION IN PLASMAS

Several models for the beaming of x-ray emission require a knowledge of electromagnetic wave propagation in plasmas. A detailed treatment of plasma waves is beyond the scope of this discussion; consideration of a simple model, however, reveals the essential physics. In this model a neutral, stationary, uniform plasma is imbedded in a uniform, homogeneous magnetic field (cf. Pacholczyk 1970). The propagation of waves is treated as a perturbation of the plasma, and the equations describing the plasma (the Maxwell equations, the continuity equation, and energy and momentum conservation) are linearized by keeping only the first powers of the perturbed quantities. The resulting set of equations is solved assuming a solution in the form of a propagating wave. The equations have a solution if and only if the determinant of the coefficients is zero. Setting the determinant equal to zero produces the dispersion relation, which relates the wavenumber of the propagation, k, to the frequency, ω. In general the dispersion relation is of fourth order in k^2. The radiation modes corresponding to the

four roots of this equation are known as the ordinary, extraordinary, electron, and ion modes. If there is no transverse component of the external field, then the ordinary and extraordinary modes are transverse electromagnetic waves and the electron and ion modes are longitudinal. It is the electromagnetic modes which are of interest in models for Her X-1.

The difference between the ordinary and extraordinary modes is best illustrated by the functional form of the index of refraction. If, in addition to the assumptions made in the previous paragraph, the plasma is assumed to be completely ionized hydrogen, and if ionic motion is neglected, then the index of refraction, n , may be written

$$n^2 = 1 - \omega_p^2/(\omega(\omega \pm \omega_H)) \qquad (3\text{-}21)$$

where the + (-) sign refers to the ordinary (extraordinary) mode, is the Larmor frequency, and $\omega_p = (4\pi e^2 n_e/m)^{0.5}$ is the plasma frequency. Note that the index of refraction for the extraordinary mode becomes imaginary for values of the frequency near the Larmor frequency, so that the extraordinary mode is strongly attenuated at those frequencies. The ordinary mode is a left-circular polarized wave and the extraordinary mode is a right-circular polarized wave. The rotation of the extraordinary mode polarization is in the same sense as the motion of an

electron in the magnetic field (Denisse and Delcroix 1963); this is why the extraordinary mode interacts strongly with the plasma and why the ordinary mode is largely unaffected by it. It should be noted that, in the application of this process to the beaming of radiation from Her X-1, temperatures of interest range from 1 to 50 keV. Expected values of the optical depth to electron scattering range from $\tau \sim 1$ to $\tau \sim 30$ in various regions of the accretion column. The implications of this interaction for models of Her X-1 are discussed further in Chapter 6.

Chapter 4

STRUCTURE OF PULSARS AND X-RAY BINARIES

The periodic emission of electromagnetic radiation observed from a variety of astrophysical sources, is believed to originate on or near compact objects. The remarkable stability of the periodicity observed from most sources argues for rotational motion rather than pulsations as the cause of the periodicity. The various types of compact objects which could serve as the source of such periodic emission include dwarf stars, neutron stars, and black holes. In many instances, which of these is involved can be inferred from the characteristics of the emitted radiation. Radio pulsars, for example, are believed to be rotating neutron stars. With one known exception they are not members of multiple star systems. The frequency of the periodic emission, and thus of the inferred neutron-star rotation rate, is observed to decrease with time. X-ray pulsars, on the other hand, usually occur in binary systems. Modulations are observed at the frequency of the binary motion and at the rotational frequency of the neutron star. It should be noted that not all x-ray binaries are pulsars in this sense; if the compact object is a dwarf star or a black hole, there may be no well defined modulation

corresponding to the rotational frequency of the compact object.

The celestial objects considered in this thesis include one in each of the above classes. The pulsar in the Crab nebula is an isolated pulsar and it is similar to other radio pulsars with respect to its radio emission. It is unique, however, in that it emits pulsed optical, x-ray, and gamma-ray photons simultaneously with the radio emission. Her X-1 is a rotating neutron star in a binary system. The emission mechanisms and source dynamics are entirely different in the two cases. A description of these objects as they are presently understood is given here, with emphasis on those aspects related to the emission of high-energy x rays.

4.1 TIMING AND STRUCTURE

The observation of rapid temporal variability in the radiation from celestial objects immediately provides information about their structure which would not otherwise be available. In this section some consequences of rapid variability are discussed, including both general arguments based solely on the existence of such variations and the results of some detailed calculations based on extended observations.

The power of temporal analysis as a tool in astrophysical investigations is immediately demonstrated by the implications of rapid variability for the size of the emitting region. The light travel time across the emitting region cannot be any longer than the time scale of the observed variations as measured, for example, by the width of an emitted radio pulse. The median period of a radio pulsar is 0.65 s; the width of subpulses emitted by many pulsars is 5×10^{-4} s. The maximum dimensions of the emitting region are thus on the order of 5×10^{-4} c, or 1.5×10^{7} cm (Manchester and Taylor 1977). This dimension is about 10% of the radius of a white dwarf (Harwit 1973).

The precisely periodic emission observed from pulsars also restricts models of source structure. Smith (1977) reviews the various proposals made between 1966 and 1969 by various investigators. Melzer and Thorne (1966) showed that a white dwarf could have a resonant period for radial oscillations of about 10 s. Corrections for relativistic and elastic effects reduced the minimum period to about 2 s. The period for fundamental modes in neutron stars was found to be from 1 to 10 ms. The period of the subsequently discovered Crab pulsar (33ms) was thus too short to be a dwarf oscillation and too long to be a neutron-star oscillation.

The possibility that the observed pulsar periods were the orbital periods of satellites revolving about condensed stars was ruled out by the work of Ostriker (1968) and Pacini and Salpeter (1968). Ostriker showed that the time scale for significant change in the period due to gravitational radiation is $\tau_g = 2.7 \times 10^5$ m/M , where m is the mass of the satellite and M is the mass of the condensed star. This is much too short, except for very small satellite masses, to account for the observed stability of pulsar periods. Pacini and Salpeter (1968) concluded that such a satellite must have a mass no larger than 3×10^{-8} solar masses to account for the stability and must be smaller that 20 meters in diameter to avoid disruption by strong tidal forces in the gravitational field of the condensed star.

The rotation of white dwarfs can also be ruled out on the basis of stability; the most rapid rotation rate of a white dwarf is about 1 s, again too slow to explain observed periods. Neutron stars, on the other hand, are stable at rotation periods as short as 1 ms. By the process of elimination, then, the rotating neutron star became the accepted model for radio pulsars.

The results presented in this thesis pertain to the x-ray emission of the Crab pulsar and not to the radio emission.

Because the x-ray and radio emission exhibit the same 33-ms periodicity, however, many conclusions about source structure inferred from the radio observations can also be inferred from the x-ray emission. Moreover, the emitted x-ray flux above 20 keV is not affected by interactions in the interstellar medium such as Rayleigh-Gans scattering and dispersion.

The temporal analysis of emission from x-ray binaries provides the same kind of information as the radio emission from pulsars. No radio emission has been detected from many x-ray binaries; in these cases x-ray emission provides the only information available for the determination of source structure and dynamics.

4.2 PULSARS

Since the identification of pulsars as rotating neutron stars, many calculations have been performed in an attempt to relate the properties of the observed radiation to detailed models of the emission process. These calculations range from simple order-of-magnitude estimates of mass, rotation rate, and magnetic field strength (cf. Dyson 1970) to detailed magnetohydrodynamic calculations of magnetospheric structure (Sturrock 1971; Ruderman and Sutherland 1975; Cheng et al. 1976). Aspects of pulsar structure inferred from radio observations have been reviewed by Smith (1977) and Manchester and Taylor (1977).

Theories for the emission of radiation from rotating neutron stars must be based on certain simplifying assumptions about the structure of both the star itself and the surrounding magnetosphere. The simplest assumptions, which guided early work, included uniform magnetization and infinite conductivity inside the neutron star, and either aligned or anti-aligned angular momentum and magnetic moment (Goldreich and Julian 1969). In this way Goldreich and Julian calculated the motion of particles in the magnetosphere. Mestel (1971) showed that the general structure of the magnetosphere was unchanged if the geometrical restrictions on the relative orientation of the magnetic moment and the rotational axis were relaxed. Sturrock proposed coherent pair creation in the strong electromagnetic field as the mechanism for the observed emission. The model described below is due to Ruderman and Sutherland (1975); Cheng and Ruderman (1976); Cheng et al. (1976). It is typical of pulsar theories presently available for radio emission from pulsars and easily generalizes to account for the optical and x-ray emission.

The neutron star rotates with its magnetic moment anti-aligned with its angular velocity. The rotating magnetic field, which is expected to be dipolar except very near to the surface, and the assumed infinite conductivity inside the star give rise to a very large induced electric

field. The interior electric field, E_{in}, and charge density, ρ_{in}, are given by

$$(4-1) \quad E_{in} = -B_p \Omega^* r_\perp \hat{e} / c \; ; \quad \rho_{in} = -B_p \Omega / (2\pi c)$$

where $r_\perp = r \sin\theta$ is the cylindrical coordinate normal to the rotation axis, Ω^* is the angular velocity, and B_p is the value of the surface magnetic field at the pole. For a corotating perfectly conducting magnetosphere, the exterior field, E_{ex}, and charge density, ρ_{ex}, are

$$(4-2) \quad E_{ex} = -(\vec{\Omega}^* \times \vec{r}) \times \vec{B} / c \; ; \quad \rho_{ex} = -\vec{\Omega}^* \vec{B} / (2\pi c),$$

where the above equations are correct to order $(v/c)^2$. The exterior electric field under these assumptions is essentially quadrupolar. If both positive and negative charges were easily pulled from the surface by the electric field, the result would be streams of particles leaving the star, with the sign of the current depending on the sign of the electric field at the origin of the stream. Charge neutrality is maintained. It was originally thought that for all pulsars except the rapidly rotating Crab pulsar the surface binding energy of the ions was too strong to be overcome by the induced electric field; thus, positive charge could not flow from the surface to maintain the charge distribution in the magnetosphere. The result in this case would be the formation and growth of a gap between

the surface of the neutron star and the inner surface of the magnetosphere. This gap, for which $E \cdot B \neq 0$, will occur at the poles of the neutron star, and will lead to a potential difference of

$$V = \Omega B_p h^2/c \qquad h<<R \tag{4-3}$$

with an electric field normal to the surface and of strength

$$E = -2\Omega B_p h/c \qquad h<<R \tag{4-4}$$

where h is the height of the gap, Ω is the rotation rate of the magnetosphere, and R is the radius of the neutron star (see figure 4-1). The rotation rate, Ω, of the magnetosphere is not, in general, equal to the rotation rate, Ω^*, of the neutron star. The gap will grow at nearly the speed of light, so that the field E will rapidly become large enough to break down by the formation of electron-positron pairs (Sturrock 1971; Ruderman and Sutherland 1975). The electrons are accelerated toward the star's surface. The positrons are accelerated away from the surface and emit curvature radiation. The curvature radiation so produced can create more electron-positron pairs. These secondary pairs are believed to be responsible for the coherent microwave emission from radio pulsars.

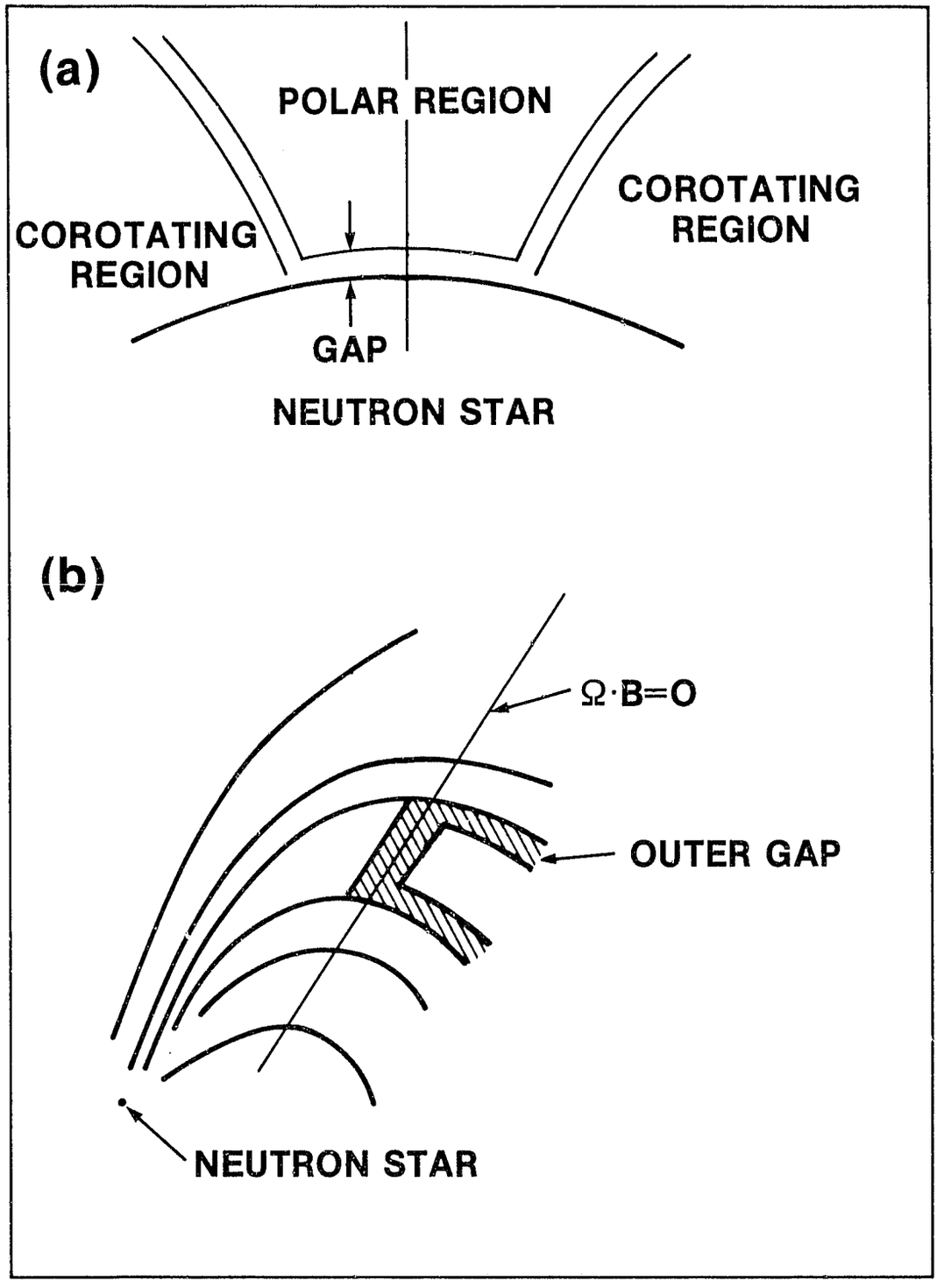

Figure 4-1. (a) The structure of the inner gap at the surface of the neutron star (after Ruderman and Sutherland 1975); (b) Structure of the outer gap (after Cheng, Ruderman, and Sutherland 1976).

The above theory, developed by Ruderman and Sutherland (1975) and based on the work of Sturrock (1971), has required some modification. New estimates of the ion binding energy were lower than those previously made; the lower binding energy prevents the formation of the necessary gap potentials and requires an alternative mechanism for the production of the high-energy curvature radiation and the subsequent pair production. Cheng and Ruderman (1976) proposed Lorentz boosting as a possible mechanism. Radio photons are Compton scattered to gamma-ray energies sufficient for pair production by the relativistic particles in the magnetosphere.

The separation between the primary pulse and the interpulse of the Crab integrated pulse profile can be interpreted as relativistic aberration of pulses emitted 180° apart in a rotating system. The observed separation requires that the emission region lie well away from the surface of the neutron star. Cheng and Ruderman (1976) have proposed a theory for the radio, optical, and x-ray emission from the Crab which invokes gaps in the outer magnetosphere. The properties of the outer gaps are very similar to those of the inner gaps described above. The gap formation will occur wherever $\vec{\Omega}\cdot\vec{B}$ vanishes, and in the outer magnetosphere does not depend on a particular orientation of the magnetic moment and rotation axis. The gap again breaks down by pair

creation. The radiation in this case, however, is produced by the synchrotron process. It should be noted that an outer gap will be formed whether or not an inner gap is formed. In the case of the Crab, both an inner and an outer gap are presumed to form. The radio precurser is formed in the inner gap, while the remaining radiation is emitted from the outer gap. The optical and x-ray photons result from Compton scattering, and hard x rays and gamma rays are produced by the synchrotron and curvature processes.

4.3 X-RAY BINARIES

Observational evidence suggests that x-rays are generated in binary systems by the accretion of matter from a normal primary star onto a compact secondary star. The strong gravitational field of the secondary accelerates the accreting matter and provides the energy for the emitted radiation. While neutron stars and black holes are the most likely candidates for the secondary star in intense x-ray sources, there is some evidence that a white dwarf is the compact component in some weak x-ray binaries.

The mechanism by which matter from the primary accretes onto the compact object depends on the geometry of the equipotential surfaces in the binary system. Figure 4-2 shows a diagram of equipotential surfaces for a typical system. Of particular importance are the inner Lagrangian

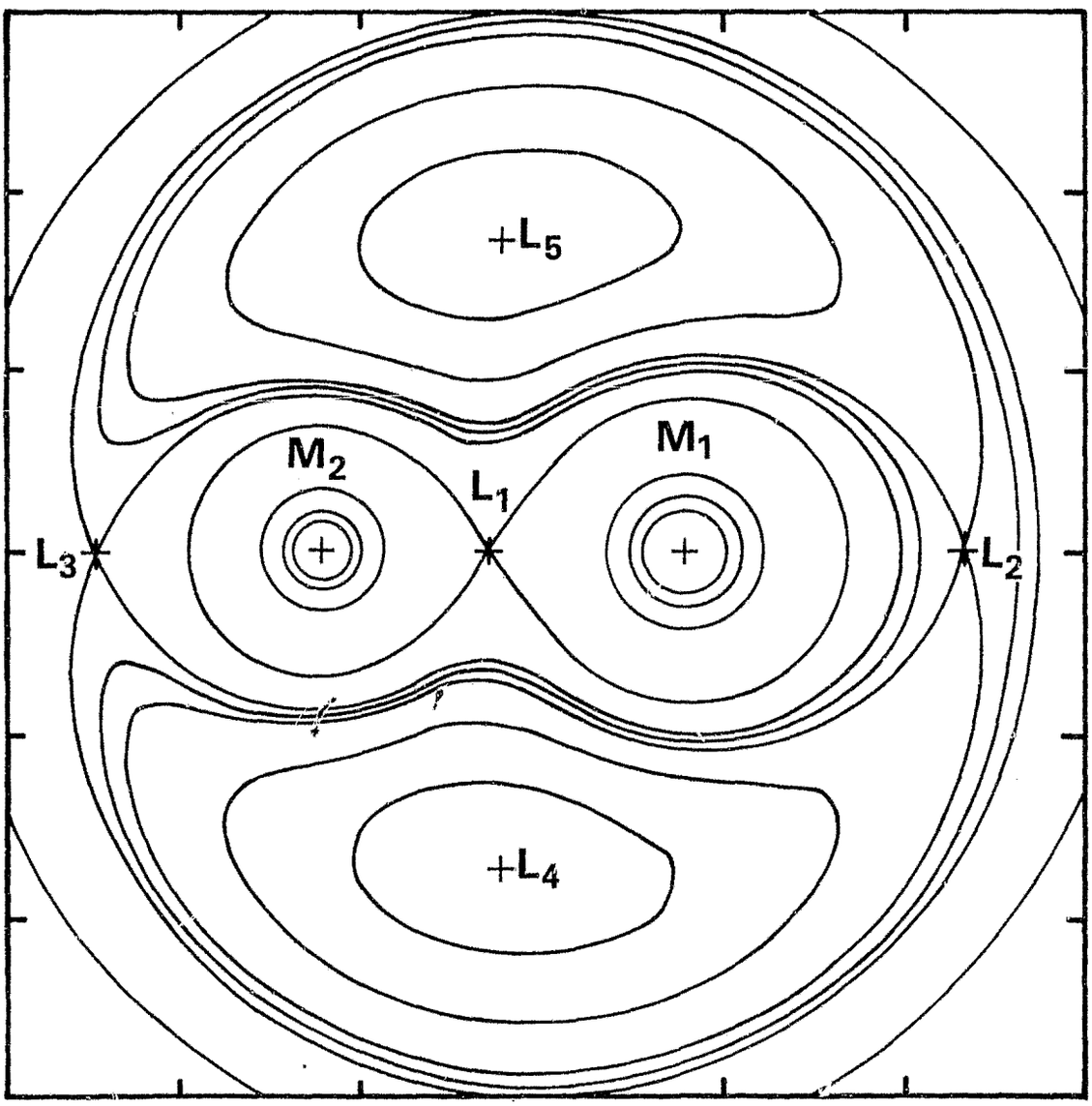

Figure 4-2. The gravitational equipotential surfaces for a model binary system (after Rose 1977). L_1 is the inner Lagrangian point and the equipotential surfaces passing through L are the so-called Roche lobes.

point and the equipotential surfaces which pass through it (the so-called Roche lobes). Note that a test particle placed at the inner Lagrangian point is in a state of metastable equilibrium. If the normal star is completely contained within its Roche lobe, then matter can accrete onto the compact object by a stellar wind. Petterson (1978) has recently suggested that flaring and streaming behavior also contribute significantly to the mass accretion in such systems. If, on the other hand, the normal star fills its Roche lobe, matter will stream through the inner Lagrangian point and onto the compact component and the accretion rate is likely to be considerably higher.

The luminosity, L, expected from mass accretion may be written as

$$L = GM\dot{M}/R \tag{4-5}$$

where G is the gravitational constant, M is the secondary mass, R is the secondary radius, and $\dot{M}$ is the mass accretion rate. Observed luminosities (10^{36}- 10^{38} ergs s^{-1}) suggest mass accretion rates between 10^{-8} and 10^{-10} solar masses per year. Roche-lobe overflow is much more efficient than solar wind for the generation of x-rays, but at high accretion rates ($>10^{-6}$ $M_\odot$ y^{-1}) the x-rays are reabsorbed in the optically thick accretion column and cannot be observed.

The behavior of the accreting matter near the compact object may be quite complicated. If the matter has angular momentum, it is likely that an accretion disk will be formed (Prendergast and Burbidge 1968). Centripetal force prevents matter from free-falling onto the surface of the neutron star. In the absence of viscous forces and magnetic fields, the matter would remain in Keplerian orbit about the neutron star. The magnetic field forces the matter to corotate with the neutron star at a radius r_A, called the Alfven radius. In general, this radius is not identical to the corotation radius, r_c, determined from centripetal forces alone. For $r_A \neq r_c$ conservation of angular momentum requires spin-up or spin-down of the neutron star. Viscous forces and the resultant turbulence eventually cause matter in the accretion disk to fall onto the star's surface. The magnetic field requires the point of impact to be at the magnetic poles of the star. The x rays are produced at these points. Some part of the accretion disc may obscure the x-ray production region from view depending on the geometry of the system. Thus, the disk structure affects the radiation in two ways: it determines the exact nature of the accretion onto the neutron star, thereby determining the particle source function; and it alters the emitted photon spectrum via scattering and absorption.

Pringle (1977) has recently reviewed the present understanding of accretion disks and concludes that the process of accretion onto a magnetized neutron star is so complex that reliable calculations of the expected radiation have not been possible. Nonetheless, it is instructive to examine the general predictions of several simple models.

Lamb et al. (1973) have considered the case of spherically symmetric accretion onto a rotating, magnetized neutron star. The accreting matter is channelled along the magnetic field lines and falls onto the surface at the poles of the field, thereby forming an accretion column above the poles. The x-rays are generated at a hot spot on the surface of the star which has an area of 1 km^2. The optical depth vertically through the accretion column is expected to be much larger than that normal to the column for photon energies much less than the cyclotron energy. The radiation which escapes from the star is thus emitted preferentially normal to the magnetic axis. Pulsed emission will be observed if the magnetic axis and the rotation axis are not coincident. This beaming geometry is sometimes referred to as a fan-beam geometry.

Gnedin and Sunyaev (1974) suggest that the radiation emitted from the poles of a neutron star will be normal to the magnetic axis if the emission mechanism is the cyclotron

process. They propose two mechanisms, however, by which radiation could be emitted parallel to the magnetic field lines. One such mechanism involves the existence of an anisotropic Maxwellian plasma for which the temperature of particles moving parallel to the field is greater than the temperature of particles moving normal to the field. Another depends on the modification of the Thomson scattering cross section in strong magnetic fields as described in Chapter 3. Because the cross section varies as $\sin^2(\theta)$, where θ is the angle between the the magnetic field and the photon momentum vector, the accretion column is more transparent to photons travelling along field lines than to those travelling normal to the field lines. This produces a so-called pencil-beam geometry.

The radiation transfer characteristics near the neutron star surface are treated by Basko and Sunyaev (1975). They propose an accretion funnel rather than an accretion column based on details of the interaction between the accretion disk and the magnetosphere. The general properties of the radiation, however, are not expected to depend strongly on the exact shape of the hot spot on the surface of the neutron star. Basko and Sunyaev also favor the pencil-beam geometry.

Petterson (1975) proposes a warped accretion disk to account for the 35-day ON-OFF cycle observed in Her X-1. This warping could arise from precession of the primary star. The OFF-state corresponds to times when the x-ray source is obscured by dense matter in the disk. The intensity dips, which occur approximately every 1.6 days, may also be explained in terms of the obscuration by the disk.

The observed x-ray emission from Hercules X-1 is discussed in terms of the above models in Chapter 6.

Chapter 5

THE CRAB PULSAR

5.1 INTRODUCTION

The emission of electromagnetic radiation from the pulsar in the Crab nebula has been studied by many observers. The general shape of the integrated pulse profile, consisting of a primary pulse followed 13.4 ms later by an interpulse, remains unchanged over 16 decades in photon energy. Typical pulse profiles from radio energies to high-energy gamma-ray energies are shown in Figure 5-1. Note that a third peak, known as the precurser, occurs below about 700 MHz in the radio data. Variability in both the temporal and spectral characteristics of the radiation has been reported in several energy bands.

The strongest evidence for variability is found in the radio observations, which have been quite extensive. Rankin et al. (1974) observed changes in the pulsar intensity by a factor of three with a characteristic fluctuation time of 30 days. These variations occur in the precurser, primary pulse, and interpulse with a high degree of correlation. Variability in the radio emission has also been detected from pulse to pulse. Sutton et al. (1971) reported that

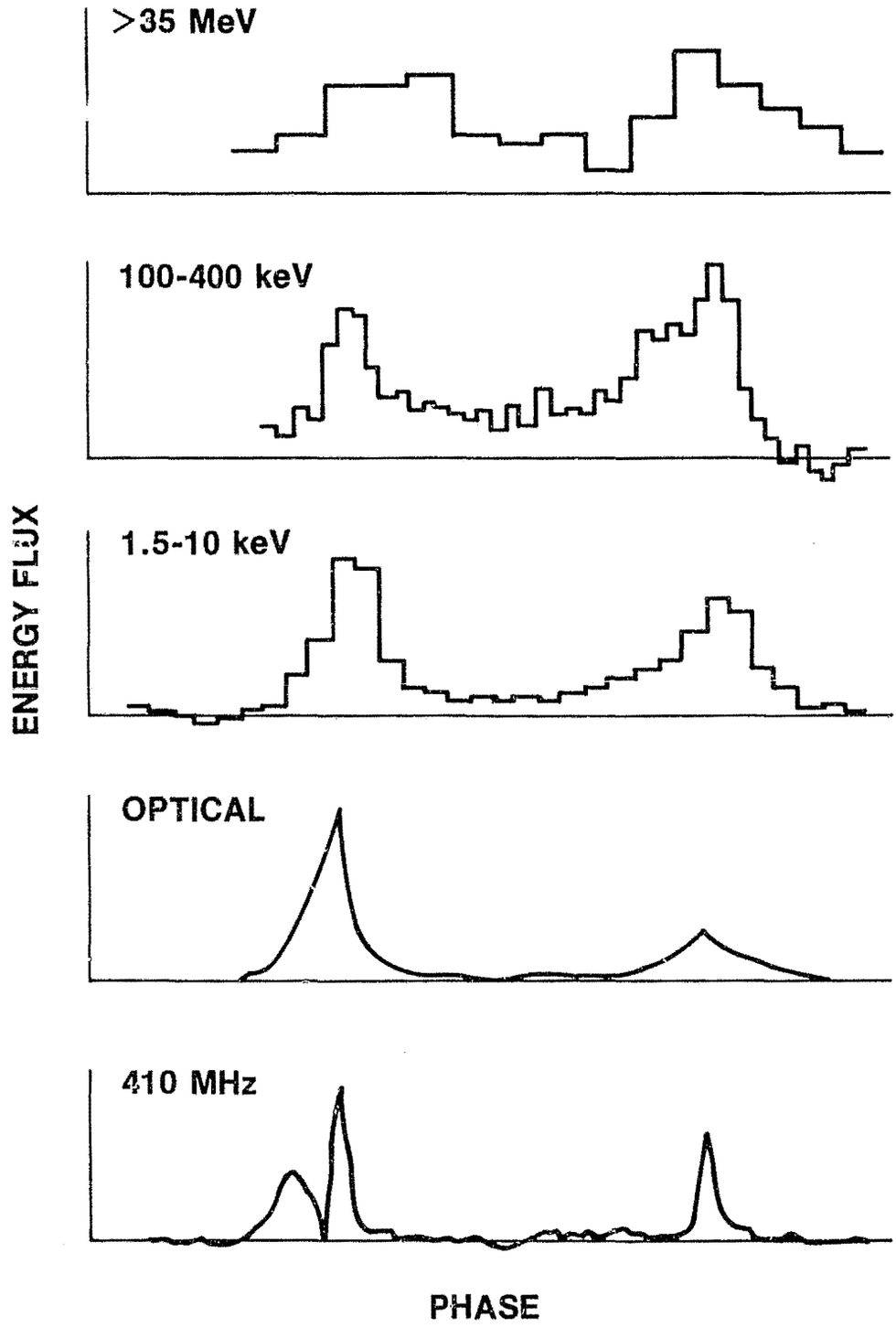

Figure 5-1. Integrated pulse profiles of the Crab pulsar at various energies (data from Manchester 1971; Warner et al. 1969; Rappaport et al. 1971; Kurfess 1971; and Kniffen et al. 1977).

"giant" pulses occur about once every 5 to 10 minutes. The flux density in these pulses can exceed the flux density from the entire nebula. Hankins and Rickett (1975) reported one such pulse whose flux density was 60 times that of the nebula.

In contrast to the radio emission, the optical emission from the pulsar shows no variations in intensity or pulse profile over short time scales (Hegyi et al. 1971). Photometric measurements made over the last few years show less than 0.05 magnitude variation (Kristian 1971).

When discussing variability in the x-ray and gamma-ray emission from the Crab pulsar, it is customary to define pulsed and nonpulsed regions of the integrated pulse profile in the following way. The pulsed emission region of the profile contains the primary pulse, the interpulse, and the phase interval between them. The precise width of the pulsed emission is subjective; values used by various observers lie between 50% and 67% of the integrated pulse profile. The different widths chosen reflect not only possible changes in pulsed structure, but possible systematic errors as well. For example, folding the data using slightly incorrect pulsar parameters would result in an apparently broader pulsed emission region.

The remaining part of the pulse profile is denoted the nonpulsed emission region of the profile. The integrated pulse profile of the optical emission contains no significant structure in this region, and most x-ray observations also exhibit no statistically significant structure in this phase interval.

In the following discussion, structure in the integrated pulse profile is called permanent if it is independent of the integration time used to construct the pulse profile. In this sense the primary pulse and the interpulse are permanent pulsed structure. Observations with increased sensitivity may reveal permanent pulsed structure in the nonpulsed region of the profile, in which case the conventions described above will require redefinition. Transient structure is taken to include all features in the pulse profile whose existence depends on the particular time interval used to construct the integrated pulse profile.

At x-ray energies above 25 keV, evidence for both permanent and transient pulsed structure has been reported. Brini et al. (1971) present statistically weak evidence for two additional peaks in the pulse profile, one preceding the interpulse by 2 ms and one succeeding the interpulse by 4 ms. Helmken (1975) has combined the results of several observations and has concluded that the first feature

remains significant, and is in fact present with low statistical significance in each of the profiles used to construct the mean profile. More recently, Ryckman et al. (1977) report the existence of transient structure in two of five transits of the Crab during a balloon observation.

To provide more information on the temporal variability of the high energy x-ray emission from the Crab, the Celestial X-ray Detector was used to observe the nebula and the pulsar for eight days in 1976 and six days in 1977. A description of the observations and of details in the data analysis unique to the Crab is presented in Section 5.2. In Section 5.3 integrated pulse profiles, photon spectra, and values of pulsed flux and pulsed fraction are presented. The results from these observations are compared with previous results in Section 5.4.

5.2 OBSERVATIONS AND DATA ANALYSIS

The 1976 observation spanned the time intervals 1976 March 8.94 to March 11.09 UT and 1976 March 17.21 to March 22.96 UT. The 1977 observation spanned the time intervals 1977 March 6.97 to March 10.94 UT and March 19.00 to March 21.97 UT.

The observed counting rate from the Crab nebula is about 25% of the detector background rate, and the signal to noise

ratio is about 9 to 1 if only statistical fluctuations are taken into account. Long integration times are therefore required to detect the pulsed emission using the Celestial X-ray Detector on OSO-8. This necessitates temporal stability of the instrument to better than 1 ms or 1 part in 10^8 per day. The clock on board the OSO-8 spacecraft is stable to better than 1 part in 10^9 per day so that integration times over many days of observation are possible. The daily UTC time tag and the event timing information enables the arrival times of the detected photons to be determined to better than 0.35 ms. The x-ray pulse profile can thus be compared on an absolute time scale with radio and optical pulse arrival times determined from ground-based observations.

The results obtained from the preliminary analysis of the 1976 observations were very encouraging but raised some worrisome questions. The integrated pulse profiles exhibited the expected double-peaked structure. The primary peak was somewhat broader than expected, however, and the peak position was shifted in phase by 2 to 3 milliseconds between the first and second observation intervals. The absolute arrival time of the primary peak was shifted by eight to eleven milliseconds from the position predicted from the radio pulsar parameters (Payne 1976). A relative change of $6 10^{-4}$ in the pulsar frequency derivative corrected

the two to three millisecond phase shift between the two observing periods, but the absolute arrival time was still incorrect.

To determine the cause of the incorrect absolute phase, the timing calculations were reviewed in detail. The barycentric time-of-flight corrections were calculated using satellite-earth and earth-sun vectors (cf. Figure 2-5) obtained from the OSO production tapes. The sun - solar system barycenter vector was obtained from the Lincoln Labs PEP311 planetary ephemeris. The earth-sun vector on the OSO-8 ephemeris was obtained from the JPL Development Ephemeris Number 19 processed by the Goddard Space Flight Center program ORB 3A. The value of the light travel time per astronomical unit was 499.012 s (American Ephemeris and Nautical Almanac). Integrated pulse profiles were constructed according to UTC barycentric arrival times using pulsar parameters having an epoch of 1975 October 21.3125 obtained at Arecibo (Gullahorn et al. 1977).

Discussions with the staff of Arecibo revealed several important differences between the above technique and the one used at Arecibo to derive the pulsar parameters (Payne 1976). One difference was the use of atomic time, including the relativistic clock correction, instead of UTC. Another difference, far more significant, was the use of the PEP311

ephemeris for the time-of-flight corrections. A detailed comparison of the earth-sun vectors from the two ephemerides showed not only that the earth-sun vectors were different, but that the difference varied with time. The discrepancies in the solar time of flight are shown in Table 4. Because of these differences the barycentric timing programs were modified to agree with the method used at Arecibo, even to the point of using the same interpolation routines for the ephemeris. These modifications and the use of a more recently published set of pulsar parameters, having an epoch of 1976 March 21.875 AT (Gullahorn et al 1977), eliminated the two to three millisecond phase shift between observation intervals. The primary peak was also somewhat narrower, being completely contained in a four millisecond wide phase interval. The absolute phase of the x-ray emission, however, still differed from the predicted radio values by three to four milliseconds.

TABLE 4

Comparison of JPL 19 and PEP311 Solar Vectors

Date	Earth-Sun Time-of-Flight Correction t(JPL) - t(PEP) (s)
1976 March 7 0h	0.015
1976 March 11 0h	0.018
1976 March 15 0h	0.020
1976 March 19 0h	0.019
1976 March 23 0h	0.023

The constant offset of the absolute phase from the predicted value strongly suggested that some simple additive constant was incorrect. After the conversion between various time scales was checked, the telemetry format was examined to verify the location of the UTC time tag. It was found that the time tag, which had been assumed to refer to the beginning of the minor frame, in fact referred to the end of the third sync word in the minor frame. The end of the third sync word occurs 3.75 milliseconds after the start of the minor frame. The application of this correction brought the absolute phase of the x-ray pulsations into agreement with the predicted radio phase to within the timing resolution of the instrument and the uncertainty on the pulsar parameters.

The excellent agreement of the x-ray results with the frequency and absolute phase based on the radio observations is a good test of the correct performance of the timing analysis. It was hoped that subsequent observations would entail no further timing difficulties. Unfortunately, this was not the case. In the absence of Arecibo observations of the Crab in 1977, preliminary values for pulsar parameters with an epoch of 1977 February 8.04457 UT were obtained from the Five College Radio Observatory (Helfand 1977). When the data were binned according to these new parameters no evidence for pulsed emission was found. When the data were

rebinned using updated parameters from Arecibo values having an epoch of 1975 October 21.3125 AT, pulsed emission was observed, although the phase of the primary peak drifted from day to day.

Because Arecibo is no longer monitoring the Crab routinely, current pulsar parameters from Arecibo are not available. A calculation of the number of predicted pulse periods which occurred during a 15-day interval near the time of observation revealed a discrepancy of 15 periods between the Five College parameters and the Arecibo parameters. Since the PEP311 ephemeris was used in the calculation of both sets of pulsar parameters, the reason for this discrepancy is not clear. It presumably has to do with details in the pulse timing calculations. The Arecibo parameters and were adjusted slightly to remove the drift in the daily phase of the primary peak and to position the center of the primary peak at a phase value of 0.0, and were updated to an epoch of 1977 March 1.00 AT. The adjustment in parameter values, while slight, was much larger than would be expected on the basis of the formal uncertainties of the original parameters. The pulsar parameters used for the 1976 and 1977 observations are listed in Table 5.

TABLE 5

Pulsar Parameters For The Crab Observations

Parameter	1976	1977
ϕ_o	0.4375	0.087
ν_o	30.13041094174275	30.11902077839999
$\dot{\nu}_o$	$-3.8326129039 \times 10^{-10}$	$-3.8291458235 \times 10^{-10}$
$\ddot{\nu}_o$	8.718×10^{-19}	1.1837×10^{-20}
Epoch	1976 March 21.875 AT	1977 March 1 00.00 AT

5.3 OBSERVATIONAL RESULTS

Among the most important results from the Crab observations are those concerning the day-to-day variations in pulsed emission. Three different indicators of pulsed emission were examined; the shape of the integrated pulse profiles, the value of the pulsed flux, and the value of the pulsed fraction. The values of pulsed flux and pulsed fraction are not independent, however, they are subject to different systematic errors. Examination of both quantities, therefore, provides information on the magnitude of some such systematic errors. In order to reduce the effects of statistical fluctuations, a large energy interval (16 - 114 keV) was used in the search for day-to-day variations in the flux levels. The data were integrated over time intervals of approximately 24 hours duration. These time intervals are identified with a day number in Table 6. In the following

discussion all references to specific observation intervals are by day number.

TABLE 6

Data Analysis Intervals

Day Number	Time Interval (UT)	Livetime within 3° of Source(s)
1	1976 March 8:2250 - 9:2220	1523
2	9:2220 - 11:0213	1550
3	17:0500 - 17:2330	1628
4	17:2340 - 18:2150	2046
5	18:2355 - 19:2306	1987
6	20:0108 - 20:2319	1325
7	20:2320 - 21:2254	1962
8	21:2255 - 22:2306	1786
9	1977 March 6:2317 - 7:2255	1086
10	7:2255 - 8:2305	1702
11	8:2330 - 10:2230	2412
12	18:2330 - 19:2330	1074
13	19:2330 - 20:2307	1198
14	20:2309 - 21:2316	876

The first step taken in the search for variaton in pulsed emission was the examination of the integrated pulse profiles for changes in pulse shape or phase of pulsed emission. The integrated pulse profiles obtained each day are presented in Figures 5-2 through 5-6. Mean pulse profiles for the 1976, 1977, and the combined observations are shown in Figure 5-7. In order to test the hypothesis of constant pulse shape, the data in each of the 33 phase bins

C-2

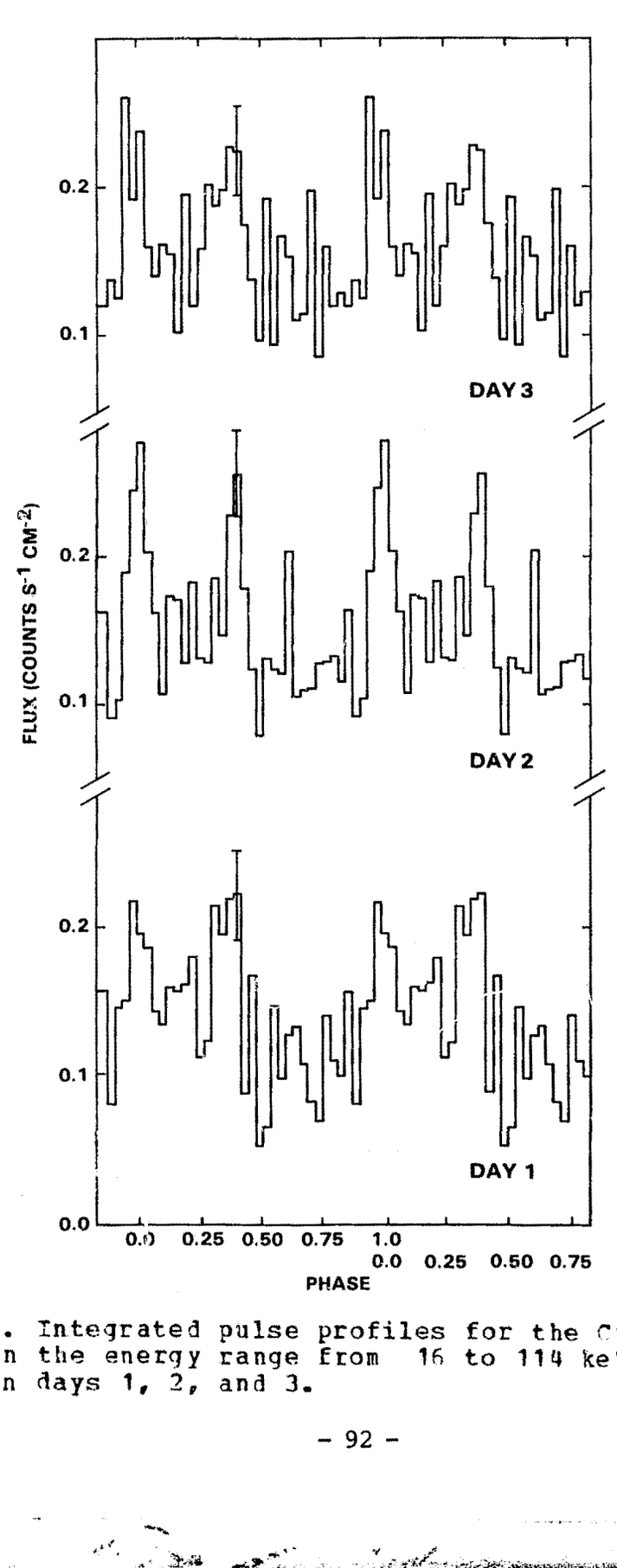

Figure 5-2. Integrated pulse profiles for the Crab pulsar in the energy range from 16 to 114 keV obtained on days 1, 2, and 3.

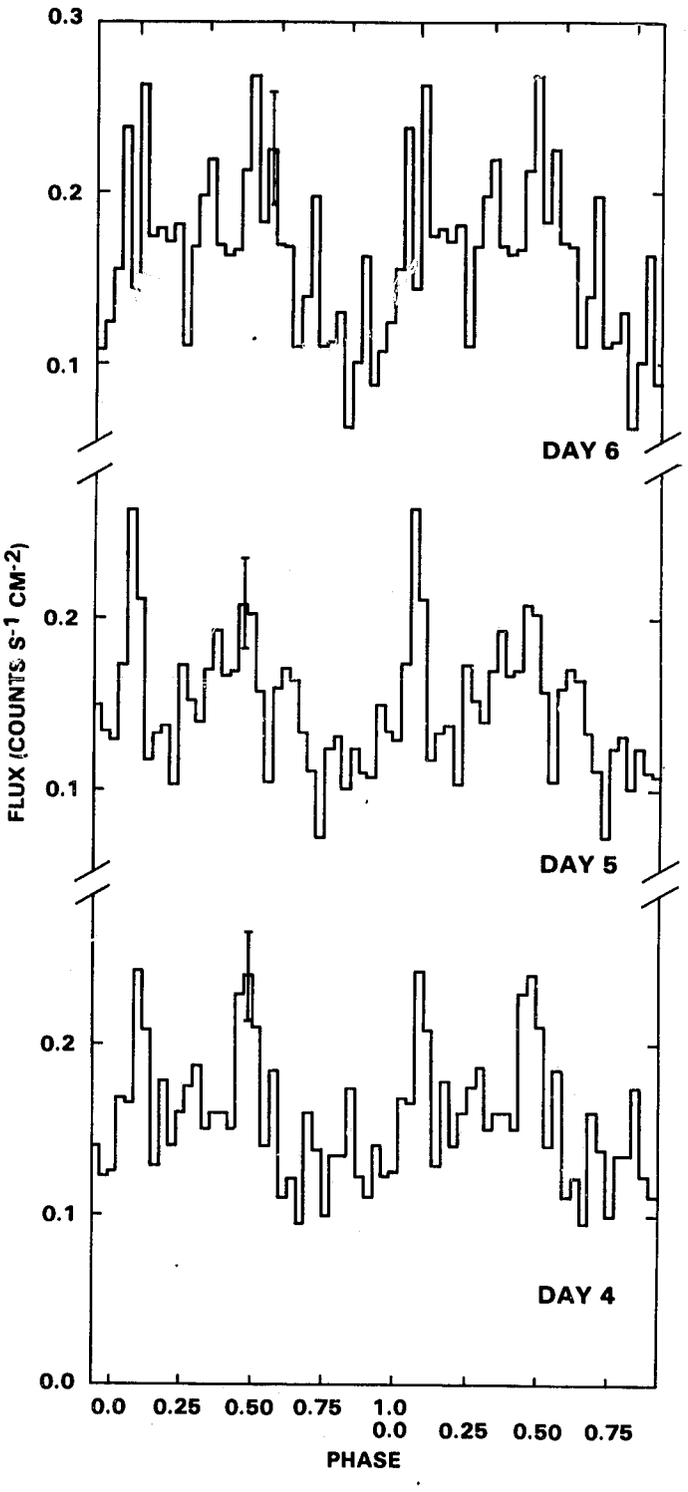

Figure 5-3. Integrated pulse profiles for the Crab pulsar in the energy range from 16 to 114 keV obtained on days 4, 5, and 6.

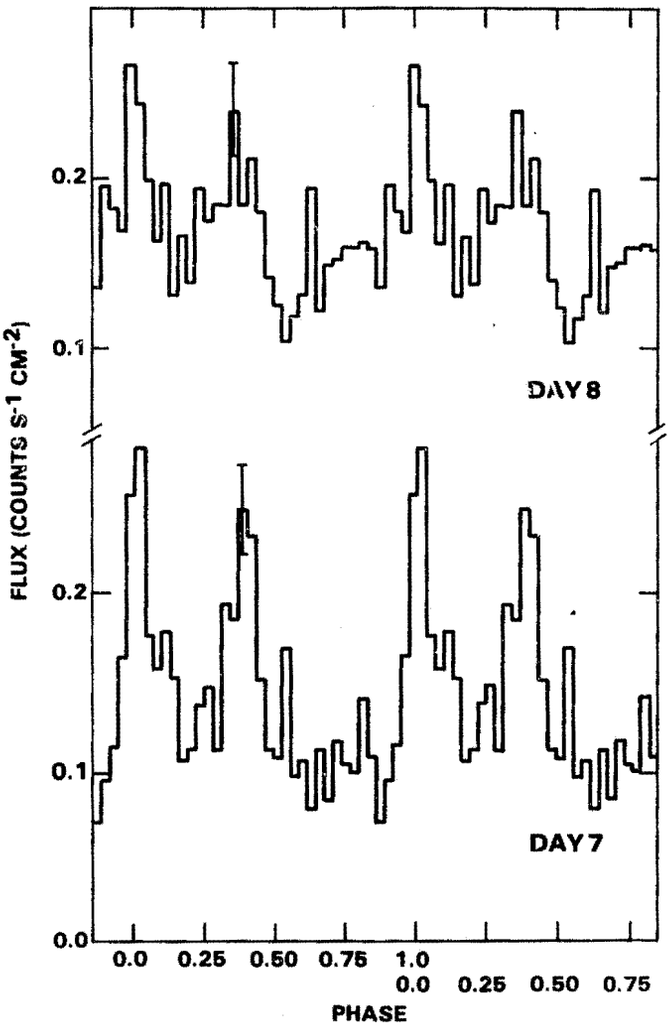

Figure 5-4. Integrated pulse profiles for the Crab pulsar in the energy range from 16 to 114 keV obtained on days 7 and 8.

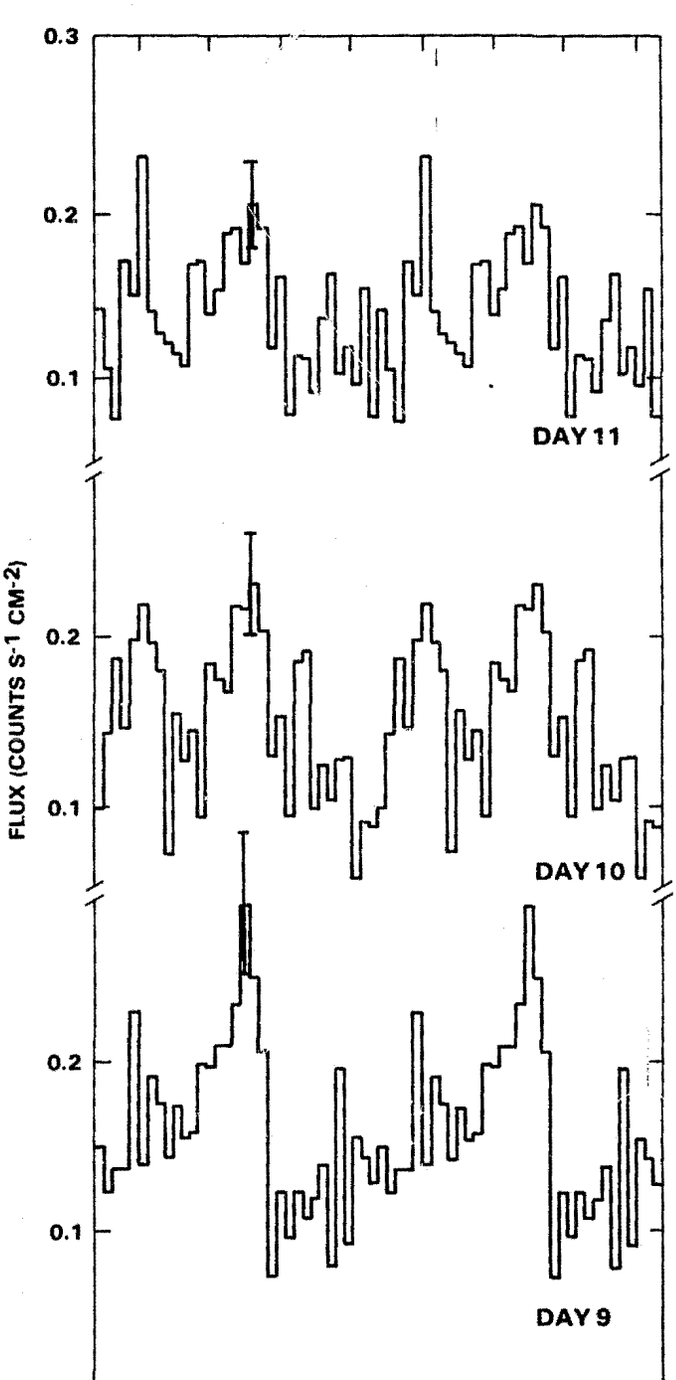

Figure 5-5. Integrated pulse profiles for the Crab pulsar in the energy range from 16 to 114 keV obtained on days 9, 10, and 11.

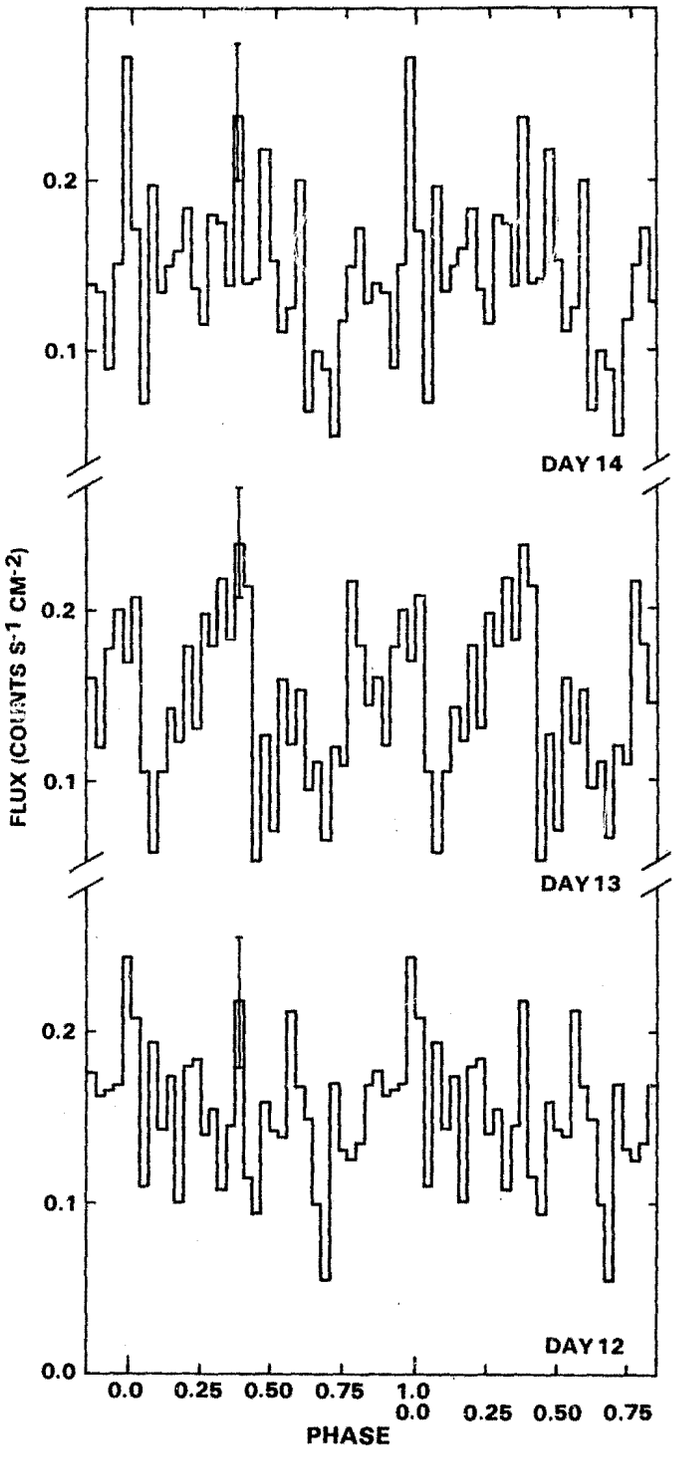

Figure 5-6. Integrated pulse profiles for the Crab pulsar in the energy range from 16 to 114 keV obtained on days 12, 13, and 14.

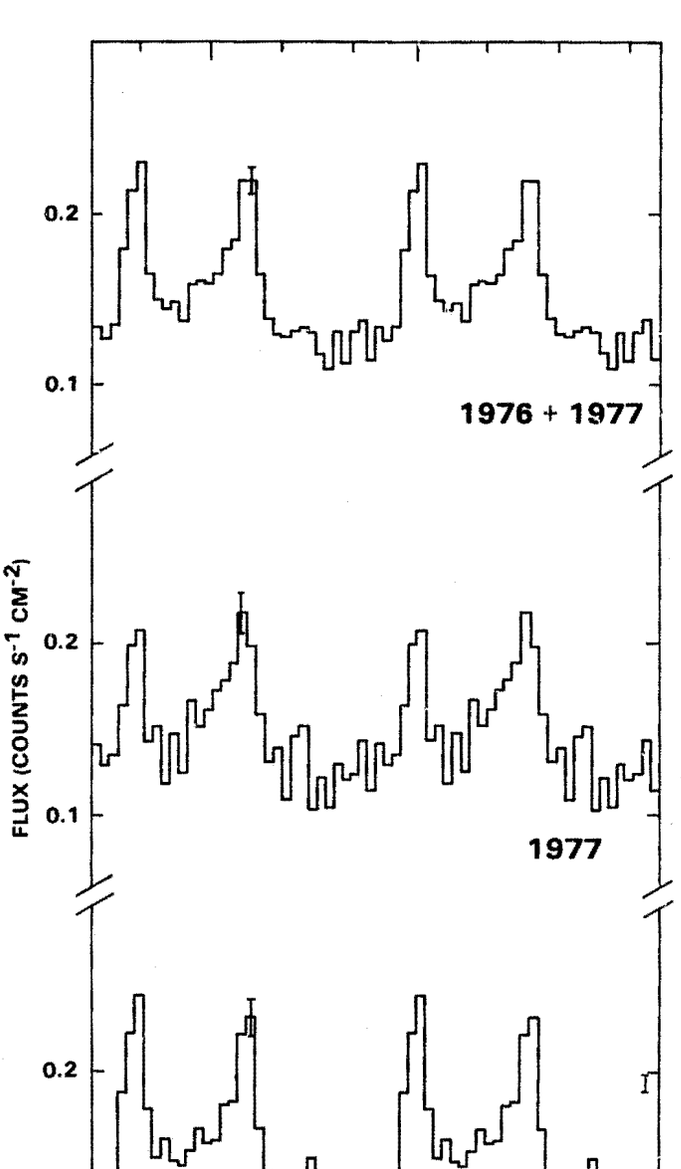

Figure 5-7. Mean integrated pulse profiles from the Crab pulsar in the energy range from 16 to 114 keV. The results from the 1976, 1977, and combined observations are shown separately.

were examined for large excursions of the daily flux from the mean flux in that phase bin. This analysis was performed for the 1976 and 1977 observations separately. The value of chi-squared obtained from this comparison was calculated for each phase bin; improbably large values of chi-squared were taken to be those values for which the probability of exceeding chi-squared was less than 0.05. The contributions to chi-squared for each day and each phase bin were examined to determine which, if any, of the daily pulse profiles were consistently contributing to the large values of chi-squared.

During the 1976 observation, four phase bins exhibited improbably large values of chi-squared. For purposes of this discussion, the phase bins are numbered sequentially starting at phase = 0.0, so that the bins with large chi-squared are identified as bins 16, 17, 20, and 33. The observed values of chi-squared were 18.9, 16.3, 21.0, and 20.7, respectively, for 7 degrees of freedom. Days 1 and 4 were the primary contributors to bin 16; Days 1 and 3, to bin 17; Days 1, 2, 7, and 8, to bin 20; and Days 4, 5, and 6, to bin 33. Thus, no one day was a primary contributor to all of the large deviations. Day 1 did contribute to three of the four bins in question.

The 1977 integrated pulse profile also exhibited four phase bins, bins 3, 4, 16, and 27, having improbably large values of chi-squared. The values of chi-squared were, respectively, 13.6, 16.2, 20.5, and 16.6 for 6 degrees of freedom (for the purposes of this calculation, Day 11 was divided into 2 smaller intervals). Day 13 contributed overwhelmingly to the large values of chi-squared in the last three bins with values of 8.3, 10.4, and 8.1. The flux values were anomalously low in bins 4 and 16 and anomalously high in bin 27. There is no simple explanation for the low flux values; because the data are binned modulo the pulsar period, a systematic error would have to exclude counts only at specific values of pulse phase, and this is very unlikely. The high value of flux in bin 27 may indicate transient structure which occurred on this day only. This possibility is discussed further in Section 5.4.

The statistical analysis presented above does not check for the simultaneous increase in two or more adjacent phase bins. To remedy this situation the pulsed flux in the primary pulse and interpulse were calculated separately and are shown in Table 7. The primary pulse was assumed to be 5 phase bins wide (out of 33); the interpulse was assumed to be 10 phase bins wide; this width includes the long leading edge of the interpulse. By this measure of variability, both the primary pulse and interpulse were consistent with

constant pulsed emission during the 1976 observation. Once again, the 1977 observations indicate statistically significant departures from random fluctuations in the pulsed emission. The primary pulse is significantly low during Day 13 and the interpulse has essentially disappeared during Day 12.

TABLE 7

Pulsed Flux in Primary Pulse and Interpulse

Day Number	Flux (counts s^{-1} cm^{-2}) Primary Flux	Interpulse Flux
1	0.36±0.08	0.61±0.1
2	0.47±0.08	0.46±0.1
3	0.32±0.07	0.48±0.1
4	0.25±0.07	0.49±0.1
5	0.26±0.07	0.38±0.1
6	0.35±0.08	0.68±0.1
7	0.52±0.07	0.58±0.1
8	0.28±0.07	0.33±0.1
9	0.24±0.09	0.75±0.1
10	0.32±0.07	0.50±0.1
11	0.23±0.06	0.51±0.1
12	0.20±0.09	0.03±0.1
13	0.07±0.08	0.38±0.1
14	0.26±0.10	0.45±0.2
MEAN	0.30±0.02	0.48±0.03

When the data from both the 1976 and the 1977 observations are combined, there is no evidence for additional permanent pulsed structure at a statistically significant level.

The mean integrated pulse profiles presented in Figure 5-7 show that the pulsed emission occurs in no more than 18 contiguous phase bins; there is no indication of significant structure in the remaining 15 bins. The pulsed flux, nonpulsed flux, total flux, and pulsed fraction were calculated for each day; the results are shown in Figure 5-8 and in Table 8. To determine how sensitive the resulting values are to the chosen pulsed emission region, the calculations were also performed for the 1976 data using 21 bins for the pulsed emission region. There is generally good agreement between the two sets of values.

The observed fluctuations in the nonpulsed emission indicate either real variations in the nonpulsed emission or a large systematic error. As discussed in Chapter 2, incorrect background subtraction is a likely candidate for such an error. The background rate in the energy range from 16 to 114 keV is shown in Figure 5-9. The background rate varies more than was expected; this variation is most likely due to differing times spent in the radiation belts each day. There is no clear-cut correlation between the background rate and the nonpulsed emission. For example, the nonpulsed emission is essentially constant on days 5 and 6 while the background rate exhibits a significant increase during the same time interval. The value of the correlation coefficient is -0.23; this value is consistent with the hypothesis of no correlation.

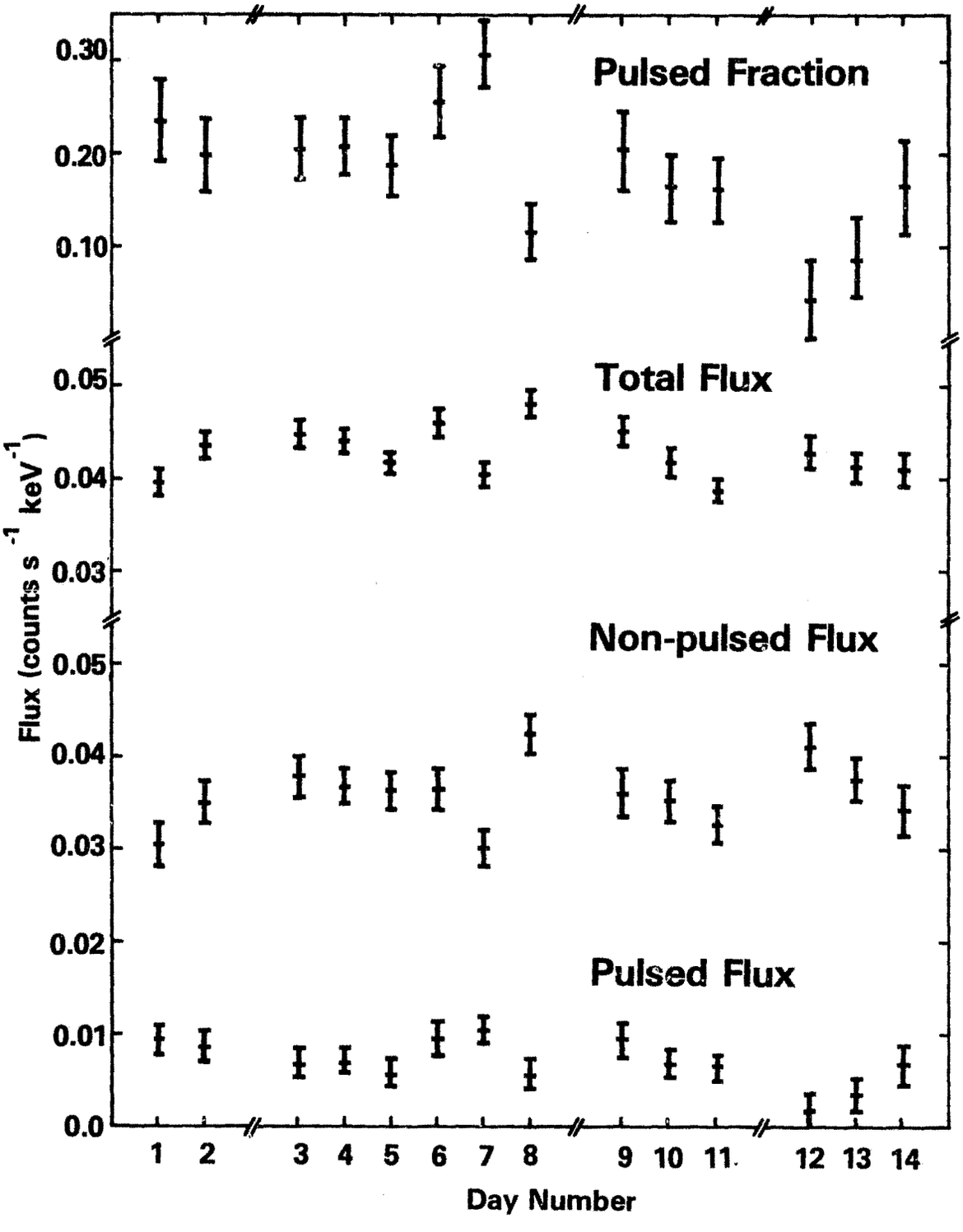

Figure 5-8. The pulsed flux, nonpulsed flux, total flux, and pulsed fraction in the energy range from 16 to 114 keV as a function of day number.

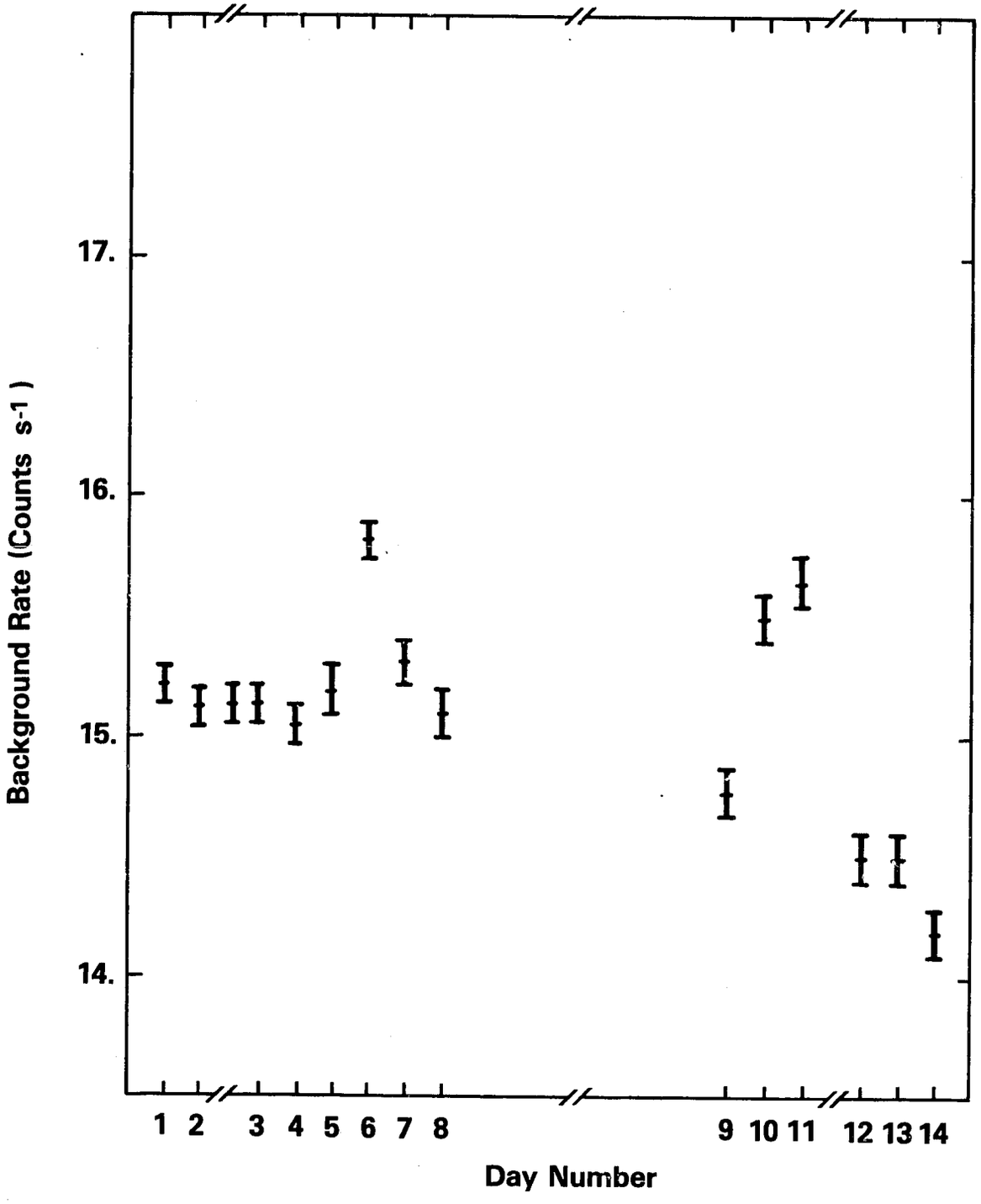

Figure 5-9. The observed background rate in the energy range from 16 to 114 keV as a function of day number.

TABLE 8

Open Central Crystal Results

Flux (counts s^{-1} keV^{-1})

Day	Pulsed (10^{-3})	Nonpulsed (10^{-2})	Total (10^{-2})	Pulsed Fraction (%)
1	4.3±1.6	3.03±0.22	3.96±0.15	23±4
2	8.6±1.6	3.50±0.22	4.35±0.15	20±4
3	6.9±1.6	3.79±0.21	4.48±0.14	15±4
4	7.0±1.4	3.69±0.18	4.39±0.12	16±3
5	5.7±1.4	3.62±0.19	4418±0.13	14±3
6	9.5±1.7	3.64±0.23	4.59±0.16	21±4
7	10.4±1.4	3.01±0.19	4.06±0.13	26±4
8	5.6±1.5	4.24±0.20	4.80±0.14	12±3
9	9.2±2.0	3.60±0.26	4.51±0.17	20±4
10	6.8±1.5	3.50±0.21	4.18±0.14	16±4
11	6.3±1.3	3.26±0.18	3.88±0.12	16±3
12	1.7±1.8	4.10±0.25	4.28±0.17	4±4
13	3.6±1.7	3.75±0.23	4.11±0.16	9±4
14	6.7±2.1	3.42±0.28	4.09±0.19	16±5
1976	7.8±0.5	3.56±0.07	4.34±0.05	16±1
1977	6.4±0.7	3.90±0.10	4.53±0.06	14±2
MEAN	7.2±0.4	3.68±0.06	4.41±0.04	16±1

The values shown in Figure 5-8 for the nonpulsed flux obtained during the 1976 observation are not consistent with constant flux. The value of chi-squared is 28 for 7 degrees of freedom. The probability that the observed scatter is due to statistical fluctuations about a constant value is less than 1.5×10^{-4}. The value of chi-squared for the pulsed flux is 9 for 7 degrees of freedom. This value is consistent with constant pulsed emission. The variations in total flux and pulsed fraction are consistent with the observed values for the pulsed and nonpulsed flux.

There are two known systematic errors which could contribute to an incorrect estimate of the background. The first of these is a systematic change in photomultiplier gain as a function of the distance from source. This gain change, which is described in Section 6.2, can be as large as 1%. It can produce spurious results in observed spectra, especially for weaker sources. To estimate the maximum effects of such a gain change, the background rate in the energy range from 16 to 114 keV was corrected for an assumed 1.4% change in the position of the lower energy channel edge. The resulting change in background rate was 0.15 counts s^{-1}, which is 20% of the observed variation in the background rate.

The other systematic effect involves a simultaneous change in the backgroound rate and the position of the spin axis. During the beginning of each observation the spacecraft orientation is changed in order to bring the source into the field of view. During this time source counts will be collected even though the detector is not in the optimum orientation. It sometimes takes on the order of a day to optimize the detector orientation. If the background rate changes significantly between the time the source first enters the field of view and the time at which the spin axis is 5° away from the source, then the calculated source flux may be incorrect. A change by a

factor of 2 in the background rate between optimum and non-optimum detector orientation is sufficient to cause a $\sim$10% error in the source strength. A change of this magnitude is sufficient to account for the observed variation. The same effect is expected to occur at the end of each observation, as the source leaves the detector field of view.

If the first and last days of the 1976 observation are excluded for this reason, the value of χ^2 for the nonpulsed emission during the remainder of the observation is 10.2 for 5 degrees of freedom. This value is consistent with constant emission at the 95% confidence level.

The 1977 observations also showed large fluctuations in the emission from day to day. In this case the value of chi-squared for the nonpulsed emission is 10.5 for 5 degrees of freedom and is consistent with constant emission at the 95% confidence level. The value of chi-squared for the pulsed emission is 14.2; the probability of exceeding this value of chi-squared is less than 1.5×10^{-2}. The pulsed flux values obtained during Days 12 and 13 evidently lowered the 1977 mean compared the the 1976 mean.

For the sake of completeness, the correlation coefficient for the background rate and the nonpulsed emission was

calculated for the 1977 observation. The resulting value, -0.48, is consistent with no correlation.

Statistical limitations prevent the determination of precise pulsed spectra on a daily basis. In this work, spectra were obtained for the 1976 data, the 1977 data, and the combined data. The spectral fits covered the energy range from 21 to 220 keV. Dolan et al. (1977) have presented the time-averaged spectrum for the 1976 observations alone from 16 to 500 keV. The more restricted energy range was used in this work because the pulsar was detected at energies up to 220 keV only. Best fit spectral parameters for the pulsed, nonpulsed, and total emission are presented in Table 9. The observed spectra are plotted in Figures 5-10 through 5-18. The uncertainties are derived from the 68% confidence contours as described by Lampton et al. (1976). The normalization energy, E_o, was chosen so as to circularize the confidence contours, thereby making the fitting parameters statistically independent.

Another measure of the pulsar spectrum is provided by the variation of pulsed fraction as a function of energy. Pulsed fraction values are shown in Figure 5-19. Also shown is the fit obtained by Thomas and Fenton (1975) to previous measurements of pulsed x-ray emission.

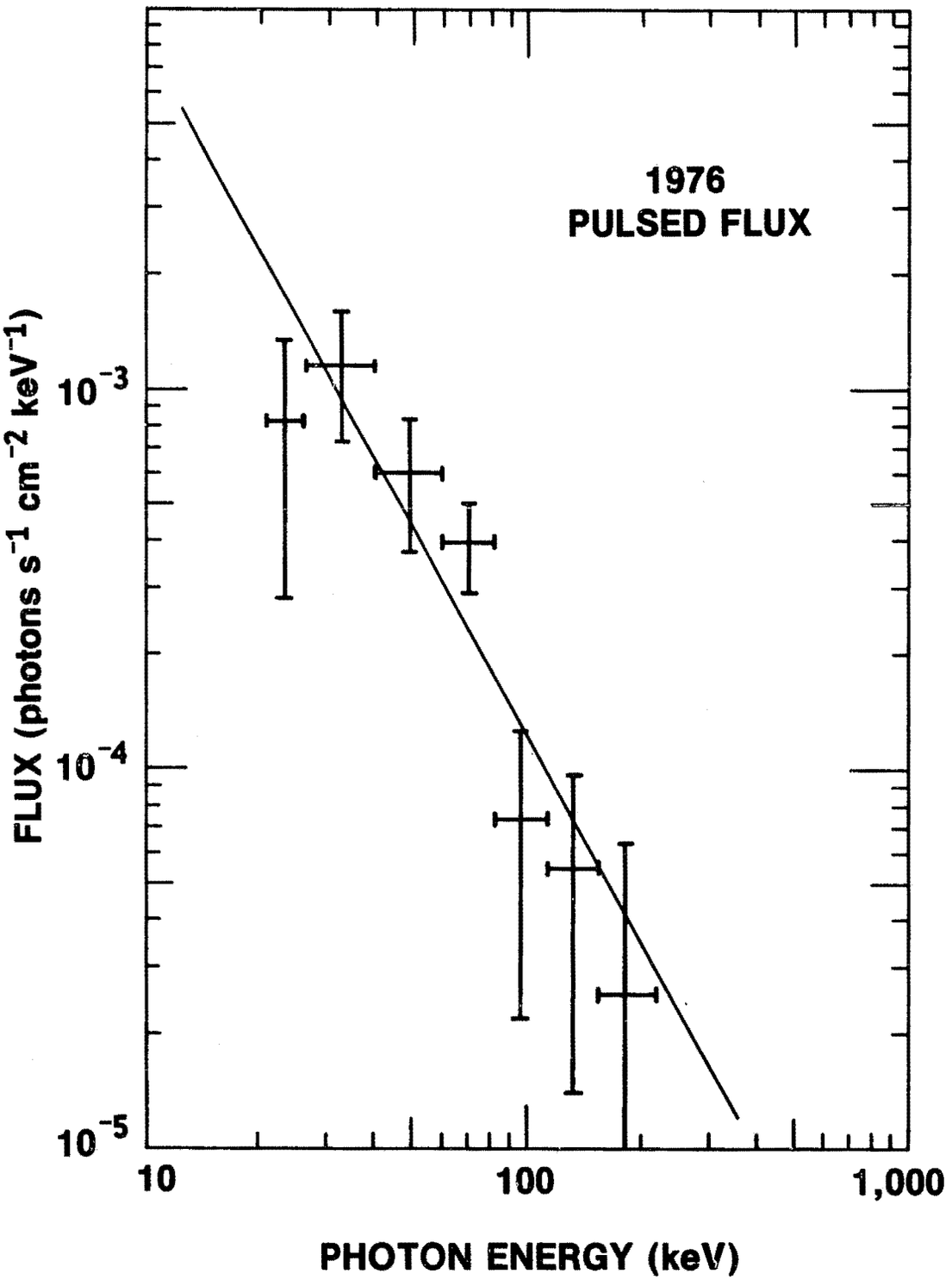

Figure 5-10. The 1976 Crab pulsed spectrum.

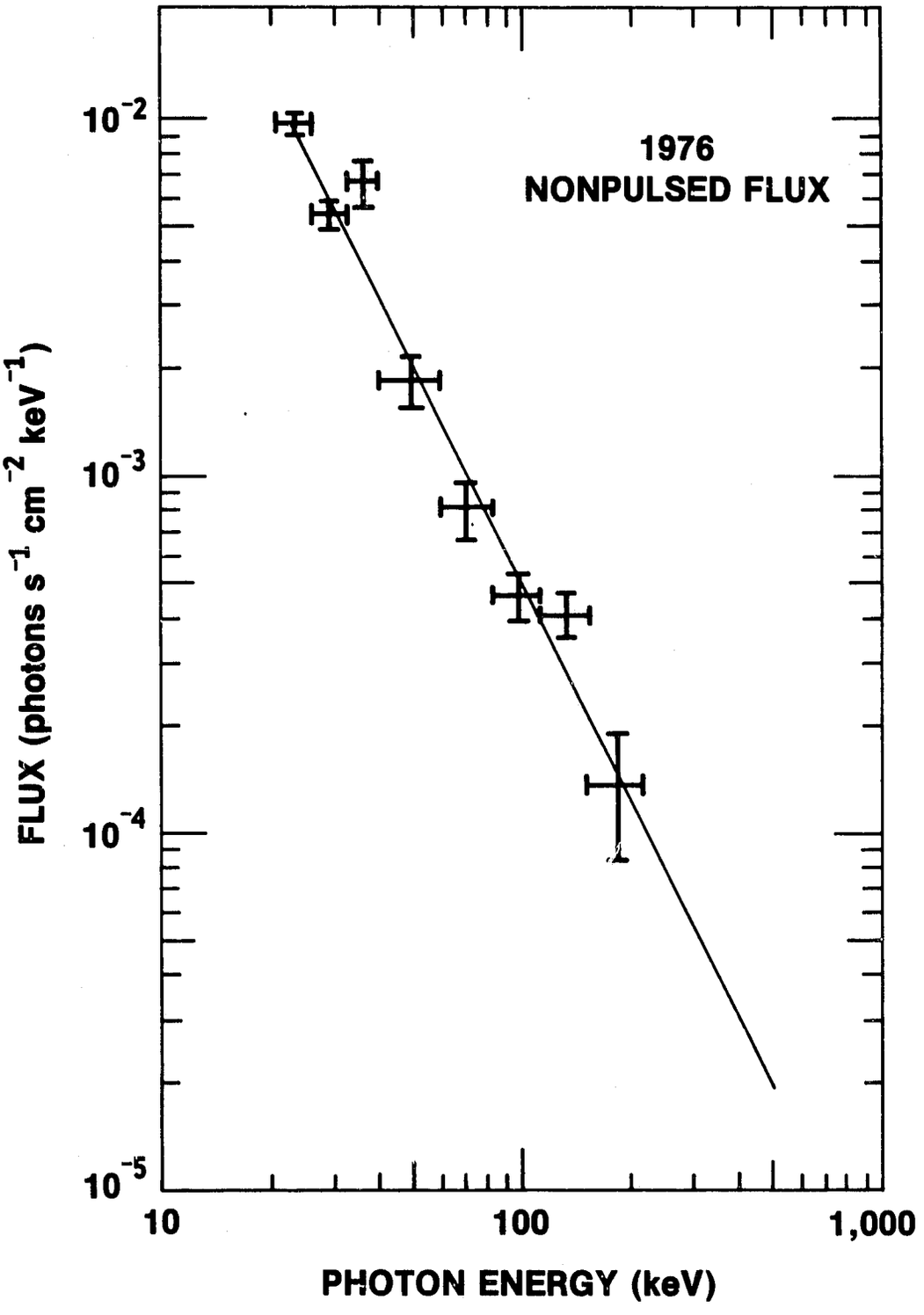

Figure 5-11. The 1976 Crab nonpulsed spectrum.

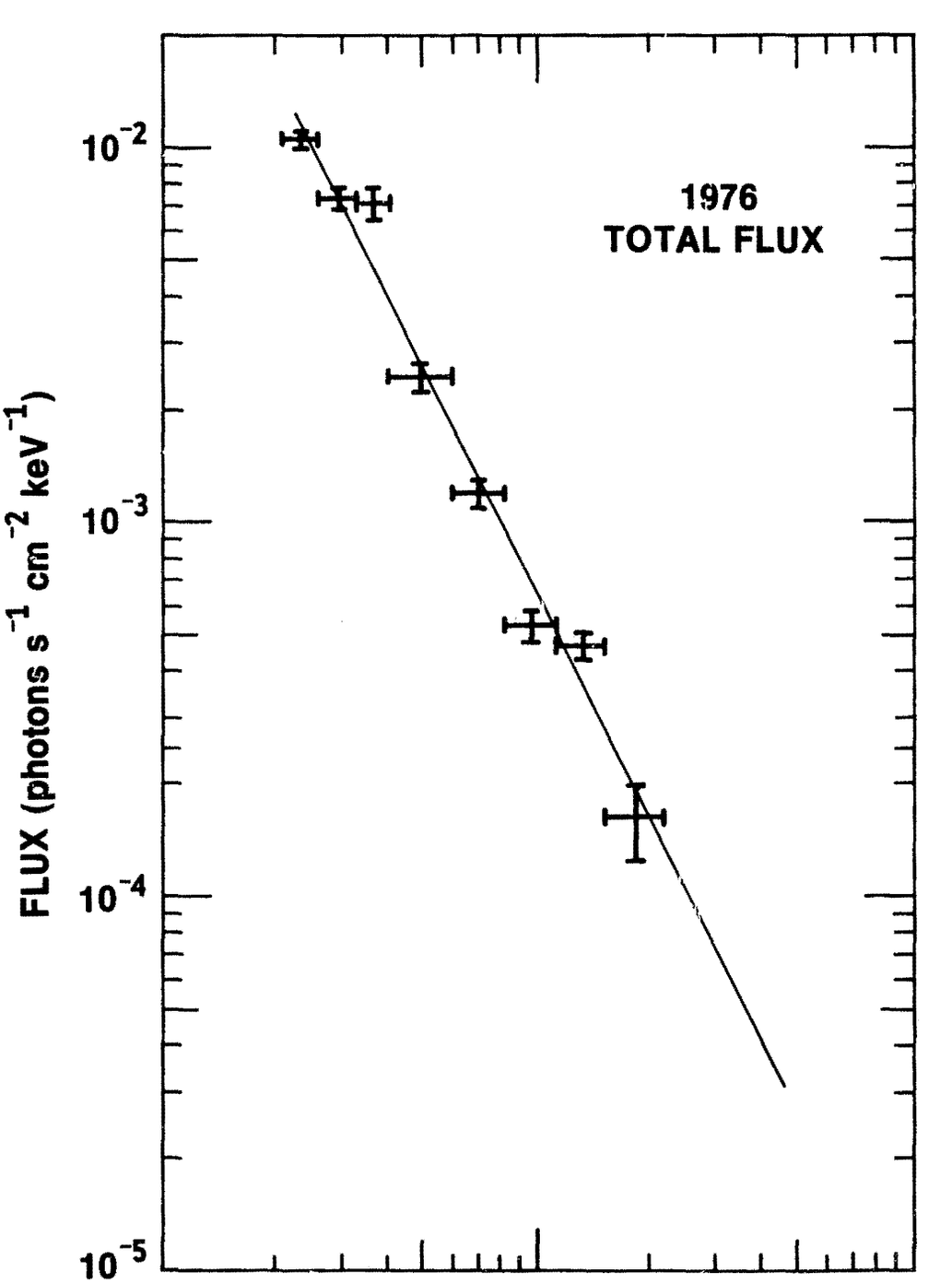

Figure 5-12. The 1976 Crab total spectrum.

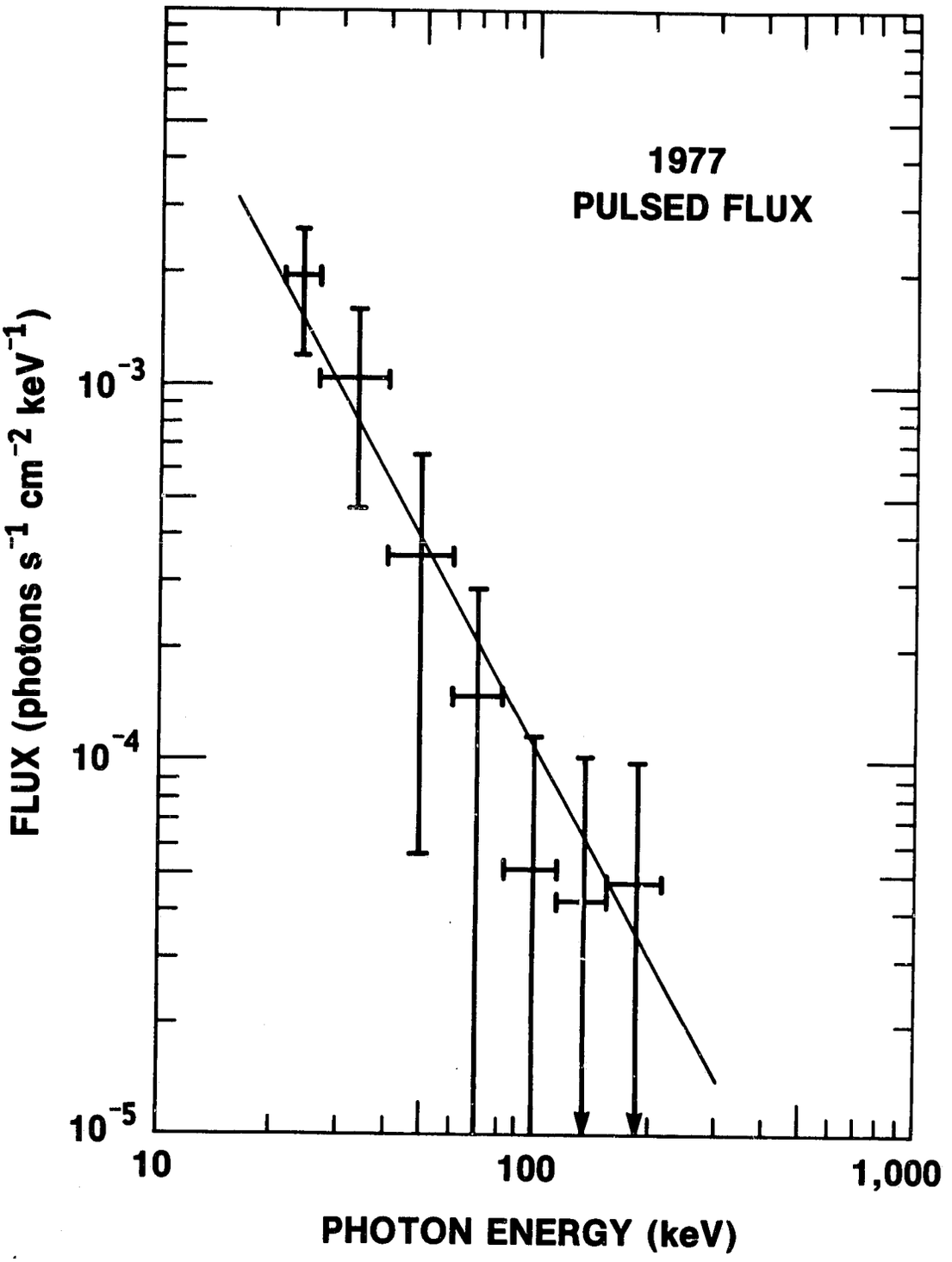

Figure 5-13. The 1977 Crab pulsed spectrum.

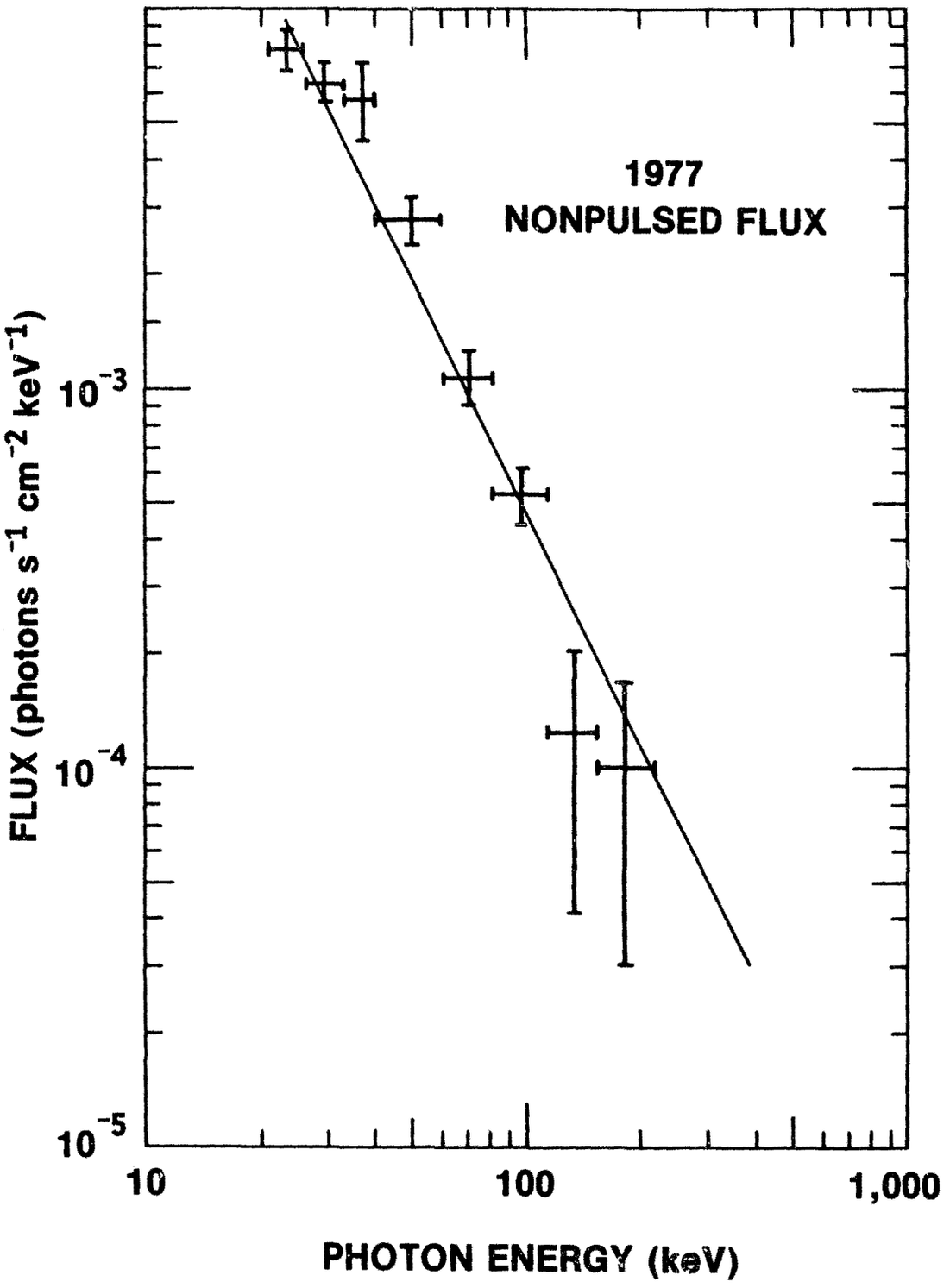

Figure 5-14. The 1977 Crab nonpulsed spectrum.

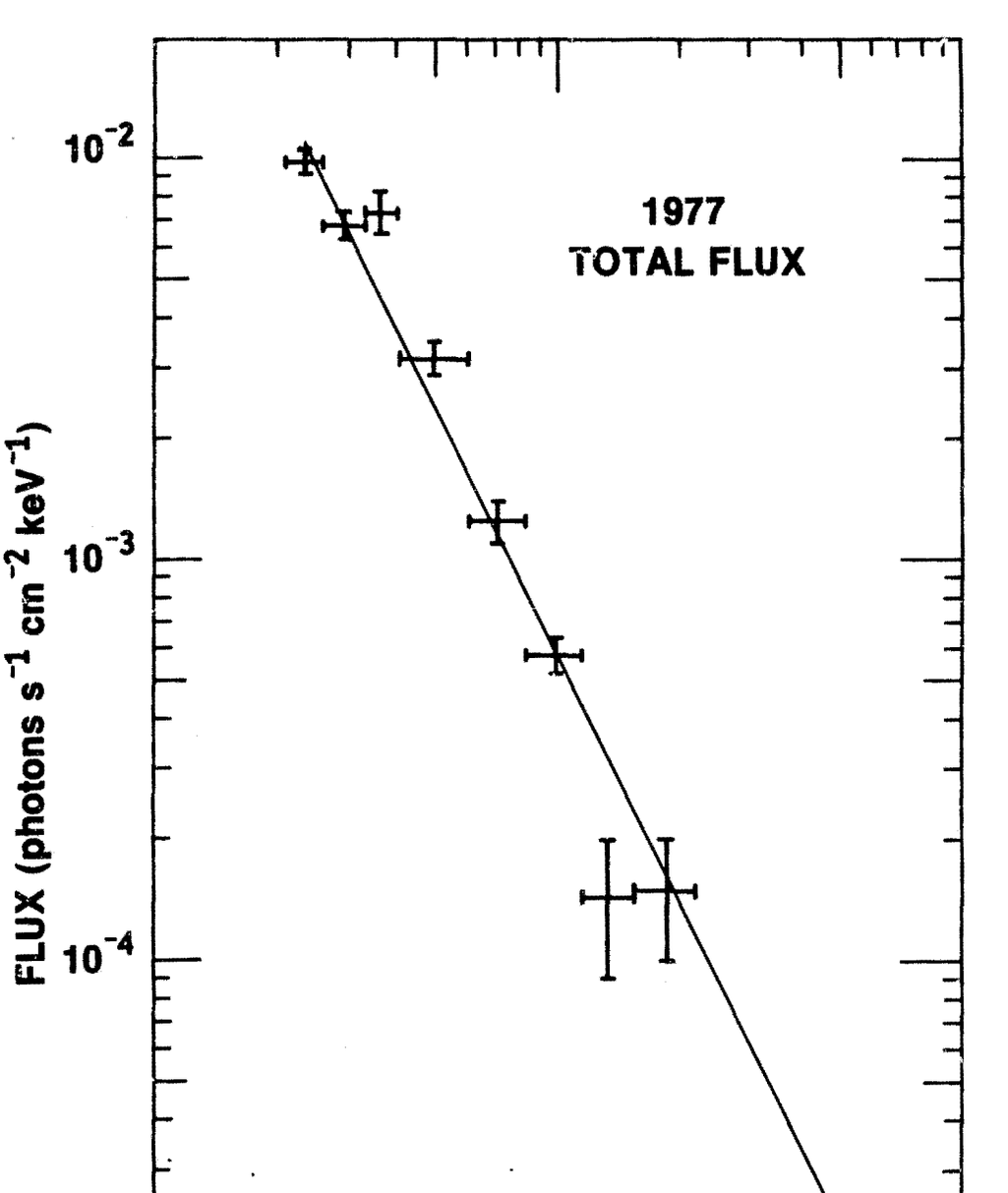

Figure 5-15. The 1977 Crab total spectrum.

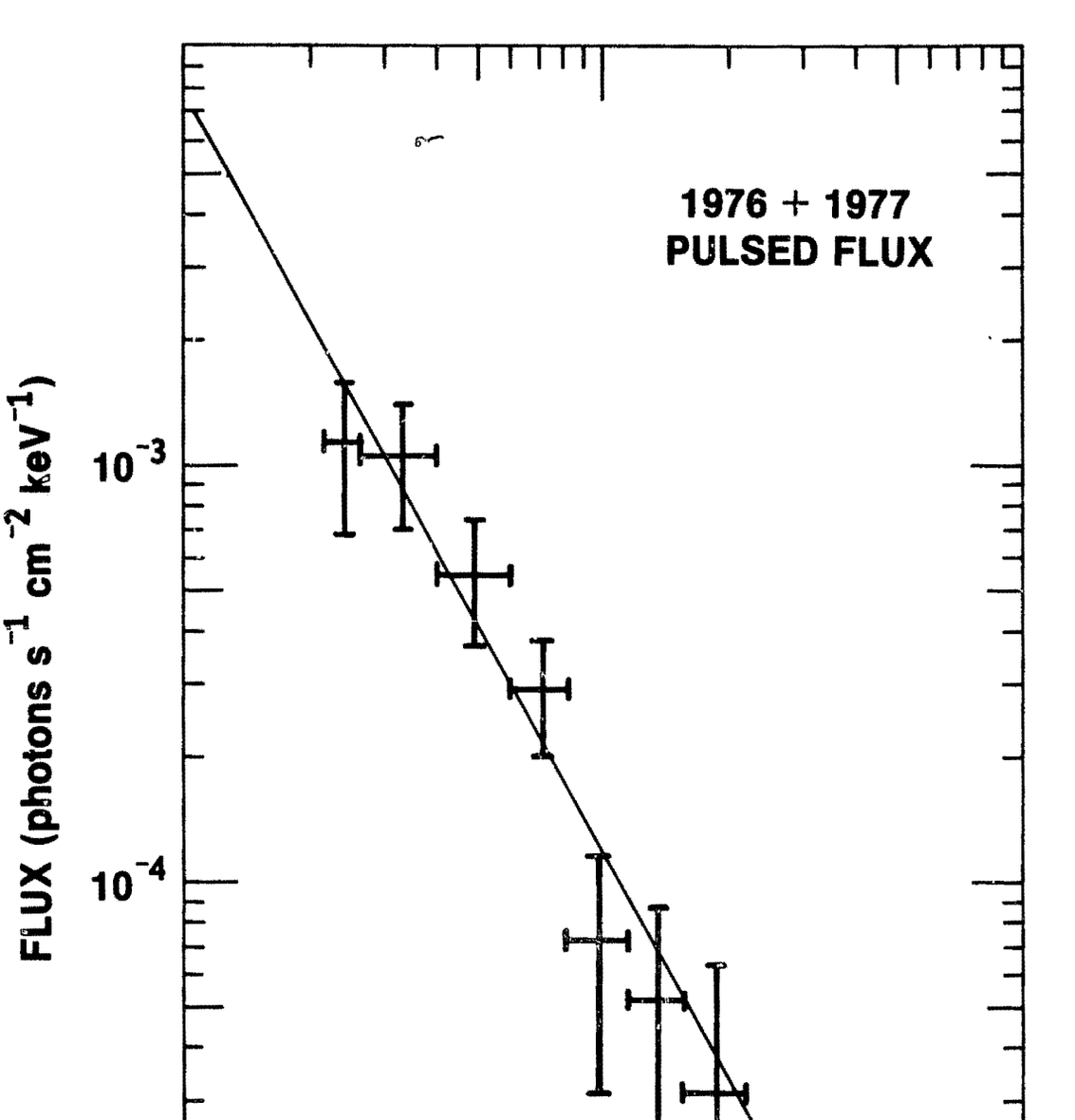

Figure 5-16. The 1976+1977 Crab pulsed spectrum.

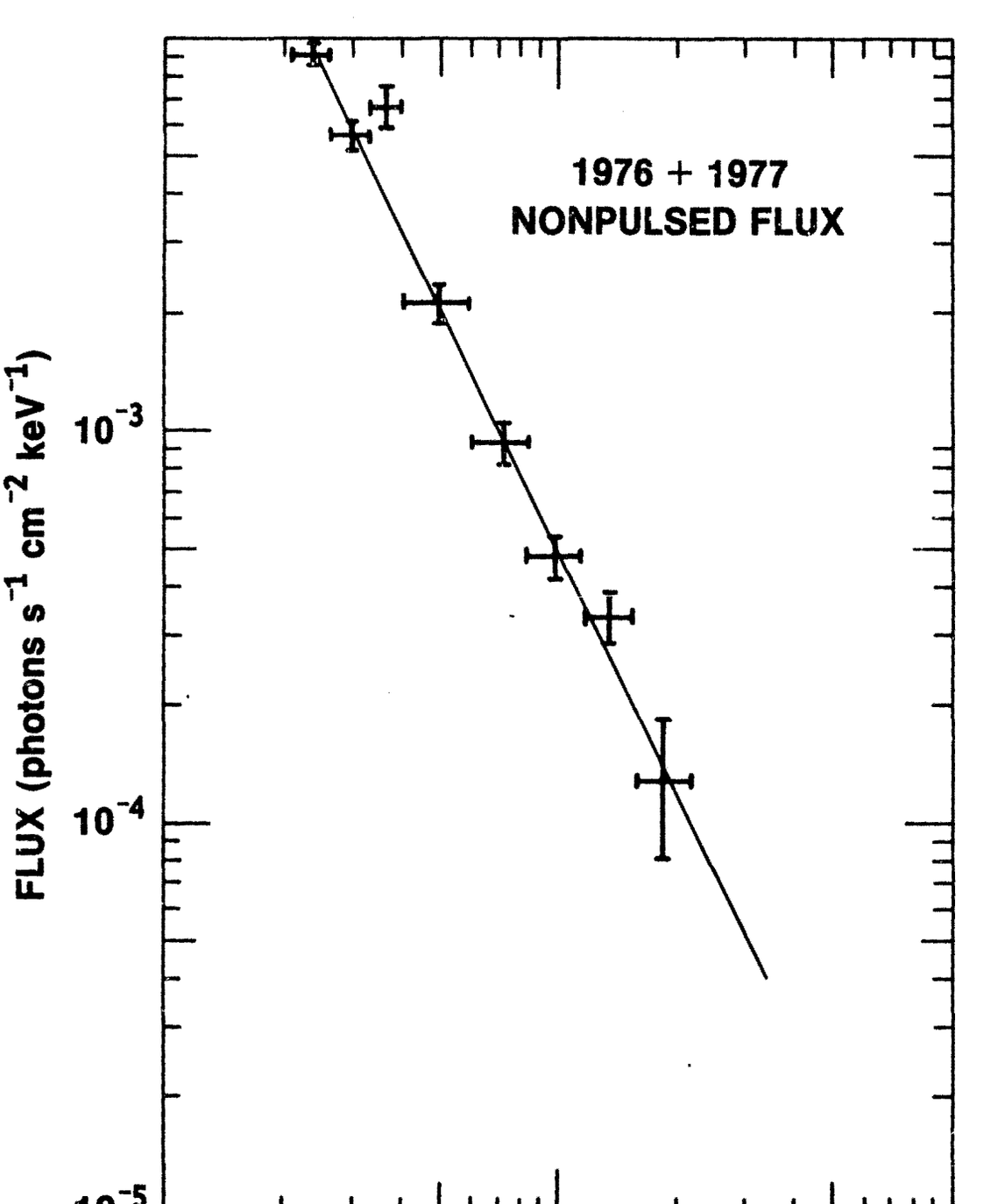

Figure 5-17. The 1976+1977 Crab nonpulsed spectrum.

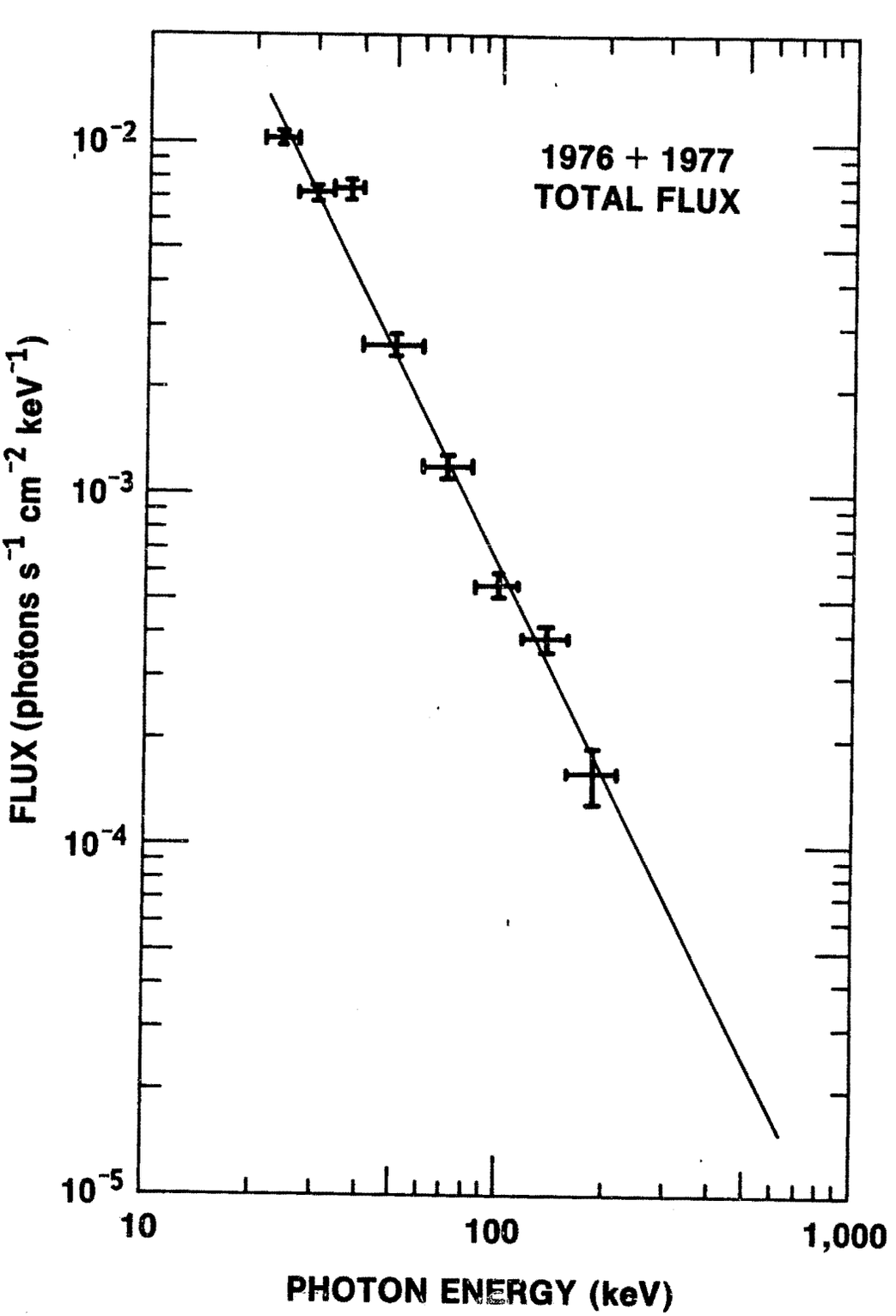

Figure 5-18. The 1976+1977 Crab total spectrum.

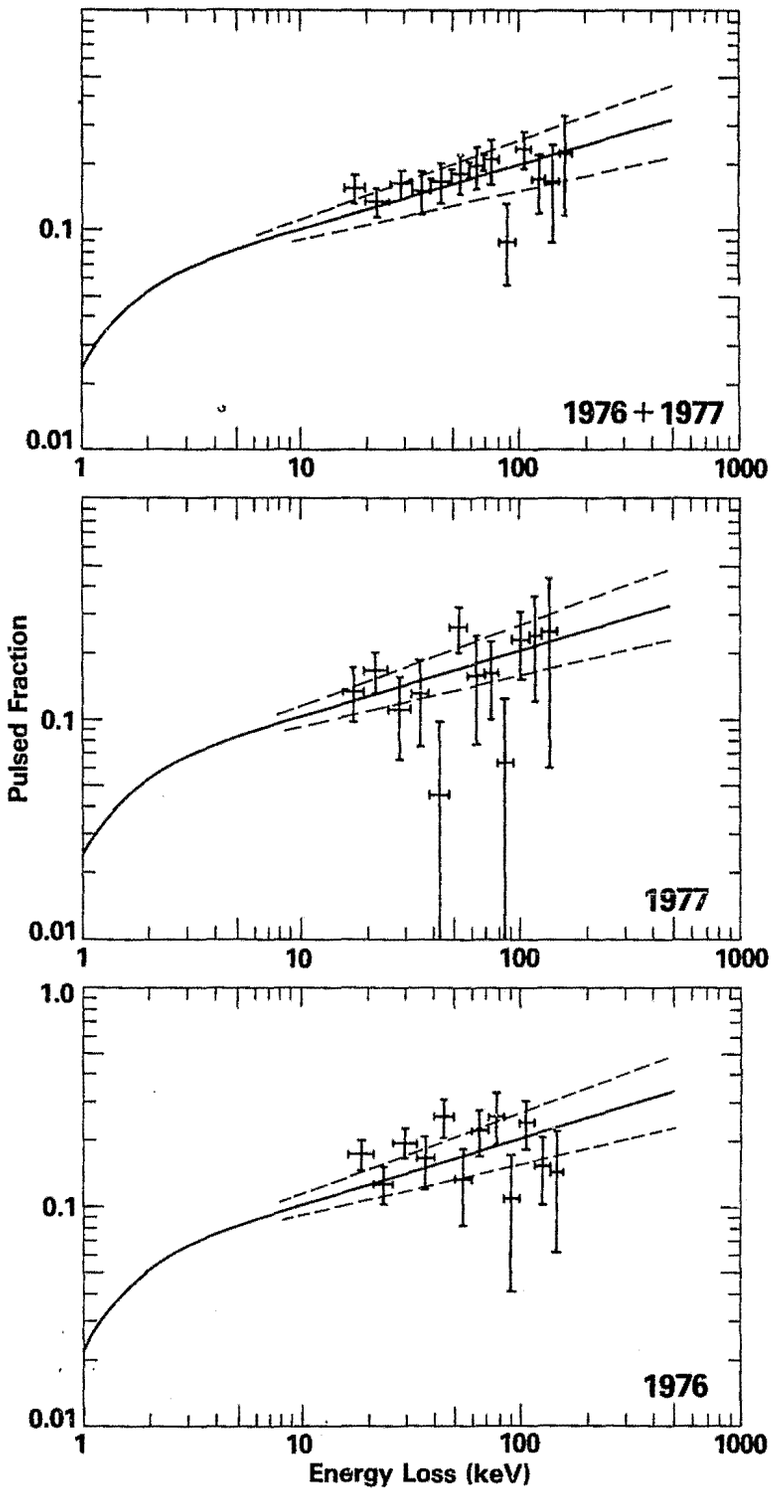

Figure 5-19. The pulsed fraction of emission as a function of energy loss in the central crystal for the 1976, 1977, and combined observations. The solid line and the dotted lines are the best- function and uncertainties, respectively, obtained by Thomas and Fenton (1975) for a number of previous observations of the Crab pulsar.

TABLE 9

Crab Spectral Parameters

$dN/dE = A(E/E_o)^{-\alpha}$ photons s^{-1} cm^{-2} keV^{-1}

1976	A	α
Pulsed	$6.2 \pm 2.4 \times 10^{-4}$	1.8 ± 0.3
Nonpulsed	$3.25 \pm 0.33 \times 10^{-3}$	2.02 ± 0.12
Total	$3.91 \pm 0.14 \times 10^{-3}$	1.98 ± 0.06
1977		
Pulsed	$5.7 \pm 2.2 \times 10^{-4}$	1.8 ± 0.7
Nonpulsed	$3.19 \pm 0.27 \times 10^{-3}$	2.05 ± 0.15
Total	$3.76 \pm 0.20 \times 10^{-3}$	2.02 ± 0.07
1976+1977		
Pulsed	$6.3 \pm 1.4 \times 10^{-4}$	1.8 ± 0.3
Nonpulsed	$3.20 \pm 0.17 \times 10^{-3}$	2.05 ± 0.10
Total	$3.83 \pm 0.11 \times 10^{-3}$	2.00 ± 0.05

E_o = 40 keV

5.4 DISCUSSION

The 1976 integrated pulse profiles all appear to be consistent with the mean pulse profile. Some profiles look "cleaner" than others, but this is to be expected because of statistical fluctuations. The primary and secondary peaks are readily identified. This is not the case for the 1977 integrated pulse profiles. The profiles obtained on Days 12 and 14, in particular, do not have well defined pulse shapes. The Day 13 pulse profile appears to have a peak which precedes the primary peak by six to seven

milliseconds. The largest flux value in this peak was determined by the chi-squared analysis to be statistically improbable as a measurement of the nonpulsed emission. It is interesting to note that all three days with "questionable" pulse profiles occurred during the latter half of the 1977 observation. The pulsed flux also decreased significantly during Days 12 and 13, with the primary pulse flux decreasing on Day 13 and the interpulse flux decreasing on Day 12. These results suggest that there may be systematic errors in the timing analysis which are strongly affecting the results. As discussed in Section 5.2, there is a large discrepancy (one pulse period per day) between the number of pulses predicted by the Five College pulsar parameters and the parameters used in the present analysis. When the data were binned using the Five College preliminary parameters, no pulsations were seen on any one day or for the entire observing interval. The parameters used here immediately revealed pulsations during each of the first three days (Days 9-11) and for Day 13. The cause of this apparent discrepancy is not yet understood.

Another interpretation of the variations in the nonpulsed emission is that variable pulsed emission is occurring in the so-called nonpulsed emission region. Two possibilities then arise; either the nonpulsed emission varies uniformly as a function of phase and is indistinguishable from nebular

emission; or there exists pulsed structure within the nonpulsed region at a level below the sensitivity of the Celestial X-ray Detector. Of these possibilities the former is less likely. Wolff et al. (1975) detected no contribution of the pulsar to the emission below 23 keV in the nonpulsed region of the integrated pulse profile during two lunar eclipses of the Crab in 1974. Toor and Seward (1977) during a lunar eclipse measurement concurrent with one of the two observed by Wolff et al. also found no evidence of nonpulsed emission from the pulsar in the energy range from 0.5 to 16 keV.

There is no evidence for additional permanent pulsed structure in the integrated pulse profiles shown in Figure 5-6. The profiles, however, are consistent with the presence of a feature on the rising edge of the secondary peak (Brini et al. 1971; Helmken 1975).

The observed variation of pulsed fraction with energy agrees well with the results of previous observations as tabulated by Thomas and Fenton (1975) and with the recent results of Ryckman et al. (1977). The agreement is particularly good for the results of the combined observations. Fluctuations in the pulsed fraction results obtained from the 1976 and 1977 observations separately are statistical in nature. The spectral fits presented in

Section 5.3 showed no unexpected results. The data from 16 to 21 keV were excluded from the fits because this is the spectral range in which contamination by charged particles has been observed. The pulsed spectrum is harder, although not significantly so at the 68% confidence level. The 1976 and 1977 results individually are consistent with the results of the combined observations.

Examination of the nonpulsed and total spectra shown in Figures 5-10 through 5-18 reveals a consistently high point between 33 and 40 keV in the results from both the 1976 and 1977 observations. The conversion from observed count rate to incident flux in this channel is difficult for several reasons. Both Cs and I K-edges are contained in this channel making it very sensitive to both dead-layer and fluorescent escape corrections. There is also some uncertainty in the exact position of the pulse height channel edges below 45 keV. These are nonuniform because of a nonlinearity in the pulse amplifier preceding the pulse height analyzer and it has proved difficult to exactly calibrate this nonlinearity.

Of the above effects neither the fluorescent escape correction nor the dead-layer correction alone can account for the observed excess. Setting the escape parameter equal to zero reduces the 5.4σ excess in the total flux to a 3.3σ

excess and does not significantly alter the spectral index. Similarly, converting counting rate to photon flux with a value of zero for the dead layer reduces the excess in the 33 to 40 keV channel. In this case the spectrum below 33 keV also is strongly affected.

It is not clear from the observed spectra that these lower-energy data are incorrect. It is, therefore, most likely that the excess flux between 33 and 40 keV results from the inability to precisely determine the low-energy pulse-height channels.

5.5 CONCLUSIONS

The Crab nebula and the pulsar PSR 0531+21 have been observed for eight days in 1976 and six days in 1977 using the Celestial X-ray Detector on OSO-8. The pulsed flux during the 1976 observation, measured day by day in the energy range from 16 to 114 keV, was constant to within statistics. The nonpulsed emission, defined to be that emission occurring after the secondary peak and before the primary peak in the integrated pulse profile, exhibited stochastic fluctuations which may be indicative of transient emission from the pulsar. The results from the 1977 observation showed nonstatistical fluctuations in the pulsed emission and in the structure of the integrated pulse profile which cannot be attributed to any known systematic

error. The nonpulsed emission was constant to within statistics during the 1977 observation. The properties of the mean x-ray emission in 1976 and 1977 separately, and of the combined observations, agree well with the results of previous measurements.

The observations reported here are the first to use a single instrument to observe the pulsed emission of the Crab continually on these time scales. Because most of the possible systematic effects associated with each day's results are expected to be the same, the reported variability in x-ray emission is more credible than if the same level of variabliity had been observed using several different instruments.

Chapter 6

HERCULES X-1

6.1 INTRODUCTION

The emission from Her X-1 is complex at all x-ray energies. Intense soft x-ray emision (<1 keV) has been observed by Catura and Acton (1975) and Shulman et al. (1975). The time-averaged spectrum from 2 to 20 keV is well fitted with a power-law spectrum. Holt et al. (1974) report a photon spectral index of 1.05 from the results of a 1973 rocket observation. Becker et al. (1977) report a spectral index of 0.91±0.05 for data obtained during a 1975 satellite observation. Pravdo et al. (1977) report iron lines in the spectrum during the ON-state.

Above 20 keV the Hercules spectrum falls off much more rapidly than an extrapolation of a thermal fit to the lower-energy data would predict. Becker et al. (1977) fit their observed spectrum with a quasi-thermal spectrum having a temperature of 7.3 (+3.6, -2.4) keV. Trümper et al. (1978) report that the pulsed continuum they observe is best fit with a thermal spectrum with a temperature of 7.3 (+2.4, -3.8) keV.

Recent observations of the high-energy x-ray emission from Her X-1 indicate that the pulsed x-ray spectrum above 20 keV contains one or more spectral features and is highly variable as a function of time (Trümper et al. 1977, 1978; Trümper 1978; Kendziorra et al. 1977; Matteson et al. 1978; Gruber et al. 1978). Trümper reports a decrease by a factor of 2.7 in the intensity of both the pulsed continuum and the 58-keV line feature between 1976 May and 1977 September. Matteson et al. and Gruber et al. report an excess flux in the pulsed spectrum above the low-energy pulsed continuum at a level similar to that observed by Trümper in 1977 September. The measured values of the pulsed fraction also have varied considerably, with values in the energy range from 16 to 45 keV ranging between an upper limit of 10% of the total flux (Iyengar et al. 1974) to a value of 58±8% (Kendziorra et al. 1977).

There also is evidence for considerable fluctuations in the time-averaged spectrum of Her X-1 including the observation of a very strong line feature at 63 keV (Coe et al. 1977). Earlier observations made from balloons suggest, when compared to more recent observations using both balloons and satellites, that the time-averaged spectrum has become significantly steeper since 1973 (Iyengar et al. 1974; Manchanda 1977; Dennis et al. 1978a). It is possible that some of these apparent variations are instrumental in

nature, resulting, for example, from the different instrumental and analytic techniques used by the different observers. Extended observations of Her X-1 made with a single instrument are, therefore, especially valuable in the search for systematic variability in the high-energy x-ray emission.

Such a long-term observation was performed in 1977 September using the Celestial X-ray Detector. The results from this observation for the time-averaged spectrum and preliminary pulsed-flux results were presented by Dennis et al. (1978a, 1978b). The work presented here is a detailed analysis of the observed pulsed flux. The results of the observation indicate that significant changes in pulsed flux intensity may have occurred from binary orbit to binary orbit. The observed changes, although of limited statistical significance, serve to further characterize the temporal variability of the source.

A discussion of the analytic techniques unique to the Hercules observation is presented in Section 6.2. The experimental results are presented in Section 6.3. In Section 6.4 the results from the present work are discussed in relation to previous observations and currently available models for x-ray emission from Her X-1.

6.2 OBSERVATION AND DATA ANALYSIS

Hercules X-1 was observed with the Celestial X-ray Detector from 1977 August 31 to 1977 September 10. The observation, during which the detector was sensitive to photons with energies between 14 and 281 keV, spanned nearly and entire ON-state, and is the first observation in this energy range to do so.

During the analysis of the Hercules data, difficulties were encountered both in the construction of the integrated pulse profile and in the determination of the source spectrum. An inaccurate value of t_s, the time of superior conjunction, was mistakenly used in the preliminary analysis of the data. The error in t_s, 0.0036 day, corresponds to an error in the angular position of the x-ray source in its binary orbit of 0.7°. An error of this magnitude was sufficiently large to prevent the successful construction of an integrated pulse profile over a time interval of seven days. Indeed, when the data were examined binary orbit by binary orbit, the pulse peak appeared to change phase systematically as a function of binary orbit. For this reason a frequency derivative was included in the pulsar parameters and different values of both frequency and frequency derivative were tried in an effort to remove the variation in peak position with time. No suitable set of parameters was found. The use of the correct time of

superior conjunction removed the problem and phase stability was maintained for the duration of the observation. The timing parameters used for the analysis of the Her X-1 data are shown in Table 10.

TABLE 10

Hercules X-1 Timing Parameters

Pulsation period*	1.237796600 s
Binary period**	1.7001656 d
Binary Radius**	13.183 light-s
Superior conjunction*	1977 August 31.2778 UT

*Pravdo (1978).
**Becker et al. (1977).

The problem encountered during the spectral analysis was the occurrence of a change in photomultiplier gain as a function of the rotation of the satellite. The effect of the gain change was to induce peaks at 60 and 135 keV in the time-averaged spectrum of Her X-1. These features, which resembled lines in the spectrum, were close in energy to those reported by other observers, so that the initial results were very misleading. Because of the high intensities of the features, and the slight discrepancy in energy compared to previous observations, the data were

re-examined with particular emphasis on small systematic errors which could produce the observed effect. It was found that a periodic gain change, with a magnitude of even less than 1%, during the rotation of the wheel section of the satellite could result in the appearance of these features. The gain change essentially shifted the nominal energy at which an event was recorded. The background rate in any energy bin became a function of the wheel rotation angle as different numbers of events were moved into and out of the bin as a result of the gain change. This varying background rate in the different energy bins masqueraded as an apparent source. Consequently, incorrect values of the observed source strength were calculated. The energies and strengths of the apparent features can be predicted from the shape of the background spectrum, which contains peaks as a result of the induced radioactivity discussed in Chapter 2. The background spectrum, and the apparent source spectrum caused by a 1% change in gain, are shown in Figure 6-1.

The cause of the gain change is apparently the changing orientation of the photomultiplier tubes with respect to the earth's magnetic field. Although the photomultiplier tubes are surrounded by magnetic shielding, the detector design prevented the shielding from extending beyond the photomultiplier tube faces. The magnetic shielding, therefore, is less than ideal. It should be noted that a

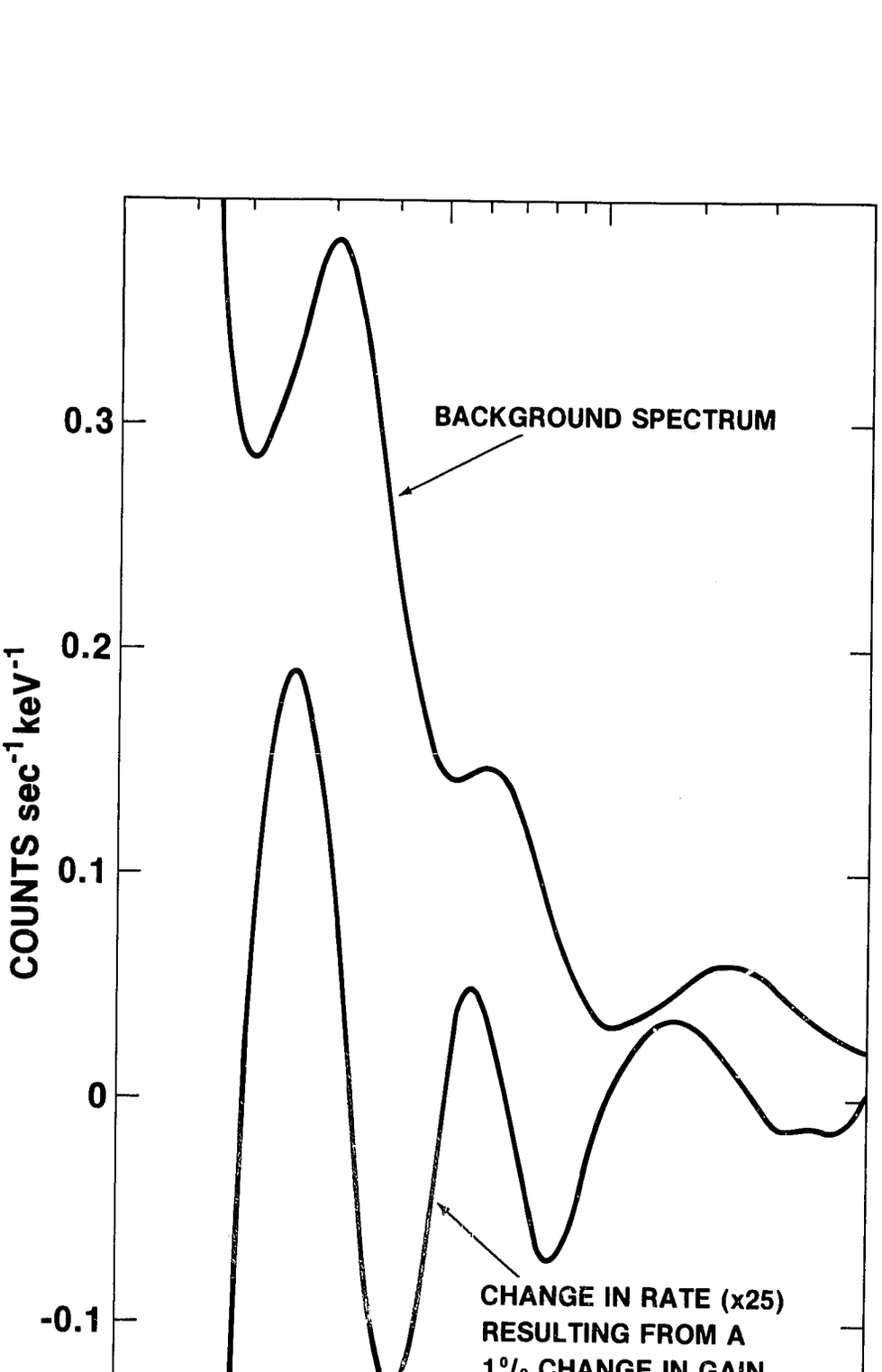

Figure 6-1. The observed background spectrum and the apparent source spectrum (magnified by a factor of 25) resulting from a 1% change in the gain of the photomultiplier tubes.

gain change of this magnitude (<1%) would be quite difficult to detect during pre-launch calibration. Moreover, since this is a problem associated with the background subtraction, it does not affect the pulsed spectrum, as discussed in Chapter 2. Because it involves a difference measurement between the on-source and off-source backgrounds, the effect is less significant for strong sources than it is for weak ones. It did not, therefore, present problems during the analysis of the Crab data described in Chapter 5. A more detailed discussion of this effect has been presented by Dennis et al. (1978a, 1978b).

6.3 RESULTS

Integrated pulse profiles, obtained by binning each event according to phase, are shown in Figure 6-2 for energies up to 98 keV. The pulsed emission between 16 and 33 keV clearly occurs during 30% of the profile width. Since the statistical significance of the pulse profiles deteriorates rapidly above 33 keV, the relative phase and width of the pulsed emission region below 33 keV was used to define the pulsed emission at higher energies.

The variation of pulsed flux with binary orbit is shown in Figure 6-3. It should be noted that the last observed binary orbit, centered on September 11.33, occurred after the end of the ON-state as defined at lower energies (Pravdo

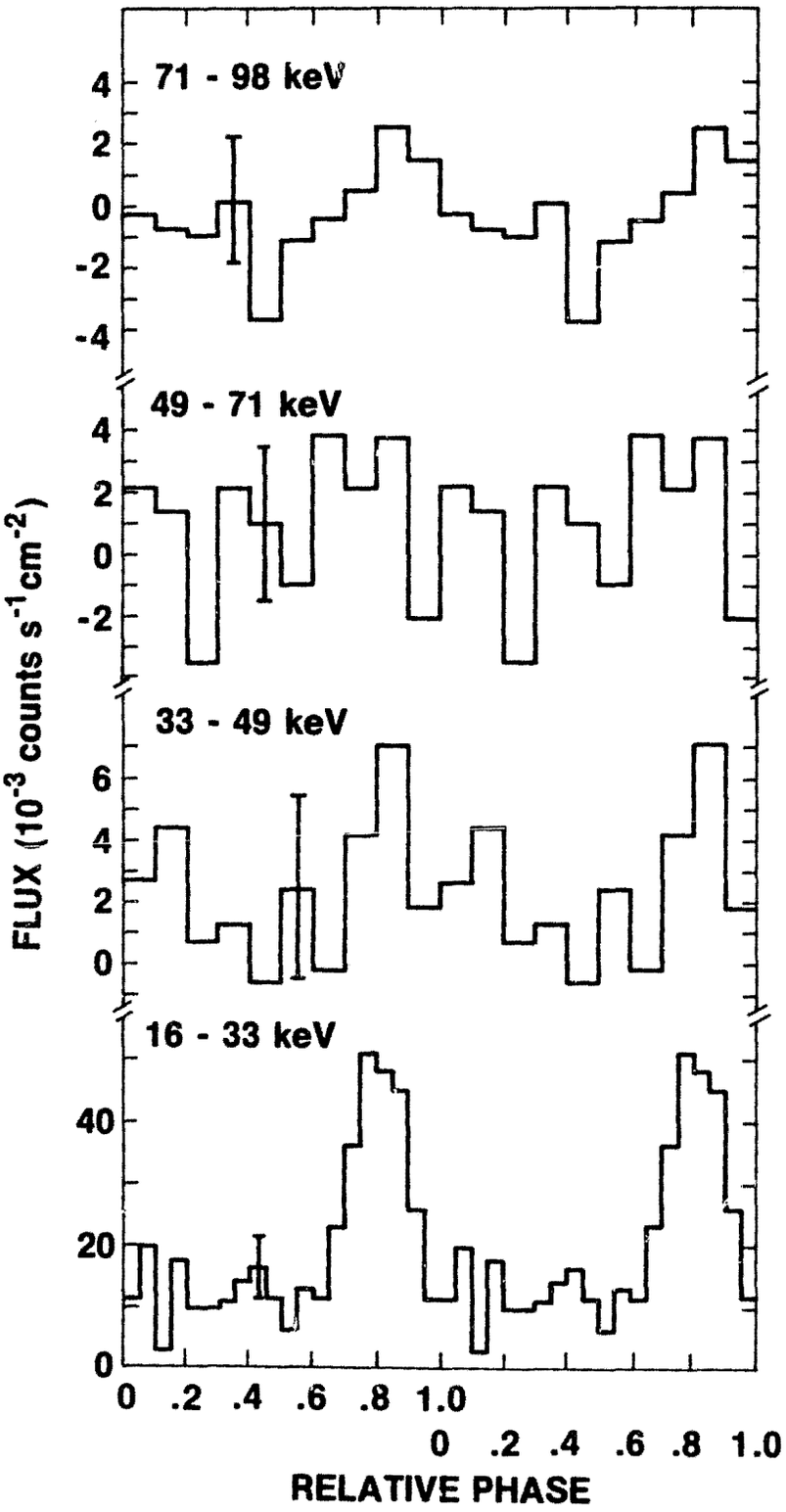

Figure 6-2. Integrated pulse profiles for the interval 1977 August 31 - September 6, which covers the noneclipsed portion of the first four binary orbits after the start of the observation. No significant pulsed flux was detected above 98 keV.

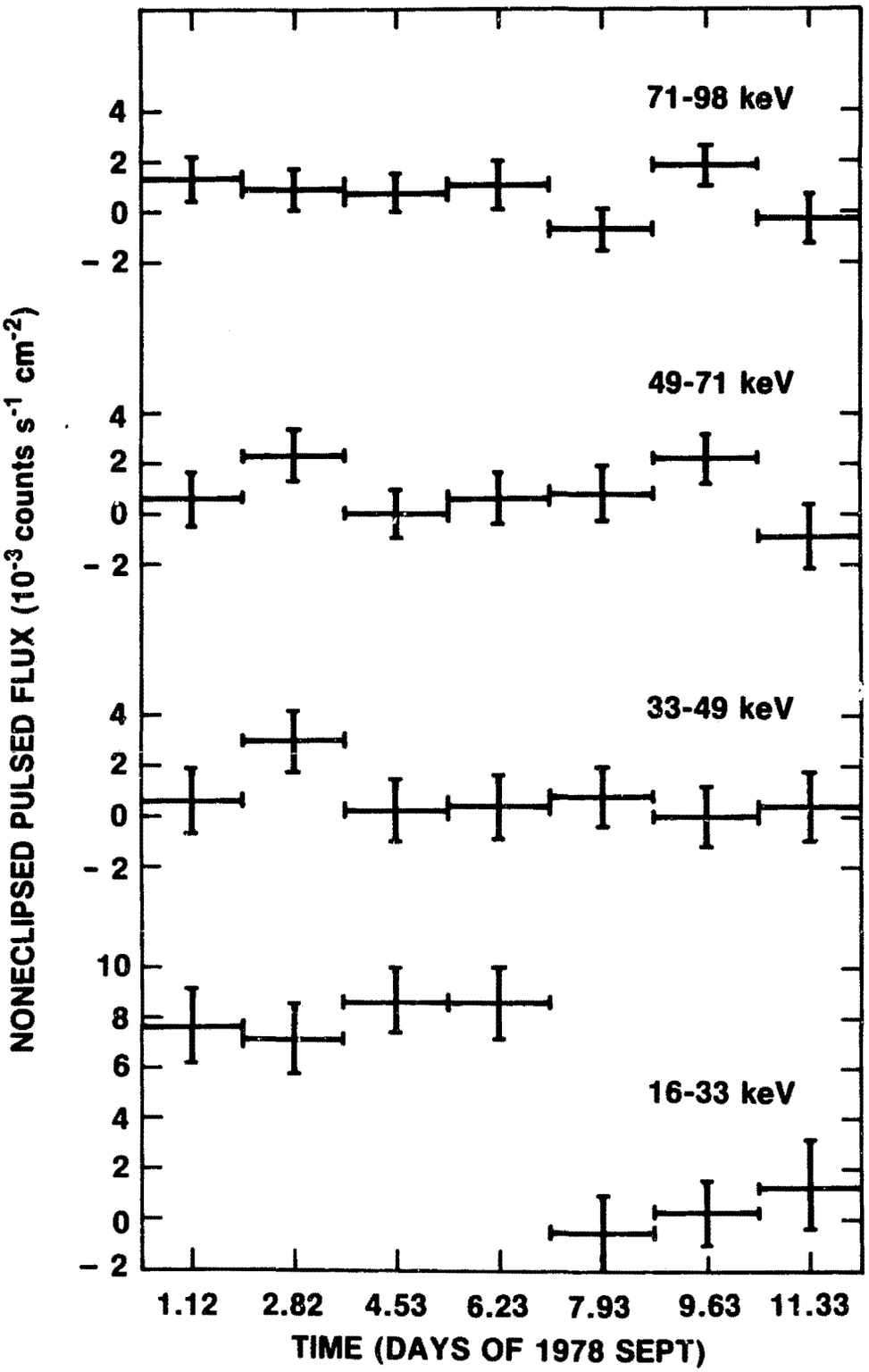

Figure 6-3. The variation of pulsed flux with binary orbit. The last observed binary orbit, centered at September 11.33, occurred after the end of the ON-state as defined at lower energies (Pravdo 1978).

1978). The pulsed flux in the 16 to 33 keV interval is consistent with constant emission during the first four binary orbits and with zero emission thereafter. The pulsed flux in binary orbit 2 was observed to increase in both the 33 to 49 keV and the 49 to 71 keV energy intervals with a combined statistical significance of 1.9 σ. During the sixth observed binary orbit, the pulsed flux between 49 and 98 keV was observed to increase with a statistical significance of 2.5 σ.

The distribution of flux as a function of binary phase is shown in Figure 6-4 for the first four binary orbits (1977 August 31 through September 6) with the binary eclipse occurring between phase 0.93 and 0.07. The noneclipsed data are consistent with constant emission, although there is a systematic trend in the flux between 16 and 33 keV. This trend, although statistically marginal, suggests that the pulsed flux increases linearly with binary phase. The low value of flux between phases 0.79 and 0.93 is due to the presence of intensity dips which occurred exclusively in this binary phase bin for the first four binary orbits (Pravdo 1978). Pulsed flux, with a statistical significance of 2.2σ, was observed between 71 and 98 keV during eclipse. No significant pulsed flux was observed at lower energies during the same time interval.

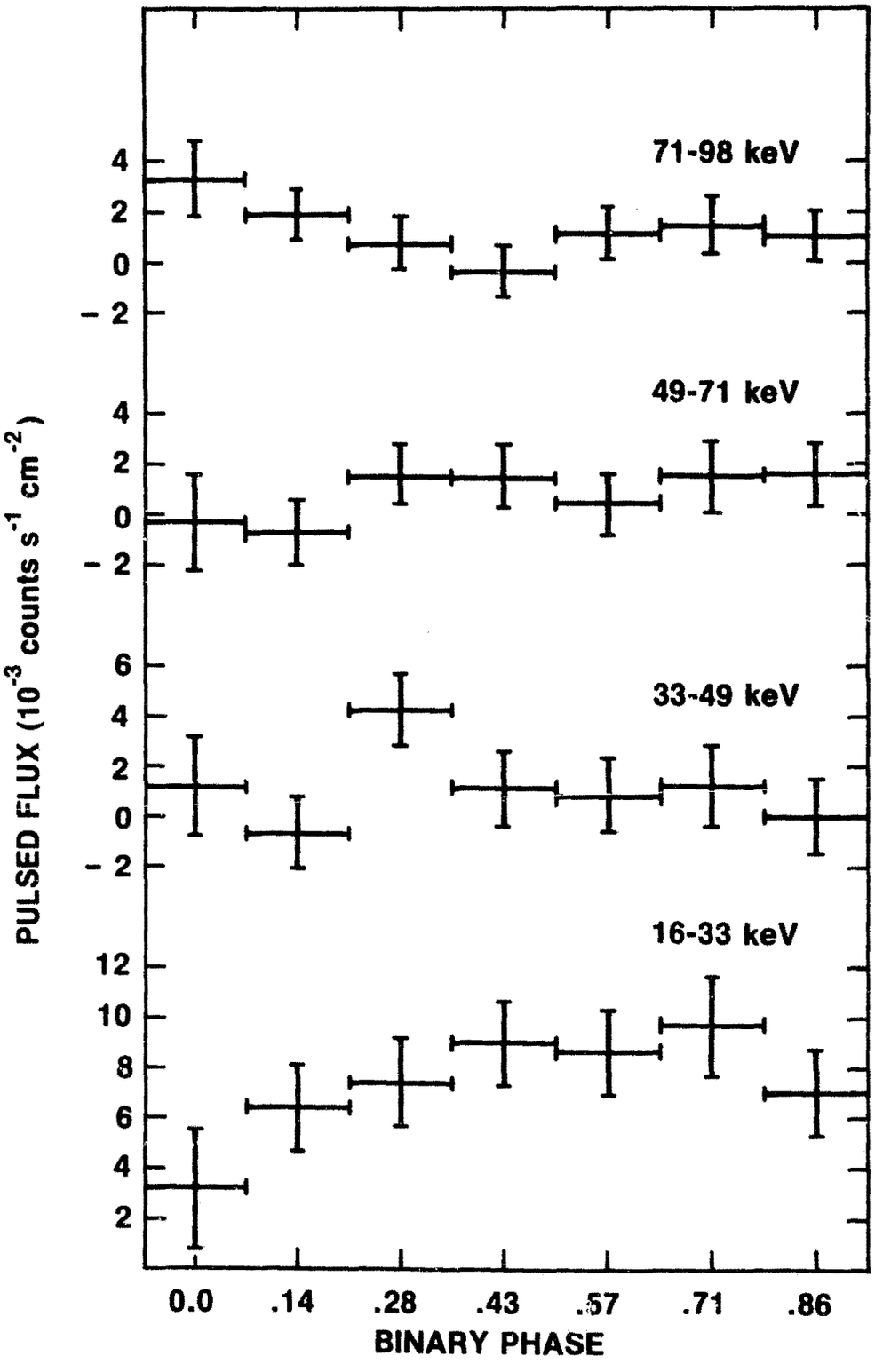

Figure 6-4. The variation of pulsed flux as a function of binary phase. The plot includes data between 1977 August 31 and September 6, covering the first four binary orbits after the beginning of the observation. The phase interval between 0.93 and 0.07 covers the binary eclipse times and the phase interval between 0.79 and 0.93 includes the times of the absorption dips observed at lower energies.

The value for the pulsed fraction of emission between 16 and 33 keV obtained during this observation is plotted in Figure 6-5 along with several previously reported values. There seems to be some fluctuation in the measured values above 20 keV.

The pulsed spectrum of Her X-1 for the time interval 1977 August 31 through 1977 September 6 is shown in Figure 6-6. The spectrum can be fitted by a power law of the form

$$(6\text{-}1)\quad \frac{dN}{dE} = (1.7\pm0.4)\times10^{-3}\ (E/25)^{-\left\{5.4^{+5.0}_{-3.2}\right\}} \quad \text{photons s}^{-1}\ \text{cm}^{-2}\ \text{keV}^{-1}.$$

a thermal spectrum of the form

$$(6\text{-}2)\quad \frac{dN}{dE} = \frac{(4.1\pm0.7)\times10^{-2}}{E}\ \exp\left\{\frac{-(E-25.2)}{5.8^{+5.9}_{-2.4}}\right\} \quad \text{photons s}^{-1}\ \text{cm}^{-2}\ \text{keV}^{-1}.$$

and a thermal spectrum with a superposed gaussian

$$(6\text{-}3)\quad \frac{dN}{dE} = (3.6\pm0.8)\times10^{-2}\ \exp\left\{\frac{-(E-19.5)}{5.7^{+5.2}_{-2.4}}\right\} + (4.1\pm2.6)\times10^{-2}\exp-\left\{\frac{(E-55)^2}{4}\right\}$$

photons s^{-1} cm $^{-2}$ keV^{-1}

The uncertainties are derived from the 68% confidence contours in chi-squared space as described by Lampton et al. (1976). For the latter fit, the thermal (line) parameters were held fixed for the determination of the uncertainties on the line (thermal) parameters. The normalization energies (25.2 and 19.5 keV, respectively) for the thermal

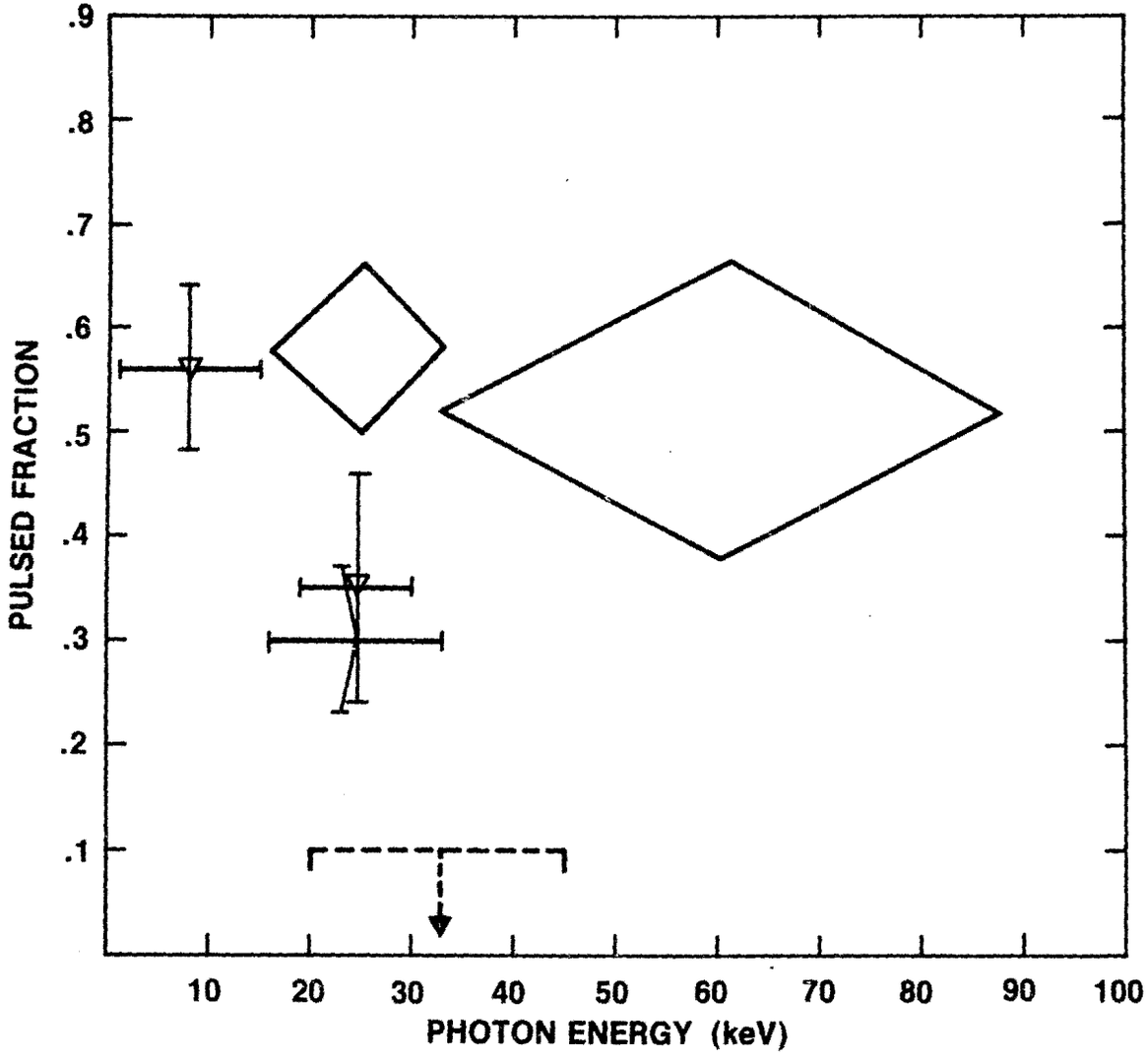

Figure 6-5. The pulsed fraction as a function of photon energy. Iyengar et al. (1974); Joss et al. (1976); Kendziorra et al. (1977); present observation.

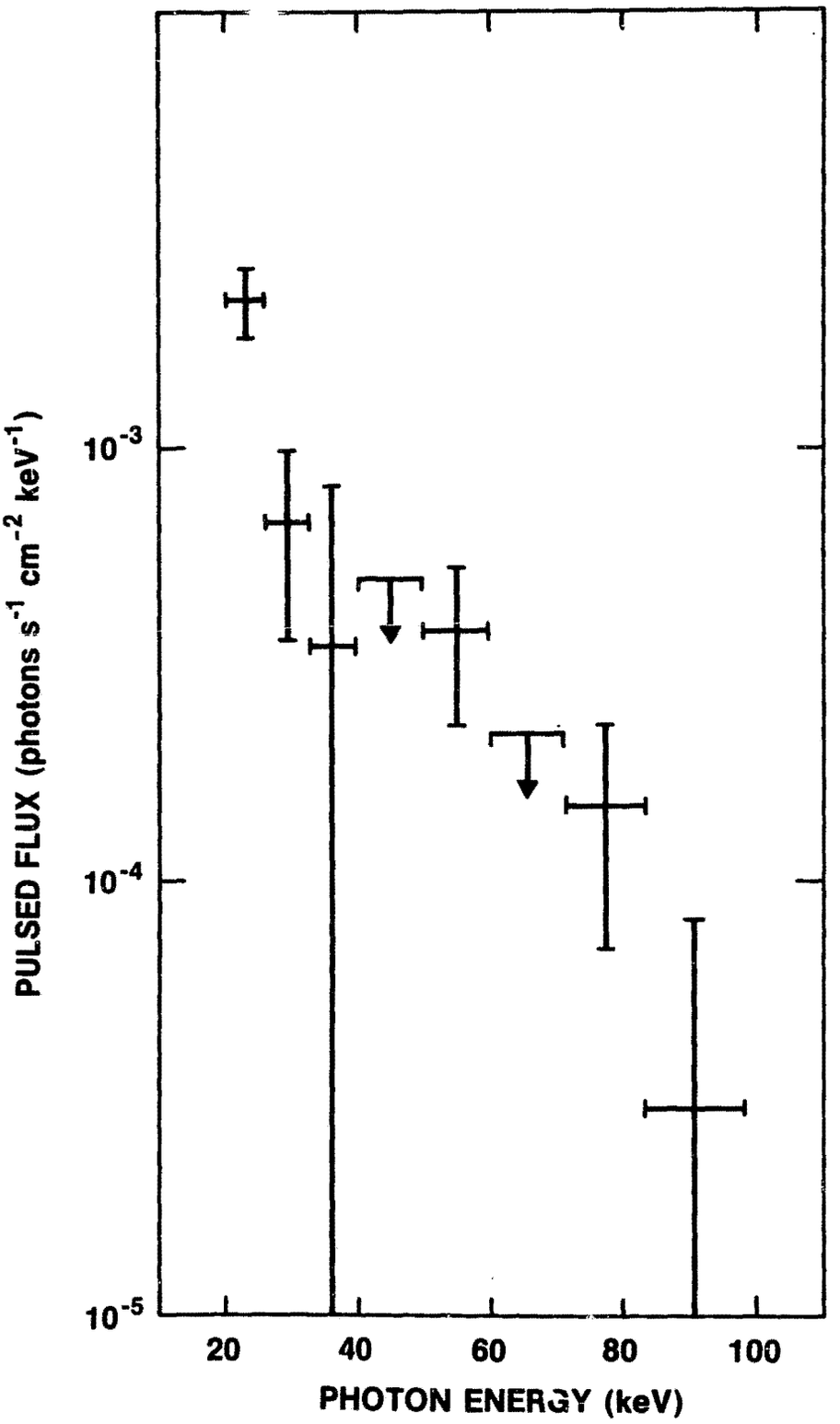

Figure 6-6. The pulsed x-ray spectrum of Her X-1 for the time interval 1977 August 31 -September 6.

spectra were chosen so as to circularize the contours of equal chi-squared, thus making the parameters statistically independent. The width, FWHM, of the line centered at 55 keV is 3.4 (+9.1,-2.6) keV and the integrated intensity is $1.5\,(+4.1,-1.4)\times10^{-3}$ photons s^{-1} cm^{-2}. The value of chi-squared for the first two fits is 21 for 14 degrees of freedom, while the value for the latter fit is 14 for 12 degrees of freedom.

6.4 DISCUSSION

The Hercules X-1 observation presented here provides information on three different aspects of the pulsed x-ray emission: the variation of pulsed flux as a function of the time from the beginning of the ON-state, the variation of pulsed flux as a function of binary phase, and the energy spectrum of pulsed emission.

The intensity as a function of time from the beginning of the ON-state, as exhibited by the 16 to 33 keV pulsed flux, differs qualitatively from the behavior of the total intensity determined by other observers. In particular, the sharp cutoff in intensity following the fourth observed binary orbit differs from the gradual decrease reported by Giacconi et al. (1973) and Pravdo (1976). The occurrence of

larger than average intensity dips during the fifth and sixth binary orbits is not responsible for the low flux values. Analysis of these orbits both including and excluding the dips produces the same flux values to within the statistical uncertainty. Joss et al. (1978) have presented an analysis of the 2 to 6 keV pulsed flux from Hercules X-1 from three consecutive ON-states. They report no significant variations in the observed nonpulsed flux. The variations which they report in the pulsed fraction, therefore, can be compared directly with the results presented here. It should be noted, however, that the first binary orbit as defined in this work is the first complete binary orbit of the ON-state, and corresponds to the second orbit of Joss et al. (1978). The 16 to 33 keV pulsed flux variations shown in Figure 6-3 agrees qualitatively with the pulsed fraction variations presented by Joss et al. (1978); the decrease in pulsed fraction which they observe following their fifth binary orbit, however, is not so rapid.

The variation of pulsed flux between 33 and 71 keV appears not to be correlated with the variations observed between 16 and 33 keV discussed above. The increase observed during binary orbit 2 suggests that changes in flux of the magnitude observed by Trumper can occur from binary orbit to binary orbit. The results presented recently by Gruber et al. (1978) also indicate significant changes in the

high-energy pulsed x-ray emission from binary orbit to binary orbit.

Two interesting results were obtained from the analysis of pulsed emission as a function of binary phase. The trend of increasing pulsed flux with increasing phase observed here disagrees with the result of Joss et al. (1978), who observed higher pulsed fraction values before midorbital phase than after. Their results, together with those presented here, reinforce the hypothesis that significant changes occur in the pulsed emission from ON-state to ON-state.

The other unexpected result in the analysis of variations with binary phase was the observation of pulsed flux between 71 and 98 keV during eclipse. This is especially suprising in view of the absence of pulsed flux at lower energies. The statistical significance of the observed flux is low; however, when considered along with the positive flux between 2 and 6 keV measured during an eclipse by McClintock et al. (1974), it suggests that variable emission during eclipse is possible.

There is considerable scatter in the spectral data between 33 and 98 keV. Power-law and thermal spectra without features fit the data equally well. Because others

have observed a feature in the spectrum near 55 keV, a thermal spectrum with a superposed gaussian was fitted to the data. The peak of the gaussian was fixed at 55 keV during the fitting procedure, but its width and intensity were allowed to vary. The resulting integrated intensity of $1.5\ (+4.1,-1.4) \times 10^{-3}$ photons $s^{-1}\ cm^{-2}$ has low statistical significance but is consistent with the value of $1.1\ (\pm 0.1) \times 10^{-3}$ photons $s^{-1}\ cm^{-2}$ obtained by Trumper during the same ON-state. The narrow width of the feature leads to the result that the gaussian rises and falls within one 10-keV wide energy interval. The limited statistical significance of the feature makes its interpretation as a line speculative. The goodness of fit as measured by chi-squared, however, is better for the spectrum with the line feature than for either of the spectra without line features. Moreover, the shape of the spectrum obtained in the present work is consistent with that obtained by the HEAO A-4 experiment from an observation of Her X-1 in 1978 February (Matteson et al. 1978).

A comprehensive model for the x-ray emission from Her X-1 must explain all of the spectral properties described above as well as the complicated temporal behavior of the source. The various models which have been proposed to perform this task have already been described in Chapter 4. In the following paragraphs these models will be considered in light of specific observational results.

The iron line observed by Pravdo et al. (1977) has been interpreted as fluorescence from a subrelativistic shell at the Alfven radius. The existence of this shell was postulated by McCray and Lamb (1976) to explain the intense soft (< 1 keV) x-ray radiation.

Boldt et al. (1976) have used the modification of the Thomson scattering cross section to explain the sharp cutoff in the energy spectrum near 20 keV. By using a cyclotron energy of 100 keV, they have been able to reproduce the shape of the observed spectrum up to energies near 30 keV.

The 57-keV line in the x-ray spectrum has been interpreted by Trumper et al. (1978) as a cyclotron line. The observation of a statistically significant pulse profile at energies near the cyclotron energy calls into question the explanation of Basko and Sunyaev (1975) for the beaming mechanism. This model predicts, on the basis of the anisotropy in the Thomson scattering cross section, that the pulse shape, degree of modulation, and pulsed fraction at high energies will differ from those observed at lower energies. The observations do not confirm this prediction.

Trumper et al. (1978b) suggest that the narrowness of the observed line ($\Delta E/E = 0.20$) supports a fan-beam emission geometry; this value for the relative width requires that

the angle between the magnetic field and the line of sight be greater than 70°. Pravdo et al. (1978), on the other hand, state that a pencil beam of the type proposed by Basko and Sunyaev (1975) and Tsuruta (1975) is more likely on the basis of their data.

Pravdo et al. (1977, 1978) have shown that significant variations in spectral index occur within the pulsed part of the integrated pulse profile. They originally proposed Thomson scattering as the cause of the spectral variatons, but later suggested that cyclotron absorption should dominate Compton scattering above 20 keV.

It is clear from the above discussion that, even without the complication of the high-energy line, there is no general concensus regarding the detailed geometry of the emission region or the radiative processes responsible for the observed spectrum. The interpretation of the line also is not unique. Trumper et al. (1978) have proposed transitions from the first excited Landau state as the mechanism for the observed emission. They suggest that cyclotron absorption is a possible but less likely mechanism. Gruber et al. (1978) using data obtained with the A4 experiment on HEAO-1 during 1978 February cannot distinguish between a cyclotron emission line at 56 keV with indeterminate width and a cyclotron absorption dip centered at 40 keV with a width of less than 30%.

The continuum under the lines observed by Trumper *et al.* (1978) is approximately thermal, having a temperature of 7.3 (+2.4, -3.8) keV. This temperature agrees well with the result obtained from the present observation. If the temperature does in fact represent the average kinetic energy of the particles in the emitting region, however, it is difficult to see how the Landau levels would be excited.

To eliminate these difficulties, Bonazzola *et al.* (1978) have proposed resonant Compton-cyclotron scattering to explain the Her X-1 x-ray spectrum. In this model the emission of x-rays occurs at a hot spot (7×10^7 K < T < 1.8×10^8 K) near the surface of the neutron star. The spectrum of the emitted radiation is expected to be blackbody. The radiation is then reprocessed in the significantly cooler (T = 2 keV) plasma in the accretion column. A resonance occurs in the scattering cross section for the extraordinary mode photons (see Chapter 3), leading to strong absorption at the cyclotron energy. The spectrum calculated from this model reproduces qualitatively the power-law low-energy spectrum, the approximately thermal high-energy spectrum, and the presence of features near the cyclotron energy.

6.5 CONCLUSIONS

Her X-1 has been observed between 16 and 280 keV for an entire ON-state. Significant pulsed flux was measured during the first four of seven binary orbits observed. This observation, which is the first to continually monitor the source in this energy range for a complete ON-state, suggests that the pulsed emission can vary in intensity by a factor of three from binary orbit to binary orbit.

The spectral data are better fit by a thermal spectrum with a superposed gaussian centered at 55 keV than by power-law or thermal spectra without features. The low statistical significance of this feature in the spectrum, however, makes independent interpretation of it as a line impossible on the basis of our data. In the light of other observations, however, our results add credibility to the existence of a variable feature in the high-energy x-ray spectrum of Her X-1.

Chapter 7

CODA

In the years which have passed since the Celestial X-ray Detector was proposed, high-energy x-ray astronomy has advanced tremendously. A better understanding of detector performance and the background counting-rate spectrum at balloon and satellite altitudes has led to significant improvements in detector design. These improvements, along with the ability to launch larger scientific payloads, have enabled a reduction in the minimum detectable source strength by more than an order of magnitude.

Scientific advances in high-energy x-ray astronomy depend on improvements in the ability to detect low continuum fluxes and the ability to make spectral measurements with fine energy resolution. The first need is being met by the use of large scintillation detectors with sensitive areas in excess of 750 cm^2. These detectors provide the capability to resolve some of the issues raised by the work presented here. In particular, variability at the two-sigma level of statistical significance can be confirmed or ruled out, as the case may be. Large-area detectors can be used also to observe high-energy x-ray sources too weak to be detected

with the previous generation of instruments. Among the most exciting candidates for such observations are extragalactic x-ray sources such as Seyfert galaxies and BL Lac objects. These are, generally speaking, low-intensity sources with very flat spectra (Mushotzky et al. 1978). Knowledge of their high-energy x-ray spectra is essential for the verification of models proposed for their structure. For example, coordinated x-ray, infrared, and radio observations will clarify the interpretation of the processes occurring in these active sources in terms of the synchro-Compton and blackbody-Compton models (Grindlay 1975; Mushotzky 1977; Tucker et al. 1973; Beall et al. 1978). The possible contribution of these sources to the diffuse component of the cosmic x-ray flux can also be better estimated from a knowledge of their high-energy x-ray spectra.

The improved counting statistics obtained with large-area detectors enables more precise determination of source spectra to be made, thus improving the ability to detect spectral breaks and possible line features. Breaks in spectra can support or refute models for x-ray production, as in the case of Cyg XR-1, where the latest models predict a break at an energy between 100 and 500 keV (Shapiro et al. 1976; Eardley and Lightman 1976). A break in the Crab spectrum has been reported by Strickman et al. (1979) but its theoretical implications are not clear at this time.

The capability of scintillators to determine fine spectral features is limited by the inherent energy resolution of the scintillation process, which results in a best-possible resolution of approximately 7% at 660 keV. To overcome this difficulty, experimenters are turning to the use of semiconductors such as germanium for the detection of high-energy photons. Germanium has an intrinsic energy resolution more than an order of magnitude finer than scintillators, typically 2 to 3 keV at 1 MeV. The largest germanium crystals currently available provide detecting areas on the order of 30 cm^2 and volumes on the order of 100 cm^3. The small size of these crystals has limited their application in astrophysics. The use of large arrays, comprising many individual detecting units, will remove this limitation.

Measurements made with germanium detectors should be able to resolve the ambiguities now present in the interpretation of the 55-keV feature in the x-ray spectrum of Her X-1. Fine energy resolution in the energy range characterizing the high-energy x-ray and low-energy gamma-ray emission will enable exploration for other spectral features in a wide variety of additional sources, such as other x-ray binaries, the interstellar medium, supernovae, and solar flares. Narrow features are expected from several mechanisms, including cyclotron line emission from hot plasmas, nuclear transitions, and positron annihilation.

Fine time resolution will continue to be an important requirement for future observations. The determination of spectra as a function of pulse phase for periodic sources will provide insight on both emission and absorption processes. Autocorrelation studies which are now being used to study aperiodic low-energy x-ray emission from black hole candidates require fine time resolution; the increased sensitivity of large-area scintillators may make such analysis feasible at higher energies.

High-energy x-ray astronomy, because of advances in both science and technology, will continue to be an active and exciting area of astrophysics research.

Appendix A

COLLIMATOR PENETRATION EFFECTS

The sensitive area of a collimated detector to a parallel beam of x rays is a function of x-ray energy and the angle between the cllimator axis and the photon momentum. At low energies, the collimator material is completely opaque to the x-rays; as the angle between the collimator axis and the photon direction increases, the sensitive area decreases as the cllimator blocks the passage of photons to the detector itself. At higher energies, however, photons may penetrate the collimator material, so that at a given angle the sensitive area is increased.

The effects of cllimator penetration for the Celestial X-ray Detector on OSO-8 have been calculated following the treatment of Mather (1957). Several results from that calculation are presented here.

Three fundamental assumptions were made in the calculation. First, the angle, , of photon incidence as measured from the collimator axis is assumed to be small enough so that small-angle approximations are valid.

Secondly, the penetration of photons through the maximum thickness of collimating material is assumed to be negligible. Thirdly, the collimator is assumed to comprise a single cylindrical hole in a semi-infinite slab of collimating material. The first assumption is straightforward, and is used to set $\cos\theta$ approximately equal to 1. The validity of the second assumption can be determined by calculating the probability of penetration through the top shield. This probability is shown for several incident x-ray energies in Table 11. The thickness of the top shield, 13.335 cm, was used in this calculation.

TABLE 11

Probability of Penetration Through Shield

E (keV)	Probability
400	0.00075
500	0.0042
600	0.008
700	0.014
800	0.02

The third assumption, namely that the collimator is a single cylindrical hole in a semi-infinite slab, must be examined carefully. The multiple-hole configuration of the OSO-8 detector will enhance the penetration effects because

of penetration through the wall separating two collimator holes. To estimate the size of this effect, angles were calculated at which incoming photons have probabilities of 0.1 and 0.2 for penetrating the minimum wall thickness (0.307 cm) between adjacent collimator holes. These angles are shown in Table 12. Since the average wall thickness is greater than the minimum wall thickness, the values in Table 13 represent the maximum probabilities of penetration and not the average probabilities for photons of the same energy and incident angle.

TABLE 12.

Angles for Penetration of Minimum Wall Thickness

E (keV)	P=0.10 (degrees)	P=0.20 (degrees)
180	13.18	
200	10.37	
220	8.67	12.45
240	7.58	10.89
260	6.89	9.89
280	6.20	8.89
300	5.66	8.11
400	4.13	5.91
500	3.13	4.49
600	2.75	3.94

The effects of multiple hole penetration can be significant, especially above about 400 keV. Consequently, the results from the calculation presented here may not be valid at energies above 400 keV.

The total sensitive area as a function of angular distance from the source was calculated under the above assumptions; the results for photons with energies of 160 and 300 keV and the results assuming no penetration are shown in Figure 2-3.

REFERENCES

American Ephemeris and Nautical Almanac, published yearly. Washington DC: U. S. Government Printing Office.

Ash, M. E., Shapiro, I. I., and Smith, W. B. 1967, A. J., 72, 338.

Backus, P. 1979, private communication.

Basko, M. M. and Sunyaev, R. A. 1975, Astron. and Astrophys., 42, 311.

Beall, J. H., Rose, W. K., Graf, W., Price, K. M., Dent, W. A., Hobbs, R. W., Conklin, E. K., Ulich, B. L., Dennis, B. R., Crannell, C. J., Dolan, J. F., Frost, K. J., and Orwig, L. E. 1978, Ap. J., 219, 836.

Bekefi,G. 1966. Radiation Processes in Plasmas. New York: John 1

Bevington, Philip R. 1969. Data Reduction and Error Analysis for the Physical Sciences. New York. McGraw-Hill Book Company.

Blumenthal, George R. and Tucker, Wallace H. 1974. In X-Ray Astronomy, ed. R. Giacconi and H. Gursky. Dordrecht. D. Reidel Publishing Company.

Bonazzola, S., Heyvaerts, J., and Puget, J. L. 1979, to be published.

Brini, D., Cavani, C., Frontera, F., and Fuligni, F. 1971, Nature Phys. Sci., 232, 79.

Bussard, R. W. 1978, Proc. of Symposium on Gamma Ray Spectroscopy in Astrophysics, Goddard Space Flight Center, Greenbelt, MD. USA, 28-29 April 1978, 404.

Canuto, V. and Venture, J. 1977, Fundamentals of Cosmic Physics, 2, 203.

Catura, R. C. and Acton, L. W. 1975, Ap. J. (Lett), 202, L5.

Cheng, Andrew F. and Ruderman, M. A. 1977, Ap. J., 216, 865.

Cheng, A., Ruderman, M., and Sutherland, P. 1976, Ap. J., 203, 209.

Chupp, E. L. 1976. Gamma Ray Astronomy: Nuclear Transition Region. Boston: D. Reidel.

Coe, M. J., Engel, A. R., Quenby, J. J., and Dyer, C. S., 1977, Nature, 268, 508.

Daugherty, J. K. 1978, Proc. of Symposium on Gamma Ray Spectroscopy in Astrophysics, Goddard Space Flight Center, Greenbelt, MD, USA, 28-29 April 1978, 394.

Daugherty, J. and Ventura, J. 1977, Astron. and Astrophys., 61, 72.

Denisse, J. F. and Delcroix, J. L. 1963. Plasma Waves. New York: Interscience Publishers.

Dennis, B. R., Frost, K. J., Lencho, R. J., and Orwig, L. E. 1977, Space Sci. Inst., 3, 325.

Dennis, B. R., Maurer, G. S., Cutler, F. P., Crannell, C. J., Dolan, J. F., Frost, K. J., and Orwig, L. E. 1978a, Nature, 275, 195.

Dennis, B. R., Maurer, G. S., Cutler, E. P., Crannell, C. J., Dolan, J. F., Frost, K. J., and Orwig, L. E. 1978b, Proc. of Symp. on Gamma-Ray Spectroscopy in Astrophysics, Goddard Space Flight Center, MD, USA, 371.

Dolan, J. F. 1972, Ap. Space Sci., 17, 472.

Hardley, D. M. and Lightman, A. P. 1976, Nature, 262, 196.

Forman, W., Giacconi, R., Jones, C., Schreier, E., and Tanenbaum, H. 1974, Ap. J. (Lett), 193, L67.

Giacconi, R. and Gursky, H. eds. 1974. X-ray Astronomy. Boston: D. Reidel.

Giacconi, R., Gursky, H., Kellogg, E., Levinson, R., Schreier, E., and Tananbaum, H. 1973, Ap. J., 184, 227.

Ginzburg, V. L. 1969. Elementary Processes for Cosmic Ray Astrophysics. New York: Gordon and Breach Publishing Co.

Ginzburg, V. L. and Syrovatskii, S. I. 1964. The Origin of Cosmic Rays. New York: Macmillan Company.

Gnedin, Y. N. and Sunyaev, R. A. 1974, Astron. and Astrophys., 36,379.

Goldreich, P. and Julian, W. H. 1969, Ap. J., 157, 869.

Grindlay, J. E. 1975, Ap. J., 199, 49.

Gruber, D. E., Matteson, J. L., Peterson, L. E., Doty, J., Cooke, B., Wheaton, W., and Lewin, W. H. G. 1978, B. A. A. S., 10, 506.

Gullahorn, Gordon E., Isaacman, Richard, Rankin, J. M., and Payne, Robert P. 1977, A. J., 82, 309.

Hamming, R. W. 1973. Numerical Methods for Scientists and Engineers. 2nd edition. New York: McGraw Hill Book Co.

Hankins, T. H. and Rickett, B. J. 1975, Meth. in Comp. Phys., 14, 55.

Hegyi, D., Novick, R., and Thaddeus, P. 1971, IAU Symposium No. 46, 129. (Dordrecht; D. Reidel).

Helfand, D. J. 1978. private communication.

Helmken, H. 1975, Proc. of Fourteenth Intl. Conf. on Cosmic Rays, Munich, I, 128.

Iyengar, V. S., Manchanda, R. K., Durgaprasad, N., Gokhale, G. S., Kunte, P. K., and Sreekantan, B. V. 1974, Nature, 251, 292.

Jackson, J. D. 1975. Classical Electrodynamics. 2nd edition. New York: John Wiley and Sons, Inc.

Joss, P. C., Li, F. K., Wang, Y.-M., and Hearn, D. R. 1977, Ap. J., 214, 874.

Joss, P. C., Fechner, W. B., Forman, W., and Jones, C. 1978, Ap. J., 225, 994.

Kendziorra, E., Staubert, R., Pietsch, W., Reppin, C., Sacco, B., and Trumper, J. 1977, Ap. J. (Lett), 217, L93.

Kestenbaum, H. L., Ku, W., Novick, R., and Wolff, R. S. 1976, Ap. J. (Lett), 203, L57.

Kniffen, D. A., Fichtel, C. E., Hartman, R. C., Lamb, R. C., and Thompson, D. J. 1977, Proc. of 12th ESLAB Symposium, Frascati, 24-27 May 1977, 45.

Kristian, J. 1971, IAU Symposium No. 46, 87. (Dordrecht: D. Reidel).

Kurfess, J. D. 1971, Ap. J.(Lett), 168, L39.

Kurfess, J. D. 1978, Proc. on Symposium on Gamma-ray Spectroscopy in Astrophysics, Goddard Space Flight Center,MD,USA, 438.

Lamb, F. K., Pethick, C. J., and Pines, D. 1973, Ap. J., 184, 271.

Lamb, F. K., Pines, d., and Shaham, J. 1978, Ap. J., 224, 969.

Lampton, M., Margon, B., and Bowyer, S. 1976, Ap. J. 208, 177.

Landau, L. M. and Lifschitz, E. M. 1971. Classical Theory of Fields. 3rd edition. Reading: Addison-Wesley Publishing Co.

Laros, J. G., Matteson, J. L., and Pelling, R. M. 1973, Nature Phys. Sci., 246, 109.

Lloyd, K. H. 1969, Am. J. Phys., 37, 329.

Lodenquai, J., Canuto, V., Ruderman, M., and Tsuruta, S. 1974, Ap. J., 190, 141.

Lyne, A. G. and Thorne, D. J. 1975, Mon. Not. Roy. Astron. Soc., 172, 97.

Manchanda, R. K. 1977, Astrophys. and Space Sci., 50, 179.

Manchester, R. N. 1971, Ap. J. (Lett), 163, L61.

Manchester, Richard N. and Taylor, Joseph H. 1977. Pulsars. San Francisco: W. H. Freeman and Company.

Mandrou, P., Niel, M., Vedrenne, G., and Dupont, A. 1977, Ap. J., 212, 704.

Mather, Robert L. 1957, J. App. Phys., 28, 1200.

Matteson, J. L., Gruber, D. E., and Hoffman, J. A., 1978, Proc. of Symp. on Gamma-Ray Spectroscopy in Astrophysics, Goddard Space Flight Center, MD, USA, 386.

McClintock, J. E., Clark, G. W., Lewin, W. H. G., Schnopper, H. W., Canizares, C. R., and Sprott, G. F. 1974, Ap. J., 188, 159.

McCray, R. and Lamb, F. K. 1976, Ap. J. (Lett), 204, L115.

Melzer, D. W. and Thorne, K. S. 1966, Ap. J., 145, 514.

Mestel, L. 1971, Nature Phys. Sci., 233, 149.

Mushotzky, R. F. 1977, Ph.D. Thesis, UCSD.

Mushotzky, R. F., Boldt, E. A., Holt. S. S., Pravdo, S. H., Serlemitsos, P. J., Swank, J. H., and Rothschild, R. R. 1978, Ap. J. (Lett), 226, L65.

National Bureau of Standards Special Publication 432, 1976.

Ostriker, J. P. 1968, Nature, 217, 1127.

Pacholczyk, A. G. 1970. Radio Astronomy. San Francisco: W. H. Freeman and Co.

Pacini, F. and Salpeter, E. E. 1968, Nature, 218, 733.

Panofsky, Wolfgang K. H. and Phillips, Melba 1962. Classical Electricity and Magnetism. 2nd edition. Reading: Addison-Wesley Publishing Co.

Payne, Robert P. 1976, private communication.

Petterson, Jacobus A. 1975, Ap. J. (Lett), 201, L61.

Petterson, Jacobus A. 1978, Ap. J., 224, 625.

Pravdo, S. H., Becker, R. H., Saba, J. L., Serlemitsos, P. J., and Swank, J. H. 1978, IAU Circular 3116.

Pravdo, S. H., Becker, R. H., Boldt, E. A., Holt, S. S., Serlemitsos, P. J., and Swank, J. H. 1977, Ap. J. (Lett), 215, L61.

Pravdo, S. H. 1976, Ph.D. Dissertation, University of Maryland.

Pravdo, S. H., Boldt, E. A., Holt, S. S., and Serlemitsos, P. J. 1977, Ap. J. (Lett), 216, L23.

Pravdo, S. H. 1978, private communication.

Pravdo, S. H., Bussard, R. W., Becker, R. H., Boldt, E. A., Holt, S. S., Serlemitsos, P. J., and Swank, J. H. 1978, Ap. J., 225, 988.

Prendergast, K. and Burbidge, G. 1968, Ap. J. (Lett), 151, L83.

Pringle, J. E. 1977, Ann. N. Y. Acad. Sci., 302, 6.

Rankin, J. M., Payne, R. P., and Campbell, D. B. 1974, Ap. J. (Lett), 193, L71.

Rappaport, sS., Bradt, H., and Mayer, W. 1971, Nature Phys. Sci., 229, 40.

Ricker, G. R., Sheepmaker, A., Ryckman, S. G., Ballintine, J. E., Doty, J. P., Downey, P. M., and Lewin, W. H. G. 1975, Ap. J. (Lett), 197, L83.

Riegler, G. R. 1969, Ph.D. Thesis, University of Maryland.

Rose, William K. 1977. In Recognition of Compact Astrophysical Objects, ed. H. Ogelman and R. Rothschild. Washington DC: NASA.

Ruderman, M. A. and Sutherland, P. G. 1975, Ap. J., 196, 51.

Shapiro, S. L., Lightman, A. P., and Eardley, D. M. 1976, Ap. J., 204, 187.

Ryckman, S. G., Ricker, G. R., Sheepmaker, A., Ballintine, J. E., Doty, J. P., Downey, P. M., and Lewin, W. H. G. 1977, Nature, 266, 431.

Shulman, S., Friedman, H., Fritz, G., Henry, R. C., and Yentis, D. J. 1975, Ap. J. (Lett), 199, L101.

Smart, W. M. 1977. Textbook on Spherical Astronomy. 6th edition. Cambridge: Cambridge University Press.

Smith, F. G. 1977. Pulsars. Cambridge: Cambridge University Press.

Stein, J. A. and Lewin, W. H. G. 1967, J. Geophys. Res., 72, 383.

Strickman, Mark S., Johnson, W. Neil, and Kurfess, James D. 1979, to be published.

Sturrock, P. A. 1971, Ap. J., 164, 529.

Sturrock, P. A., Petrosian, V., and Turk, J. S. 1975, Ap. J., 196, 73.

Sutton, J. M., Staelin, D. H., and Price, R. M. 1971, IAU Symposium No. 46. Dordrecht: D. Reidel, 97.

Thomas, R. M., and Fenton, K. B. 1975, Proc. of Fourteenth Intl. Conf. on Cosmic Rays, 1, 188.

Toor, A. and Seward, F. D. 1974, A. J., 79, 995.

Toor, A. and Seward, F. D. 1977, Ap. J., 216, 560.

Trumper, J., Pietsch, W., Reppin, C., Sacco, B., Kendziorra, E., and Staubert, R. 1977, Ann. N. Y. Acad. Sci., 302, 538.

Trumper, J. Pietsch. W., Reppin, C., Voges, W., Staubert, R., and Kendziorra, E. 1978, Ap. J. (Lett), 219, L105.

Trumper, J. 1978, Proc. of Symp. on Gamma-Ray Spectroscopy in Astrophysics. Goddard Space Flight Center, MD, USA, 331.

Tsuruta, S., 1977, Ann. N. Y. Acad. Sci., 262, 391.

Tucker, Wallace H. 1975. Radiation Processes in Astrophysics. Cambridge: MIT Press.

Tucker, W., Kellogg, E., Gursky, H., Giacconi, R., and Tanenbaum, H. 1973, Ap. J., 180, 715.

U. S. Naval Observatory Time Service Report, Series 11, No. 225, 1978.

U. S. Naval Observatory Time Service Notice No.6, 1959.

Walraven, G. D., Hall, R. D., Meegan, C. A., Coleman, P. L., Shelton, D. H., and Haymes, R. C. 1975, Ap. J., 202, 502.

Warner, B., Nather, R. E., and McFarlane, M. 1969, Nature, 222, 233.

Wolff, R. S., Kestenbaum, H. L., Ku, W., and Novick, R. 1975, Ap. J. (Lett), 202, L77.

ACKNOWLEDGEMENTS

Carol Jo Crannell, Brian R. Dennis, and Carl Werntz are thanked for their guidance and encouragement throughout the course of the research.

The work presented in this thesis would not have been possible without the assistance of a great many people. Particular thanks are due to D. J. Thompson, for useful discussions on timing analysis; to S. H. Pravdo, for providing timing parameters for Her X-1; to the OSO-8 Project Scientist, Roger J. Thomas, for obtaining optimum observations of the Crab and Her X-1; to Robert Payne, D. J. Helfand, and Peter Backus for providing preliminary pulsar parameters for the Crab; and to Wendy Kennard and Edwin P. Cutler for their programming assistance.

The patience and understanding of family and friends has made the work go more easily. Special thanks go to my wife, Vicki, who has shared both the good times and the bad.

The support from NASA Grant NSG-5066 for the three years during which the work was in progress is gratefully acknowledged.